SLAC-PUB-1143
LBL-1371
(EXP)
November 1972

VECTOR MESON PRODUCTION BY POLARIZED PHOTONS AT 2.8, 4.7 AND 9.3 GeV*

J. Ballam, G. B. Chadwick, Y. Eisenberg,** E. Kogan,**
K. C. Moffeit, P. Seyboth,*** I. O. Skillicorn,†
H. Spitzer,†† and G. Wolf†††

Stanford Linear Accelerator Center
Stanford University, Stanford, California 94305

and

H. H. Bingham, W. B. Fretter, W. J. Podolsky,‡ M. S. Rabin,‡‡
A. H. Rosenfeld, and G. Smadja‡‡‡

University of California and Lawrence Berkeley Laboratory
Berkeley, California 94720

(Submitted to Phys. Rev.)

---

*Work supported by the U. S. Atomic Energy Commission and National Science Foundation.
**On leave from the Weizmann Institute, Rehovoth, Israel.
***Present address: Max-Planck-Institut für Physik und Astrophysik, München, Germany.
†Present address: University of Glasgow, Physics Department, Glasgow, Scotland.
††Present address: University of Hamburg, Hamburg, Germany.
†††Present address: DESY, Hamburg, Germany.
‡ Present address: University of Washington, Seattle, Washington.
‡‡Present address: University of Massachusetts, Amherst, Massachusetts.
‡‡‡Fellow of the Miller Institute of Basic Research in Science; Present address: DPHPE, CEN, Saclay, France.

ABSTRACT

We present results on vector meson photoproduction via $\gamma p \rightarrow Vp$ in the LBL-SLAC 82" hydrogen bubble chamber exposed to a linearly polarized photon beam at 2.8, 4.7 and 9.3 GeV. We find ρ^0 production to have the characteristics of a diffractive process, i.e., a cross section decreasing slowly with energy and a differential cross section with slope of ~ 6.5 GeV^{-2}. Within errors the ρ^0 production amplitudes are entirely due to natural parity exchange. S-channel helicity is conserved to a high degree in the $\gamma \rightarrow \rho^0$ transition. We find evidence for small helicity flip amplitudes for $\pi\pi$ pairs in the ρ^0 region. Photoproduction of ω mesons is separated into its natural (σ^N) and unnatural (σ^U) parity exchange contributions. The E_γ- and t-dependence and the spin density matrix of the unnatural parity exchange contribution are consistent with an OPE process. The natural parity exchange part has characteristics similar to ρ^0 production. At 9.3 GeV the ratio of $\sigma(\rho^0)$ to $\sigma^N(\omega)$ is ~ 7. The slope of the Φ differential cross section is ~ 4.5 GeV^{-2}, smaller than that of ρ^0 and ω production. Natural parity exchange is the main contributor to Φ production. No evidence for higher mass vector mesons is found in $\pi\pi$, $\pi\pi\pi$ or $K\bar{K}$ final states. The s- and t-dependence of Compton scattering as calculated from ρ, ω and Φ photoproduction using VDM agree with experiment, but the predicted Compton cross section is too small by a factor of two.

TABLE OF CONTENTS

I. INTRODUCTION

We have studied the photoproduction of hadrons by monochromatic linearly polarized photons at 2.8, 4.7, and 9.3 GeV, by exposing the LBL-SLAC 82" hydrogen bubble chamber to the SLAC backscattered laser beam. We obtained 92, 150 and 275 events/μb at the three energies. Here we present data on vector meson photoproduction in the reactions:

$$\gamma p \rightarrow p\rho^{o}$$

$$\gamma p \rightarrow p\omega$$

$$\gamma p \rightarrow p\Phi$$

For ρ^{o} photoproduction we give new data at 9.3 GeV which are compared to our previously published results at 2.8 and 4.7 GeV.[1] For ω and Φ photoproduction we present final results at all three energies. Preliminary data on ω production have been given in Refs. 2 and 3.

Previous bubble chamber[4,5,6] and counter experiments,[7,8,9] as well as this one, have shown that ρ^{o} photoproduction has the characteristics of a diffractive process — i.e., a sharply forward-peaked differential cross section varying slowly in magnitude with photon energy. Such behavior is accounted for, for example, in the vector dominance model[10] (VDM) by a direct $\gamma \rightarrow \rho^{o}$ coupling, followed by a diffractive scattering of the ρ^{o} from the target. Whatever mechanism is postulated, however, the use of polarized photons allows us to study the spin structure of the amplitudes involved by analyzing the ρ^{o} polarization.

In Ref. 1 we found that ρ^{o} photoproduction proceeds through natural parity exchange in the t-channel. Similar conclusions were reached in counter experiments with polarized beams.[11,12] We showed also that the dominant amplitudes

for the γ-ρ^o transition conserve the s-channel helicity of the photon. In our new data at 9.3 GeV we confirm these observations and also observe small helicity flip amplitudes in the ρ^o mass region.[13]

In the case of ω-photoproduction it has long been assumed from the energy dependence of the cross section that pion exchange was an important contributor.[5,6] The linear polarization of the beam allows us to establish that the term in the cross section with energy dependence $\sim E_\gamma^{-2}$ is indeed associated with unnatural parity exchange in the t-channel. At 9.3 GeV this contribution has become much smaller than the natural parity exchange part. The polarization of the beam allows us to study the spin structure of the natural-parity exchange contribution and to show that it is mainly s-channel helicity-conserving as in ρ^o photoproduction.

Photoproduction of Φ mesons is thought to proceed only by Pomeron exchange in the t-channel.[14] In agreement with previous experiments[5,8,9] we find a small cross section, increasing slowly with energy. The decay angular distributions of the Φ meson measured with the polarized photon beam are similar to those found for the ρ^o meson, indicating predominant natural parity exchange in the t-channel, and a roughly helicity conserving $\gamma \rightarrow \Phi$ transition.

The vector dominance model suggests that the photon acts as a superposition of the vector mesons ρ^o, ω, and Φ in hadronic reactions.[10] The s- and t-dependence of Compton scattering calculated from ρ, ω, and Φ photoproduction using VDM agrees with experiment, but the predicted cross section is too small by a factor of two. To save the simple prescriptions of VDM one may include contributions from higher mass vector states which couple to the photon. The Veneziano model[15] predicts such states as daughters of known meson resonances. If these higher mass vector mesons decayed into $\pi\pi$, $\pi\pi\pi$

or $K\bar{K}$, and if they retained the s-channel helicity of the photon, we would expect decay correlations similar to those observed for ρ^o, ω, and Φ. We find no evidence for higher vector mesons in the mass distributions or the appropriate moments of the decay angular distributions in the reactions $\gamma p \rightarrow (\pi^+\pi^-, \pi^+\pi^-\pi^o, K\bar{K})p$. Higher mass vector mesons could of course also decay into other final states. Mass enchancements have been reported in the missing mass spectrum recoiling against the proton,[8] in the 4π mass spectrum of the reaction[16] $\gamma p \rightarrow p\pi^+\pi^+\pi^-\pi^-$ and in the annihilation of e^+e^- into four charged pions.[17] The first two effects are also present in our experiment and are reported elsewhere.[3,18]

II. BEAM AND DATA ANALYSIS

The linearly polarized high energy photons in the bubble chamber were obtained by intersecting an intense linearly polarized laser beam with the electron beam at SLAC. Those photons scattered through 180^{o} by the Compton process obtain a substantial fraction of the incident electron energy while maintaining most of their original polarization. By collimating the backscattered photon beam to within $\sim 10^{-5}$ radians of the electron beam direction we obtain a nearly monochromatic polarized photon beam. For the 2.8 and 4.7 GeV exposures we used the output of a Q-switched ruby laser (E_{γ} = 1.78 eV) with electron energies of 12 and 16 GeV. To obtain 9.3 GeV photons the frequency of the ruby light was doubled in an ADP or KDP crystal, and an electron energy of 19 GeV was used. A summary of the beam and exposure parameters is given in Table I. The beam is described in more detail elsewhere.[3, 19, 20]

The film was scanned twice. Measurements were done on a Spiral Reader at LBL and on conventional measuring machines at LBL and SLAC. The measurements were analyzed with the standard TVGP-SQUAW system.[21] Ionization consistency with the fitted hypotheses was checked using the Spiral Reader pulse height information and doubtful cases were examined at the scanning table. For details of the analysis procedure, see Refs. 1, 3, 20, and 22.

III. ρ^0 PHOTOPRODUCTION IN THE REACTION $\gamma p \to p\pi^+\pi^-$ AT 9.3 GeV AND COMPARISON WITH DATA AT 2.8 AND 4.7 GeV

A. Event Selection and Channel Cross Section

The reaction

$$\gamma p \to p\pi^+\pi^- \qquad (1)$$

yields a 3 constraint kinematic fit. To select events of reaction (1) we require a kinematic $\chi^2 < 30$ and consistency with the observed track ionizations. From simulations of other 3-prong channels with the program PHONY[23] we find with the above selections a negligible contamination of reaction (1). A correction for scanning losses of 7 ± 5 percent is applied to the cross section in the interval $0.02 \leq |t| \leq 0.05$ GeV^2 (t is the 4-momentum transfer squared to the proton). The cross section for $|t| \leq 0.02$ GeV^2 was found by an extrapolation of the form e^{At} of the differential cross section from the region $0.02 \leq |t| \leq 0.4$ GeV^2. The channel cross section is 14.7 ± 0.6 μb.[20]

B. General Characteristics of the Reaction $\gamma p \to p\pi^+\pi^-$

In Fig. 1 we show the Dalitz plot for the channel $\gamma p \to p\pi^+\pi^-$ and the Chew Low plot for $\pi^+\pi^-$. Figures 2 and 3 give the $\pi^+\pi^-$, $p\pi^+$ and $p\pi^-$ mass projections. The channel is dominated by ρ^0 production at all $|t|$ intervals below 1 GeV^2. There is no evidence for higher mass mesons in the $\pi^+\pi^-$ mass distribution (Fig. 3). This can be more clearly seen in Fig. 4, where we plot the $\pi^+\pi^-$ mass distribution on a logarithmic scale and where we included also the lower energy data for comparison. In order to arrive at upper limits for the production of higher mass mesons we exclude Δ^{++} production and take all events in the $M_{\pi\pi}$ interval 1.2 - 1.4 (1.6 - 1.8) GeV, where such mesons are predicted by the Veneziano model.[15] The resulting upper limits (98% C.L.) are 0.27 (0.15) μb

respectively at 9.3 GeV. It is interesting to note that $d\sigma/dM_{\pi\pi}$ for $M_{\pi\pi} > 1$ GeV drops roughly like E_γ^{-2} (Fig. 4).

As can be seen from the $p\pi^+$ mass distribution (Fig. 3), there is some Δ^{++} production. The cross section is 0.32 ± 0.04 μb (see Ref. 1 for a description of the fit procedure). For completeness we give the Δ^{++} density matrix elements (see Ref. 1 for definitions) in Table II. The parity asymmetry, P_σ, is -0.91 ± 0.24 for $|t_{p/\Delta^{++}}| < 0.4$ GeV^2, showing that unnatural parity exchange, e.g., pion exchange, dominates the reaction $\gamma p \rightarrow \Delta^{++}\pi^-$ at 9.3 GeV.

We now discuss the general characteristics of the dipion system. As we observed at the lower energies,[1] the ρ^o shape changes as a function of t (see Fig. 2). As in our previous work we have parameterized the ρ^o shape by the form Breit-Wigner $\cdot$ $(M_\rho/M_{\pi\pi})^{n(t)}$. The fitted values of n, obtained from a maximum-likelihood fit on the Dalitz plot for separate t-slices (Appendix A of Ref. 1) are shown in Fig. 5. The exponent n(t) decreases with increasing $|t|$, and the ρ^o approaches a Breit-Wigner shape at larger momentum transfers. It is interesting to note that within errors the values of n(t) at 9.3 GeV are the same as at lower energies, i.e., the t-dependence of the ρ^o mass shape is independent of the photon energy. In the momentum transfer range 0.02 - 0.5 GeV^2 the t-distribution for dipion pairs (given in Table III) is well represented by the form $d^2\sigma/dtdM_{\pi\pi} = d^2\sigma/dtdM_{\pi\pi}\big|_{t=0}\, e^{At}$. In Fig. 6a,b and Table III we present the values of $d^2\sigma/dtdM_{\pi\pi}\big|_{t=0}$ and A for intervals of $M_{\pi\pi}$, obtained by a maximum likelihood fit. The rapid change of A with $M_{\pi\pi}$ is directly related to the change of shape of the $\pi\pi$ mass spectrum with momentum transfer. As was shown in Ref. 1 this effect can be explained by the Söding model,[24] in which a coherent background interferes with a diffractive ρ^o production amplitude having a t-slope independent of $M_{\pi\pi}$. (See curves in Figs. 2, 6b.)

We now turn to the decay angular distribution of the dipion system. We use the following angles[25]: Φ, the angle of the photon electric polarization vector with respect to the production plane in the overall center-of-mass system; θ and ϕ, the polar and azimuthal angles of the π^+ in the dipion rest frame. It is also convenient to introduce the angle $\psi = \phi - \Phi$, since s-channel helicity conserving p-wave dipion pairs have a decay angular distribution in the helicity frame given by $\sin^2\theta \cos^2\psi$ (for complete linear polarization of the incident photon).

In order to illustrate the dominant helicity-conserving characteristics of the dipion system in the ρ^0 region, we show in Fig. 7 the cos θ and ψ distributions in the helicity frame for the dipion mass region 0.6 - 0.88 GeV and for $0.02 \leq |t| \leq 0.4$ GeV^2. The curves on the figure are calculated assuming helicity conservation in the s-channel and using the calculated photon polarization of 0.77. The curves fit the data well.

A further general study of the dipion system was made using the moments $Y_\ell^m(\theta, \psi)$ with θ, ψ defined in the helicity frame. In contrast to our lower energy data[1] in which significant nonzero Y_1^0, Y_2^0, Re Y_2^2, Y_3^0, Y_4^0, and Y_6^0 moments were found, here we find that only the Y_2^0 and Re Y_2^2 moments are significantly different from zero within the present statistics. The Y_2^0, Re Y_2^2, and Y_4^0 moments are shown in Fig. 8 as a function of dipion mass. Note that the distributions of the Y_2^0 and Re Y_2^2 moments show the same skewing as the $\pi\pi$ mass distributions (Fig. 3), in accordance with our observations at the lower energies. We conclude from the moments that the only important angular momentum states in the dipion system are p-wave states and that these are confined to the ρ^0 mass region.

C. ρ^0 Cross Sections

1. Procedures

Experimental studies of ρ^0 photoproduction have revealed difficulties in defining and extracting ρ^0 cross sections in a unique way. We follow the procedures of Ref. 1 and give four cross sections for ρ^0 production:

(1) A ρ^0 cross section derived from a fit of the Söding model[24] to our data. In this cross section determination we are removing the influence of the coherent Drell background[26] and giving a ρ^0 cross section proportional to the area of a rho Breit-Wigner distribution, integrated over the available phase space. We use a Söding model with a Ferrari-Selleri form factor[27] and include a rescattering correction to the Drell terms.[28] The model is described in detail in Ref. 1.

(2) A ρ^0 cross section obtained from $d^2\sigma/dtdM'_{M=M_\rho} \cdot \frac{1}{2}\pi\Gamma_\rho$ with $M_\rho = 770$ MeV and $\Gamma_\rho = 145$ MeV as obtained from the Söding model fit above. This approach of Yennie[29] is based on the observation of Pumplin and Bauer[28] that the rescattering-corrected Drell diagram vanishes at the ρ^0 mass. It takes a constant-area Breit-Wigner distribution in contrast to method (1), in which the area under the ρ^0 Breit-Wigner shape depends on the available phase space. In this phenomenological application of the Söding model we determine $d^2\sigma/dtdM$ at $M = M_\rho$ from a fit of a smooth curve of the form Breit-Wigner $\cdot$ $(M_\rho/M_{\pi\pi})^{n(t)}$ to the $\pi\pi$ mass distribution. We refer to cross sections obtained using this technique as phenomenological Söding cross sections. (See Ref. 1 for a more detailed discussion.)

(3) A parameterization cross section obtained by fitting the Dalitz plot to a matrix element consisting of phase space, Δ^{++} and a ρ^0 whose shape is given by the form Breit-Wigner $\cdot$ $(M_\rho/M_{\pi\pi})^{n(t)}$. Basically this yields a ρ^0 cross

section through the assumption that all dipion pairs, other than those originating from Δ^{++} production and phase-space-like background, are from ρ^o production.

(4) A cross section for s-channel helicity-conserving dipion pairs (Π) calculated from

$$\Pi = \frac{\sigma_0}{P_\gamma} \sqrt{\frac{40\pi}{3}} \Sigma \, \mathrm{Re} \, Y_2^2(\theta, \psi)$$

where the sum extends over all events of reaction (1) in the appropriate t interval and σ_0 is the number of μb of cross section per event. Here we make use of our observation that the ρ^o production mechanism mainly conserves s-channel c.m.s. helicity at the $\gamma\rho$ vertex. Consequently the angular distribution of dipion pairs in the helicity frame has a component proportional to Re $Y_2^2(\theta, \psi)$.[1]

2. Results and Discussion

In Table IV we give total cross sections determined using these four methods. Differential cross sections are presented in Table V and Fig. 9. We also give in Table IV the extrapolated differential cross sections at $|t| = 0$ and the slopes A from a fit of the differential cross section to the form $B\, e^{At}$ in the interval $0.02 < |t| < 0.4$ GeV^2. For comparison we include the lower energy results[1] in Table IV.

The fits to our differential cross sections do not require a quadratic term in t. If quadratic contributions or a break at small $|t|$ (like that observed in pp scattering) are present, the forward cross sections obtained from a linear extrapolation may be unreliable (too small).

Table IV shows that the values of the cross sections and slopes obtained by the different methods are much closer to each other at 9.3 GeV than at the lower energies. The forward cross sections, for example, vary by $\leq 10\%$ at 9.3 GeV. We observe (see Table IV) that the ρ^o cross section is decreasing with energy,

but that the slopes of the phenomenological Söding, the parameterization and the Π differential cross sections are independent of energy within our errors. The Söding model fits give smaller slopes at the lower energies. However, this energy variation can be largely understood as being due to phase space limits which cut off the high mass ρ^o tail at small $|t|$ and low photon energies. When the slope is fitted directly in the matrix element we find the values 6.0 ± 0.3, 6.3 ± 0.3, 6.7 ± 0.2 GeV^{-2} at 2.8, 4.7, 9.3 GeV respectively. As expected, these values are in agreement with those of method (2).

The phenomenological Söding approach gives a cross section which depends on M_ρ and is proportional to Γ_ρ. This introduces a systematic uncertainty of ~20% which is not included in our errors. Effects of ρ-ω interference are largely averaged out, because $d\sigma/dtdM\big|_{M=M_\rho}$ was determined from a fit of a smooth curve over a wider mass region. The slope of $d\sigma/dt$ is, of course, independent of Γ_ρ and varies only slightly over the range of likely values of M_ρ.

The fitted Söding model cross sections depend on the form of the Drell background used. A different Drell background (one that was gauge invariant, for example) could lead to a different ρ^o cross section and a different fitted ρ^o mass and width. The only cross sections which are independent of the assumed ρ^o mass and width and/or the form of the Drell background are the parameterization and Π cross sections, but as we have emphasized,[1] these are not necessarily ρ^o cross sections.

Figure 9 gives a comparison of the differential ρ^o cross sections with other experiments. The data of Anderson et al.[8] at 11.5 GeV and Barish et al.[30] at 12 GeV were obtained in missing mass experiments and ρ^o cross sections were extracted by a method equivalent to our parameterization technique. The results show excellent agreement over the full range of t (Fig. 9a). The 7.5 GeV

bubble chamber data of Ref. 6 also agree with the present measurements. The Cornell experiment[9] at 8.5 GeV detects pion pairs near decay angles $\theta = \phi = 90^{\circ}$ (see Footnote 25 for definitions) in the helicity system and uses method (2) for extracting the ρ^{0} cross section. Thus the combination

$$2\left(\rho^{0}_{11} + \rho^{0}_{1-1}\right) \cdot \frac{d\sigma}{dt} = \left(\frac{d\sigma}{dt}\right)_{\text{Cornell}}$$

is measured, which, with our measured values for the density matrix elements (Table VI) is smaller than $d\sigma/dt$ at the larger $|t|$ values. This may explain the somewhat greater slope parameter found by Berger et al.[9]

D. Dipion Angular Distribution and ρ^{0} Spin Density Matrix

1. Spin Density Matrix Formalism

The decay angular distribution for vector mesons produced by linearly polarized photons can be expressed in terms of nine independent measurable spin density matrix parameters ρ^{α}_{ik} (31):

$$\begin{aligned} W(\cos\theta, \phi, \Phi) = \frac{3}{4\pi}\Big\{ & \frac{1}{2}\left(1 - \rho^{0}_{00}\right) + \frac{1}{2}\left(3\rho^{0}_{00} - 1\right)\cos^{2}\theta - \sqrt{2}\,\mathrm{Re}\,\rho^{0}_{10}\sin 2\theta\cos\phi \\ & - \rho^{0}_{1-1}\sin^{2}\theta\cos 2\phi - P_{\gamma}\cos 2\Phi\Big[\rho^{1}_{11}\sin^{2}\theta + \rho^{1}_{00}\cos^{2}\theta \\ & - \sqrt{2}\,\mathrm{Re}\,\rho^{1}_{10}\sin 2\theta\cos\phi - \rho^{1}_{1-1}\sin^{2}\theta\cos 2\phi\Big] \\ & - P_{\gamma}\sin 2\Phi\left[\sqrt{2}\,\mathrm{Im}\,\rho^{2}_{10}\sin 2\theta\sin\phi + \mathrm{Im}\,\rho^{2}_{1-1}\sin^{2}\theta\sin 2\phi\right]\Big\} \end{aligned} \tag{2}$$

Here P_{γ} is the degree of linear polarization of the photon. The contributions σ^{N}, σ^{U} to the cross section from natural parity ($P = (-1)^{J}$) and unnatural parity ($P = -(-1)^{J}$) exchange in the t-channel can be obtained from the density matrix

elements. Defining P_σ by

$$P_\sigma = \frac{\sigma^N - \sigma^U}{\sigma^N + \sigma^U}$$

one finds to leading order in energy[31,32]

$$P_\sigma = 2\rho^1_{1-1} - \rho^1_{00} \quad . \tag{3}$$

In the limit of high energies one can separate the density matrix ρ^α_{ik} into components ρ^N_{ik}, ρ^U_{ik} arising from natural and unnatural parity exchanges in the t-channel[31]:

$$\rho^{N,U}_{ik} = \frac{1}{2}\ \rho^0_{ik} \mp (-1)^i\ \rho^1_{-i,k} \tag{4a}$$

with the normalization

$$\mathrm{Tr}\ \rho^N + \mathrm{Tr}\ \rho^U = 1 \quad . \tag{4b}$$

The density matrix elements ρ^α_{ik} measure bilinear products of helicity amplitudes $T_{\lambda_V \lambda_{N'}, \lambda_\gamma \lambda_N}$ (see Appendix C of Ref. 1). Here $\lambda_V, \lambda_{N'}, \lambda_\gamma, \lambda_N$ denote the helicities of the vector meson, the outgoing proton, the photon and the target proton respectively. The elements ρ^0_{ik} are given by[31]:

$$\rho^0_{00} = \frac{1}{A}\ 2 \sum_{\lambda_{N'}\lambda_N} \left| T_{0\lambda_{N'}, 1\lambda_N} \right|^2 \tag{5a}$$

$$\mathrm{Re}\ \rho^0_{10} = \frac{1}{A}\ \mathrm{Re} \sum_{\lambda_{N'}\lambda_N} \left(T_{1\lambda_{N'}, 1\lambda_N} - T_{-1\lambda_{N'}, 1\lambda_N} \right) T^*_{0\lambda_{N'}, 1\lambda_N} \tag{5b}$$

$$\rho^0_{1-1} = \frac{1}{A}\ 2\ \mathrm{Re} \sum_{\lambda_{N'}\lambda_N} T_{1\lambda_{N'}, 1\lambda_N}\ T^*_{-1\lambda_{N'}, 1\lambda_N} \tag{5c}$$

$$A = \sum_{\lambda_V \lambda_{N'} \lambda_\gamma \lambda_N} \left| T_{\lambda_V \lambda_{N'}, \lambda_\gamma \lambda_N} \right|^2$$

The element ρ^0_{00} measures the intensity of helicity flip by one unit at the γV vertex and ρ^0_{1-1} measures the interference of nonflip and double-flip amplitudes. With a linearly polarized beam one can also measure the interference between nonflip and single-flip amplitudes by the combination

$$\text{Re}\,\rho^1_{10} - \text{Im}\,\rho^2_{10} = \frac{1}{A}\,2\,\text{Re}\left(\sum_{\lambda_{N'},\lambda_N} T_{1\lambda_{N'},1\lambda_N}\, T^*_{0\lambda_{N'},-1\lambda_N}\right) . \qquad (6)$$

We note that similar information is obtained from Re ρ^0_{10} (Eq. (5b)) provided that the double-flip amplitudes are small compared with the nonflip amplitudes. Finally we consider the combination

$$\rho^1_{1-1} + \text{Im}\,\rho^2_{1-1} = \frac{1}{A}\,2\sum_{\lambda_{N'},\lambda_N}\left(\left|T^N_{1\lambda_{N'},-1\lambda_N}\right|^2 - \left|T^U_{1\lambda_{N'},-1\lambda_N}\right|^2\right) \qquad (7)$$

where T^N and T^U are the amplitudes due to natural and unnatural parity exchange in the t-channel respectively.[31] The combination (7) can be used to estimate the intensity of helicity flip by two units at the γV vertex when either of the exchanges dominates.

The parameterization of the $\pi\pi$ angular distribution by Eqs. (2) - (7) is, of course, only valid for p-wave states, but as shown in the moment analysis of Section III.B these are the only important ones in the ρ^o mass region.

2. Dipion Density Matrix Averaged over the ρ^o Mass Region

Following our procedures at 2.8 and 4.7 GeV dipion density matrix elements averaged over the ρ^o region are first presented in a model independent way. In Section III.D.3 below we shall show that the dipion density matrix elements vary with $M_{\pi\pi}$ and that their interpretation in terms of ρ^o density matrix elements is model dependent.

The helicity frame density matrix elements in the ρ^0 region were determined as a function of t by a maximum likelihood fit including a ρ^0 contribution with a decay distribution given by Eq. (2) and Δ^{++} and phase space contributions (see Ref. 1 for details). This fitting method removes the effects of incoherent background under the ρ^0 which are small at 9.3 GeV but more important at lower photon energies. At 9.3 GeV the combined Δ^{++} and phase space backgrounds averaged over the ρ^0 mass region ($0.60 \leq M_{\pi\pi} \leq 0.88$ GeV) were 7% in the interval $0.4 \leq |t| \leq 0.8$ GeV^2 decreasing to < 2% at small $|t|$. Figure 10 and Table VI show the results of the fits. We observe that the production mechanism is mainly s-channel helicity conserving (SHC), i.e., $\rho^1_{1-1} = -\text{Im}\,\rho^2_{1-1} = 0.5$ with the other elements in Eq. (2) close to zero. There are, however, small but systematic deviations from zero in the elements $\text{Re}\,\rho^0_{10}$, ρ^0_{1-1}, $\text{Re}\,\rho^1_{10}$ and $\text{Im}\,\rho^2_{10}$. The values of P_σ are close to 1.0 for all t ($P_\sigma = 0.98 \pm 0.04$ for $0.02 \leq |t| \leq 0.80$ GeV^2) showing that the ρ^0 is produced predominantly by natural parity exchange.

To test for an instrumental source of the small deviations from zero in the above density matrix elements we evaluated the ρ^α_{ik} separately for events with photon polarizations parallel and normal to the optical axis of the bubble chamber cameras. Since the ρ^0 decays preferentially in the polarization plane, this effectively rotates the asymmetry of the angular distribution by 90^0 in the chamber. The two samples gave the same result. Thus the observed effects do not seem to originate from an experimental bias.

Next we give the separation of the density matrix into contributions from natural and unnatural parity exchanges in the t-channel, using Eq. (4). Figure 11 shows the density matrices $\rho^{N,U}$ at 2.8, 4.7 and 9.3 GeV in the helicity system. The elements ρ^U_{ik} are close to zero, again showing that natural parity exchange

dominates ρ^0 production at all energies. (We consider the nonzero value of ρ^U_{1-1} at 4.7 GeV to be a statistical fluctuation since it violates the condition $|\rho^U_{1-1}| \leq \rho^U_{11}$.) The deviations from SHC observed in Re ρ^0_{10} are seen to originate from natural parity exchange and do not show a marked energy dependence.

Finally, we use the ρ_{ik} and the combinations given in Eqs. (6) and (7) (see Fig. 12) to estimate the magnitude of the helicity-flip amplitudes for dipion pairs in the ρ^0 region. As discussed above, ρ^0_{00} measures the intensity of helicity flip by one unit at the $\gamma\pi\pi$ vertex. As seen from Fig. 10 and Fig. 16 of Ref. 1, the values of ρ^0_{00} are consistent with zero for $|t| < 0.4$ GeV^2. For $|t| > 0.4$ GeV^2 we find single-flip contributions to the cross section of $12 \pm 7\%$ and $28 \pm 6\%$ at 2.8 and 4.7 GeV respectively. At 9.3 GeV one obtains $3 \pm 5\%$ from ρ^0_{00}; a better estimate at this energy will be given from interference terms below. We note from Fig. 11 that at 4.7 GeV $\rho^0_{00} \approx \rho^N_{00}$ showing that the single-flip amplitudes are due to natural parity exchanges in the t-channel. No clear conclusion can be drawn at 2.8 GeV.

The combination $(\rho^1_{1-1} + \text{Im } \rho^2_{1-1})$ of Eq. (7) can be used to estimate the contribution of the double-flip amplitudes to the cross section at 2.8 and 4.7 GeV. As seen from Fig. 12 there is no evidence for such contributions for $|t| < 0.4$ GeV^2; for $|t| > 0.4$ GeV^2 we obtain $32 \pm 12\%$ and $16 \pm 10\%$ at the two energies respectively.

At 9.3 GeV the intensity terms ρ^0_{00} and Eq. (7) are zero within errors. However, the interference terms ρ^0_{1-1} (Fig. 10) and the combination (Re ρ^1_{10} - Im ρ^2_{10}) of Eq. (6) (plotted in Fig. 12) show that the double-flip and single-flip amplitudes are still 10 - 20% of the nonflip amplitudes at $|t| > 0.18$ GeV^2. Since at 9.3 GeV the flip amplitudes are small, the interference between nonflip and single-flip amplitudes can also be measured by Re ρ^0_{10}. We get the same

results as from the combination in Eq. (6). From Re $\rho^0_{10} \approx$ Re ρ^N_{10} (Figs. 10, 11) we infer that the single-flip amplitude is due to natural parity exchange in the t-channel.

We note that the SHC violating effects seem to be roughly of the same size at the $\gamma\pi\pi$ vertex in ρ^o photoproduction as in πN scattering.[13, 33, 34] Both reactions are thought to proceed mainly by Pomeron exchange.[34]

3. Mass Dependence of the Dipion Density Matrix and Interpretation in Terms of ρ^o Density-Matrix Elements

The density-matrix elements in the helicity system and P_σ for all dipion pairs were determined using Eq. (2), by the method of moments. Figure 13 shows the values at 9.3 GeV as a function of the dipion mass for $0.02 \leq |t| \leq 0.80$ GeV^2. As in the 2.8 and 4.7 GeV exposures, we observe marked changes of the $\pi\pi$ decay angular distribution with dipion mass. For a more detailed study of the $M_{\pi\pi}$ dependence of the dipion density matrix we concentrate on the elements ρ^0_{ik}, since these have the smallest statistical errors.

In Fig. 14 the elements ρ^0_{ik}, determined by the method of moments, are shown versus $M_{\pi\pi}$ for both small and large values of $|t|$. For $0.02 \leq |t| \leq 0.2$ GeV^2 the elements are close to zero up to 0.9 GeV. For $0.2 \leq |t| \leq 0.8$ GeV^2 ρ^0_{00} is again zero within errors in the ρ^o region. However, Re ρ^0_{10} and ρ^0_{1-1} vary through the ρ^o region and change sign around 0.7 GeV, indicating the importance of background effects. To demonstrate more clearly this variation near the ρ^o mass, we show in Fig. 15 the unnormalized moments $\rho^0_{ik} \cdot \frac{d\sigma}{dM_{\pi\pi}}$. Interference patterns are present, in particular in Re $\rho^0_{10} \cdot \frac{d\sigma}{dM_{\pi\pi}}$ and $\rho^0_{1-1} \cdot \frac{d\sigma}{dM_{\pi\pi}}$ for $0.2 \leq |t| \leq 0.8$ GeV^2.

The small incoherent Δ^{++} and phase-space-like background cannot be the cause of these strong variations. To explain the effects in Figs. 14 and 15, we

must introduce a coherent background. If this background had the same phase as the ρ^0 production amplitude and were slowly varying with $M_{\pi\pi}$, the interference pattern would be antisymmetric about the ρ^0 mass. The interference would therefore average to zero over the ρ^0 region and we would conclude that the ρ^0 amplitude had helicity flip components. If, however, we wish to enforce SHC for the ρ^0 amplitude, the background either would have to be $\sim 45^0$ out of phase with the ρ^0 or have a strong variation with $M_{\pi\pi}$. We now consider specific models for this background.

The curves in Figs. 14 and 15 were calculated from our formulation of the Söding model[24] (see Ref. 1 for details), in which an SHC ρ^0 amplitude interferes with a Drell background. The parameters of the model were adjusted to fit the mass and t-distributions. Although the dipion decay angular distribution is reproduced qualitatively, there are significant differences between the predictions of the model and the data in the ρ^0 region for the larger values of $|t|$. In the Söding model the change of sign in Re ρ^0_{10} and ρ^0_{1-1} results from an interference of the diffractive SHC ρ^0 amplitude with the helicity flip component of the mainly imaginary Drell background and thus occurs at $M_{\pi\pi} = M_\rho = 0.770$ GeV. The element ρ^0_{00} is predicted and observed to be small throughout the ρ^0 region. Averaged over the ρ^0 mass region ($0.6 \leq M_{\pi\pi} \leq 0.88$ GeV), and over the range $0.2 \leq |t| \leq 0.8$ GeV^2, we calculate Re $\rho^0_{10} = -0.021$ and $\rho^0_{1-1} = 0.00$ in the Söding model. Experimentally we find the values Re $\rho^0_{10} = 0.055 \pm 0.015$ and $\rho^0_{1-1} = -0.11 \pm 0.03$.

We remark that a dual model,[35] which approximates the Söding model in the ρ^0 region, also reproduces the mass and t distributions well. The model, which was constructed to be SHC at the ρ^0 mass, predicts values for the ρ^α_{ik} which are close to those of the Söding model.

Thus, within the formulation of the above models used by us the observed $\pi\pi$ angular distribution is not explained quantitatively if s-channel helicity conservation is assumed for ρ^0 production. Since the interference terms predicted by the models cancel out in the ρ^0 region, the ρ^{α}_{ik} of Fig. 10 represent the density-matrix elements of ρ^0 production. However, as we have emphasized, considerable uncertainties exist in the calculation of the Drell background. For example, the phase of the Drell term relative to the ρ^0 is not known, and the shape of the dipion mass spectrum could be changed by the terms that are required to make the Drell background gauge invariant.

In conclusion: (a) We have demonstrated that there are significant helicity flip amplitudes for dipion production in the ρ^0 region. (b) Because of theoretical uncertainties in the coherent background we are unable to determine the magnitude of s-channel helicity-flip amplitudes in ρ^0 photoproduction.

E. Comparison with Models

We compare the Söding model (for details of the calculation see Appendix B of Ref. 1) with our data on the reaction $\gamma p \to p\pi^+\pi^-$ at 2.8, 4.7, and 9.3 GeV. We find at all three energies that the model gives a good quantitative description of the $\pi^+\pi^-$ mass shape and its variation with t (Figs. 2, 3, 6b). With an s-channel helicity conserving ρ^0 amplitude, the main features of the $\pi^+\pi^-$ decay angular distribution (Figs. 8, 13, 14, 15) are also well reproduced, although as discussed in Section D, in the ρ^0 mass region some discrepancies exist at larger $|t|$. At the lower energies the model predicted the presence of moments other than Y_2^0 and Re Y_2^2 which were found in the data (see Fig. 14 of Ref. 1; in particular the Y_4^0 moment was small but significantly nonzero). At 9.3 GeV such moments are calculated to be too small to be observed in our experiment, and indeed we do not see any significant deviation from zero.

Photoproduction of ρ^0 is also described well by a dual resonant model.[35] We compared this model with our data and found that it predicts the observed cross section of $\pi^+\pi^-$ pair production to within 15%. Below $M_{\pi\pi} = 1$ GeV this dual model approximates the Söding model with the normalization of the ρ^0 amplitude fixed by duality. The $\pi\pi$ mass and production angular distributions are reproduced for $M_{\pi\pi} < 1$ GeV, but the model predicts more ρ' near 1.3 GeV than is consistent with the experimental $\pi^+\pi^-$ mass and decay angular distribution. S-channel helicity conservation was built into the model for the ρ^0 region. It describes qualitatively the $\pi\pi$ decay angular distribution for $M_{\pi\pi} < 1$ GeV, but, as for the Söding model, small discrepancies remain in the ρ^0 mass region at larger $|t|$.

In the model of Kramer[36] the ρ^0 is produced through final state interaction of the $\pi^+\pi^-$ system. Kramer has compared our data at 2.8 and 4.7 GeV with his model and found fair agreement. Our data do not support his prediction that the slope parameter A (see Fig. 6b) should sharply dip around $M_{\pi\pi} = 1.1$ GeV. Also, the associated structure in the decay angular distribution is not observed.

IV. ω PHOTOPRODUCTION IN THE CHANNEL $\gamma p \to p\pi^+\pi^-\pi^o$ AT 2.8, 4.7 AND 9.3 GeV

A. Event Selection

We have studied ω photoproduction in the reaction

$$\gamma p \to p\pi^+\pi^-\pi^o \quad . \tag{8}$$

The cross section for reaction (8) is 24.9 ± 1.5 μb, 15.1 ± 1.5 μb and 8.0 ± 0.6 μb at 2.8, 4.7,[1] and 9.3 GeV,[20] respectively. We now discuss the selection procedures used to obtain the sample of ω events in reaction (8). The presence of a neutral particle in the final state makes it difficult to obtain a clean sample of reaction (8), and we consequently had to investigate possible biases coming from the event selection. We determined the selection biases by generating with a Monte Carlo technique (program PHONY[23]) samples of measurements which were then treated in the same way as real events.

From our 3-prong events we selected a sample that had track ionizations consistent with the hypothesis

$$\gamma p \to p\pi^+\pi^- + \text{neutral(s)}$$

and which did not fit the 3-constraint reactions $\gamma p \to p\pi^+\pi^-$, $\gamma p \to pK^+K^-$, or $\gamma p \to pp\bar{p}$. We found that $\leq 7\%$ of ω events were lost by this selection. Figure 16a shows the mass squared MM^2 of the neutral system calculated assuming E_γ to be the mean beam energy of the particular exposure. At each energy we see a clear peak corresponding to the reaction (8). To remove events with more than one π^o we require $MM^2 < 0.1$ GeV^2 (loss $\leq 5\%$ of ω events). The momentum of the π^o and the incident photon energy for this restricted sample of events are then obtained from a 0-constraint calculation (using the beam energy in a 1C fit results in a higher background under the ω). For the 2.8 and 4.7 GeV exposures we

required in addition that the calculated photon energy be in the energy intervals of Table I. At 9.3 GeV no energy cut was used, because the greater error in the determination of E_γ at this energy was found to remove ω events without improving the ratio of ω events to background in the ω peak.

B. General Characteristics of the $\pi^+\pi^-\pi^o$ System

The 3π mass distributions for our final samples at the three energies are given in Fig. 16b, and scatter plots of the 3π mass versus t are shown in Fig. 17. A strong, peripheral ω signal is seen and no other prominent mass structure is found.

In view of the possibility that higher-mass vector-meson states may be produced in the reaction $\gamma p \to p\pi^+\pi^-\pi^o$ we have examined the higher 3π mass region for other structure. In Fig. 18a we plot the slope A obtained from an exponential fit to the t distribution in the interval $0.02 \leq |t| \leq 0.5$ GeV^2; in this $|t|$ interval the proton is identified by ionization. We have calculated the moments Y_2^0 and Re Y_2^2 in the helicity system[37]; these are shown as a function of the 3π mass in Fig. 18b, c. Except for clear signals in the ω mass regions, we see no evidence for other vector-meson states.

C. ω Cross Sections

As was seen in Fig. 16b, the ω shows a clear signal in the 3π mass above a small background. This background (typically < 10%) was estimated using hand-drawn curves. The ω peak has a full width at half maximum of about 25, 50, and 60 MeV at 2.8, 4.7 and 9.3 GeV, respectively. The shape and width of the peak is well reproduced by Monte Carlo simulations with the program PHONY,[23] where we use a Breit-Wigner distribution with Γ = 12 MeV as input. We used these simulations to calculate the corrections for ω events lost in the wings of the ω mass distribution, for the missing mass cut, and for the energy cut. The

combined correction factors are respectively 1.12, 1.22 and 1.29 at 2.8, 4.7 and 9.3 GeV. The correction at 9.3 GeV was found to be slightly t-dependent. Cross sections were further corrected for other decay modes (11%)[38] and scanning losses.[39]

Figure 19 and Table VII show the ω differential cross sections $d\sigma/dt$ and Fig. 20 and Table VIII show the total cross section, σ. Table VIII and Figs. 19 and 20 also show σ and $d\sigma/dt$ separated into contributions σ^N, σ^U from natural and unnatural parity exchanges in the t channel[31]:

$$\sigma^{N,U} = \frac{1}{2}(1 \pm P_\sigma) \cdot \sigma \quad .$$

In analogy to our analysis of ρ^o photoproduction, we fitted the differential ω cross sections $d\sigma/dt$ and $d\sigma^N/dt$ to an exponential form $d\sigma/dt = d\sigma/dt\big|_{t=0} \exp(At)$. The values found are given in Table VIII. We observe from Fig. 20 that σ^U decreases rapidly with increasing energy while σ^N is approximately constant. The slope parameter A^N has values consistent with those found for the ρ^o.

Finally, we compare our cross sections with those from previous experiments[5,6] and find good agreement (see Fig. 20).

D. ω Spin Density Matrix

For ω's produced by linearly polarized photons the angular distribution of the normal to the ω meson decay plane is given by Eq. (2).[37] As for the ρ^o, we introduce the angle $\psi = \phi - \Phi$. Figure 21 shows the distributions of cos θ and ψ in the helicity system for events in the ω mass region ($0.74 \leq M_{\pi^+\pi^-\pi^o} \leq 0.84$ GeV) and $0.02 \leq |t| \leq 0.3$ GeV^2. At the lower energies we observe little structure in ψ, but at 9.3 GeV the characteristic $\cos^2 \psi$ signal observed in ρ^o photoproduction develops.

Figure 22 and Table IX show the density matrix elements ρ^α_{ik} and P_σ calculated by the method of moments in the ω mass region for three t intervals. We

estimate the background to be ≤ 5 percent, and no background subtraction was made. As indicated by our simulation of ω production with PHONY, our cuts exclude some ω events when the π^o in the laboratory system is close to the beam direction and our mass resolution is poorer. Corrections of ≤ 1 s.d. were applied to ρ^0_{00}, ρ^0_{1-1}, ρ^1_{11}, and ρ^1_{1-1} at 9.3 GeV, but were unnecessary at the lower energies.

We now proceed with the separation of the natural and unnatural parity exchange components. We give in Fig. 23a,b the density matrices ρ^N_{ik}, ρ^U_{ik} of these two components (note that ρ^N_{ik}, ρ^U_{ik} are not normalized separately, but that Tr ρ^N + Tr ρ^U = 1). We have chosen to calculate ρ^N_{ik} in the helicity system since it gave the simplest form of the density matrix for the ρ^o. Figure 23a shows that ρ^N_{ik} is consistent within errors with $\rho^N_{00} = \rho^N_{1-1} = \text{Re}\ \rho^N_{10} = 0$, ρ^N_{11} dominant as expected for an s-channel helicity conserving $\gamma \to \omega$ transition. The density matrix for natural parity exchange is also consistent with having the same fraction of small helicity flip contributions that are observed in the ρ^o case.

In the unnatural parity exchange contribution we expect π exchange to be the dominant process. We therefore have evaluated ρ^U_{ik} in the Gottfried-Jackson system, where we expect ρ^U_{11} to be dominant and ρ^U_{00}, ρ^U_{1-1}, Re $\rho^U_{10} \approx 0$. At 9.3 GeV the unnatural parity exchange contribution is too small to allow conclusions. At 2.8 and 4.7 GeV we find ρ^U_{1-1}, Re ρ^U_{10} close to zero and ρ^U_{11} large. At 2.8 GeV ρ^U_{00} seems to be significantly nonzero. This deviation from the simplest expected OPE behavior could be caused by absorption effects or by a breakdown of the high energy approximation involved in separating natural and unnatural parity exchanges at 2.8 GeV.

E. Discussion of Results

From the data presented above we observe:

(1) The ω cross section becomes approximately constant above 5 GeV.

(2) While natural and unnatural parity exchange contributions are comparable between 3 and 5 GeV, natural parity exchange dominates at 9.3 GeV.

(3) The separation into σ^N and σ^U demonstrates that the rapid decrease of the total ω cross section at lower energies is due to the unnatural parity exchange contribution.

(4) The energy and t-dependence of the cross section σ^N, as well as the spin density matrix ρ^N_{ik}, agree within errors with those found for the ρ^o. In particular, the ρ^N_{ik} are compatible with s-channel helicity conservation at the γ-ω vertex.

(5) The energy variation ($\sim E_\gamma^{-2}$) of the cross section σ^U and the spin density matrix ρ^U_{ik} of the unnatural parity exchange contribution are consistent with the dominance of one-pion exchange.

F. A Model for ω Photoproduction

We have attempted to fit our data at all energies to a simple model. We describe ω photoproduction by a sum of diffractive and one pion exchange (OPE) parts. Specifically, we write for the cross section:

$$\frac{d\sigma}{dt} = \left.\frac{d\sigma^N}{dt}\right|_{t=0} e^{A^N t} + W \cdot \frac{d\sigma^{OPE}}{dt}(E_\gamma, t)$$

In the OPE calculation we used the formulation of Wolf[40] (using Benecke-Dürr form factors) and the value of $\Gamma_{\omega \to \pi\gamma} = 0.90$ MeV [38] for the radiative ω width.

Further, we allow for an energy dependence of $\left.\frac{d\sigma^N}{dt}\right|_{t=0}$ of the form:

$$\left.\frac{d\sigma^N}{dt}\right|_{t=0} = C\left(1+\frac{D}{E_\gamma}\right)$$

A χ^2 fit was performed to the differential cross sections and P_σ at the three energies in the interval $0.02 \leq |t| \leq 0.5$ GeV^2 and the results are (see curves in Fig. 20):

$$C = 9.3 \pm 1.7 \ \mu b/GeV^2$$

$$D = 1.4 \pm 1.2 \text{ GeV}$$

$$A^N = 6.7 \pm 0.6 \text{ GeV}^{-2}$$

$$W = 0.97 \pm 0.09$$

$$\chi^2 = 16 \text{ for } 19 \text{ degrees of freedom .}$$

We conclude that the absolute OPE calculation can account for the unnatural parity exchange contribution in the cross section and the spin density matrix (see C above). The energy dependence of the natural parity exchange cross section is consistent with that of ρ^0 production.

V. Φ PHOTOPRODUCTION AT 2.8, 4.7 AND 9.3 GeV

A. Event Selection

Photoproduction of Φ mesons occurs in the reactions:

$$\gamma p \rightarrow pK^+K^- \tag{9}$$

$$\gamma p \rightarrow pK_S^oK_L^o \tag{10}$$

Reaction (9) can be well separated from other 3-prong reactions by a 3-constraint kinematic fit and a check of the track ionization. Calculations with PHONY indicated that the contamination of (9) by other 3-prong reactions was less than 5% and was negligible for Φ production. Reaction (10) is a 1-prong + V^o topology in the bubble chamber. The photon energy and K_L^o momentum are obtained from a 0-constraint calculation, while the K_S^o is identified by a 3-constraint kinematic fit. Requiring the calculated photon energy to lie within the limits of Table I removes many of the events with additional neutral particles in the final state.

B. General Characteristics

Figure 24 gives the K^+K^- mass distributions found at 2.8, 4.7, and 9.3 GeV. We observe a clear peak at the Φ mass, with little background, and no evidence for higher vector mesons decaying into K^+K^-. The insert parts of Fig. 24 show the mass region around the Φ expanded in 2 MeV bins. Our calculated K^+K^- mass resolution in the Φ region at 9.3 GeV is ± 1.4 MeV. Fitting a p-wave Breit-Wigner shape,[41] with measuring resolution folded in, we find

$$M_\Phi = 1020.4 \pm 0.4 \text{ MeV}$$

$$\Gamma_\Phi = 3.8 \pm 0.9 \text{ MeV} \quad .$$

We have estimated the systematic error in M_Φ due to the calibration of the magnetic field by calculating the K^o mass from $K_S^o \rightarrow \pi^+\pi^-$ decays. We found

$M_{K^0} = 498.44 \pm 0.15$ MeV, indicating that the calibration of the magnetic field was 0.25% too high. The above value of M_Φ should therefore be reduced by 0.1 MeV.

Figure 25 shows the pK^+ and pK^- mass distributions. Apart from some possible Y*(1520) production at 2.8 GeV, no structure is observed. The wide enhancement at large masses is the reflection of the Φ (unshaded events in Fig. 25), which is produced mainly in the helicity states +1, -1.

Figure 26 shows the effective mass distribution of the $K^o_S K^o_L$ system of reaction (10). Again we observe a clear peak at the Φ mass. At 9.3 GeV the scanning efficiency for the 1-prong + V^o topology was found to be poorer than at the lower energies. We therefore do not use this topology at 9.3 GeV in the following.

C. Φ Cross Sections

We calculate cross sections from the number of events in the Φ mass interval $1.00 \leq M_{K\bar{K}} \leq 1.04$ GeV. A correction of $\sim 5\%$ was applied for visible K^+, K^- decays which were not classified as reaction (9) in our analysis. The correction factor for neutral K^o_S decays was $1/0.689$ [38] and the average geometrical correction factor was 1.02. In the t-interval $0.02 \leq |t| \leq 0.05$ GeV^2 a scanning correction of 15 ± 8 (7 ± 5 percent) was applied at 4.7 GeV (9.3 GeV). The cross section for $|t| < 0.02$ GeV^2 was found by a linear exponential extrapolation of the differential cross section. A 3% correction was applied for the tails of the Breit-Wigner distribution outside our Φ mass region. The cross sections were corrected for the unobserved decay modes of the Φ by a factor $\Gamma_{tot}/\Gamma_{\Phi \to K\bar{K}} = 1/0.798$ at 2.8 and 4.7 GeV and $\Gamma_{tot}/\Gamma_{\Phi \to K^+K^-} = 1/0.491$ at 9.3 GeV.[38] For 2.8, 4.7 GeV combined the observed branching ratio of $\Phi \to K^o_S K^o_L / \Phi \to K^+K^-$ was 0.7 ± 0.2, consistent with the world average.[38]

Figure 27 and Table X show the differential cross sections. In Table XI and Fig. 28 we present our total cross sections. The forward differential cross sections and slopes (shown in Fig. 28 and Table XI) were obtained from a maximum likelihood fit of the form $d\sigma/dt = d\sigma/dt\,|_{t=0}\, e^{At}$ to all events in the Φ mass region and in the interval $0.02 \leq |t| \leq 0.8$ GeV^2. There may be a slow increase in the cross section and in the slope with energy. As seen from Figs. 27, 28 our results are consistent with those from other experiments.[5,8,9,42,43] We give in Table XI also an estimate of the slope due to Pomeron exchange at each energy as calculated[34] from an analysis of ρ^o photoproduction data between 3 and 18 GeV. Agreement is found within errors consistent with the suggestion that Φ photoproduction proceeds by Pomeron exchange.[14]

D. Φ Spin Density Matrix

We analyze the decay of the Φ meson in the helicity system in the same way we analyzed the ρ^o. The decay angles are defined as in footnote 25, by replacing the direction of the π^+ by the direction of the K^+ or the K^o_S. The decay distribution is parameterized by Eq. (2). We also introduce the angle $\psi = \phi - \Phi$ as in the ρ^o analysis. Figure 29 shows the distribution of cos θ and ψ for events in the Φ mass region with $0.02 \leq |t| \leq 0.80$ GeV^2. Because of the low statistics we combine the 2.8 and 4.7 GeV data. We observe distributions similar to those found for the ρ^o. Table XII lists the density matrix elements ρ^{α}_{ik} and the parity asymmetry P_σ determined by the method of moments. We conclude from our data that the Φ meson seems to be produced predominantly by natural parity exchange in the t-channel. The ρ^{α}_{ik} are consistent with those found for ρ^o production.

We calculate the quantity

$$\Sigma = \frac{\sigma_{\parallel} - \sigma_{\perp}}{\sigma_{\parallel} + \sigma_{\perp}} = \frac{\rho^{1}_{11} + \rho^{1}_{1-1}}{\rho^{0}_{11} + \rho^{0}_{1-1}}$$

where $\sigma_{\parallel}$, $\sigma_{\perp}$ are the cross sections for symmetric K pairs produced parallel and normal to the photon polarization plane. Our values are consistent with the measurements of both the Cornell[44] and SLAC-Wisconsin groups[43] (see Table XII). We note, however, that Σ is equivalent to P_{σ} only if the helicity flip amplitudes are zero (Ref. 1, Appendix C).

VI. COMPARISON OF VECTOR MESON PHOTOPRODUCTION WITH THE VECTOR DOMINANCE MODEL

In Sections III-V we presented data on ρ^o, ω and ϕ photoproduction and showed that in each case there is a roughly energy independent part of the cross section associated with natural parity exchange in the t-channel. We will now compare vector meson photoproduction with predictions from VDM. Within VDM the vector meson (V) photoproduction amplitudes are related to the amplitudes for elastic scattering of transverse vector mesons on protons:

$$T(\gamma p \to Vp) = \frac{\sqrt{\alpha\pi}}{\gamma_V} T(V_t p \to Vp) \qquad (11)$$

We assume in accordance with the quark model the total ρp and ωp cross sections to be the same. Using Eq. (11) we then find at 9.3 GeV that the ratio $\gamma_\omega^2/\gamma_\rho^2 = \sigma(\gamma p \to p\rho)/\sigma^N(\gamma p \to p\omega)$ is between 6.5 and 7.5 depending on the analysis procedure used for the ρ^o (the statistical errors are $\sim 20\%$). These values are in agreement with the value 7.2 ± 1.2 measured in e^+e^- annihilation.[45] Simple SU_6 predicts 9 for this ratio, while modifications due to symmetry breaking have been calculated to give 7.5 [46] or 13.8.[47] Our result agrees best with the prediction of Ref. 46.

Using the determination of $\sigma(\rho^o p \to \rho^o p)$ obtained from ρ^o photoproduction in deuterium[48] or the quark model prediction, values in the range 0.5 - 0.7 are found for $\gamma_\rho^2/4\pi$. Such values are consistent with the e^+e^- storage ring results.[45]

One can obtain γ_Φ from the forward differential cross section for Φ photoproduction. Using the quark model value of 13 mb for the Φ nucleon total cross section[49] we find from Eq. (11) that $\gamma_\Phi^2/4\pi = 6.2 \pm 1.3$ at 9.3 GeV (allowing a 30% real part in the Φp forward amplitude reduces this number by $\sim 10\%$). As has been noted before, Φ photoproduction leads to values of γ_Φ^2

which are about twice as large as the one derived from the direct measurement in e^+e^- annihilations[50] but agrees with SU_6 predictions for the ratio $\gamma_\Phi^2/\gamma_\rho^2$.[46,47]

VDM further predicts that the Compton scattering amplitude is related to the sum of the transverse components of vector meson photoproduction amplitudes:

$$T(\gamma p \to \gamma p) = \sum_V \frac{\sqrt{\alpha\pi}}{\gamma_V} T(\gamma p \to V_t p) \tag{12}$$

In Eq. (12) the sum is over all vector mesons. Assuming that all amplitudes are imaginary and have the same spin structure, Eq. (12) becomes

$$\frac{d\sigma}{dt}(\gamma p \to \gamma p) = C \cdot \frac{\alpha}{4}\left\{\sum_{V=\rho,\,\omega,\,\phi}\left[\left(\frac{\gamma_V^2}{4\pi}\right)^{-1}\frac{d\sigma}{dt}(\gamma p \to V_t p)\right]^{1/2}\right\}^2 \tag{13}$$

where C is a scale parameter that should equal unity if all assumptions are correct.

Using our phenomenological Söding cross sections (Table V) for the ρ^0, together with our σ_ω and σ_Φ results, we have evaluated the R.H.S. of Eq. (13). (We have added σ_ω^U incoherently. Strictly speaking, one should use the transverse part of the vector meson cross sections, but this correction is negligible.) The values of $\gamma_V^2/4\pi$ were taken from the storage ring experiments.[45,50] The L.H.S. was obtained from recent Compton scattering experiments[51] and our total cross section measurements.[1,20] We adjust C for best agreement, and have plotted the resulting values in Fig. 30. As noted before,[6] one finds excellent agreement of the R.H.S. with both the s and t dependence of Compton scattering, but a scale factor $C \simeq 2$ is needed to obtain the Compton cross section. The value of the scale factor cannot be explained by the uncertainty in our ρ cross section. If we assume less than maximal interference between the vector meson amplitudes, the resulting value of C becomes even larger.

Agreement with the Compton scattering cross sections could be obtained with $C \simeq 1$, if the sum over vector mesons in Eq. (13) were extended to include more states. These states would have to give a contribution of $\sim 40\%$ to the amplitude sum of Eq. (13).

A search for $\rho' \rightarrow \pi^+\pi^-$ in several experiments,[6,52] including ours, yielded an upper limit of the order of 1 percent of the ρ^o cross section. As shown in Sections IV and V, no evidence for higher mass resonances is seen in $\pi^+\pi^-\pi^o$ and $K\bar{K}$ final states. However, an analysis of our multi-pion final states in the reactions $\gamma p \rightarrow p$ + pions indicates the presence of broad enhancements in the mass range 1.2 - 1.6 GeV in both the $(\pi^+\pi^+\pi^-\pi^-)$ [18] and $(\pi^+\pi^-$ + neutrals) mass distributions.[3] These enhancements, which are produced with small momentum transfers to the proton (t slope ~ 6 GeV^{-2}) have cross sections of $\sim 10\%$ of ρ^o production. The $\pi^+\pi^+\pi^-\pi^-$ enhancement has been identified as a $J^P = 1^-$, $I^G = 1^+$ state and is referred to as the ρ'.[18] Assuming that the ρ' nucleon cross section is equal to the ρ^o nucleon cross section and the ρ' decays only into $\pi^+\pi^+\pi^-\pi^-$, then from Eq. (12) $\gamma_{\rho'}^{-1} \sim 0.3\ \gamma_{\rho^o}^{-1}$. (A consistent value of $\gamma_{\rho'}$ can be derived from the e^+e^- experiments.[17]) Thus the ρ' contributes only $\sim 10\%$ to the amplitude sum in Eq. (13).

VII. CONCLUSIONS

From our study of vector meson production in the channels $\gamma p \rightarrow p\pi^+\pi^-$, $p\pi^+\pi^-\pi^o$, $pK\bar{K}$ we conclude

1. The shape and t-dependence of the dipion mass distribution in the ρ^o region is independent of photon energy.

2. At 9.3 GeV dipion pairs in the ρ^o region are in a p-wave state. No evidence exists for higher partial wave states in the ρ^o region. In contrast small but significant contributions from such states were observed at 2.8 and 4.7 GeV.

3. P-wave dipion production in the ρ^o region occurs through natural parity exchange in the t-channel.

4. Dipion production amplitudes in the ρ^o region are predominantly s-channel helicity conserving.

5. At 9.3 GeV the density-matrix elements Re ρ^0_{10} and ρ^0_{1-1}, studied as a function of the dipion mass, give evidence for interference between a predominantly SHC ρ^o amplitude and a coherent background.

6. When averaged over the ρ^o region the helicity-flip dipion amplitudes at $|t| > 0.18$ GeV^2 are about 15% of the helicity-nonflip amplitudes at 9.3 GeV. The flip amplitudes at the $\gamma\pi\pi$ vertex are of the same relative magnitude as those in πN scattering.

7. As at the lower energies the Söding model describes well the shape of the dipion mass spectrum and its variation with momentum transfer. It does not, however, give a quantitative description of the helicity flip amplitudes in the rho region.

8. Theoretical uncertainties in the Söding model preclude a calculation of the helicity flip background in the rho region. Consequently, the magnitude of the helicity flip amplitudes for the ρ^o cannot be determined.

9. Because of the theoretical uncertainties in defining the ρ^o cross sections we have derived ρ^o cross sections by four different methods. The results are shown in Tables IV and V. At 9.3 GeV there is closer agreement (within $\sim 10\%$) between the results of the different methods than at the lower energies.

10. Analysis of the reaction $\gamma p \rightarrow p\omega$ shows that unnatural parity exchange decreases from $\sim 55\%$ of the total ω cross section at 2.8 GeV to $\sim 5\%$ at 9.3 GeV. The unnatural parity contribution to ω production is well explained by OPE.

11. The natural parity exchange cross section in ω production does not vary strongly with energy; its E_γ and t dependence are consistent with those of the ρ^o. The natural parity exchange components of the ω density matrix are compatible with s-channel helicity conservation. At 9.3 GeV the ratio of the cross sections $\sigma_\rho/\sigma_\omega^N$ is between 6.5 and 7.5 in agreement with predictions from SU_6 and the quark model.

12. The cross section and slope of Φ meson photoproduction may increase slowly with energy. The slope of the differential cross section is smaller than that for ρ^o and ω production. Natural parity exchange in the t-channel seems to be the major process. The ratio σ_Φ/σ_ρ agrees with the prediction from SU_6 and the quark model.

13. In $p\pi^+\pi^-$, $p\pi^+\pi^-\pi^o$, $pK\bar{K}$ final states we find no evidence for higher mass vector mesons.

14. The s and t dependence of Compton scattering as calculated from ρ, ω and Φ photoproduction using VDM agree with experiment, but the predicted Compton cross section is too small by a factor of two.

ACKNOWLEDGEMENTS

We wish to thank the SLAC Operations Crew, R. Watt and the 82" Bubble Chamber Operations Group for their assistance in performing this experiment. We thank R. Gearhart, J. J. Murray and C. K. Sinclair for their help during the early stages of the experiment. We acknowledge the diligence of our scanners and data reduction group, in particular D. Blohm, K. Eymann, W. Hendricks and A. Wang. We thank Y. Avni for helpful discussions.

FOOTNOTES AND REFERENCES

1. H. H. Bingham et al., Phys. Rev. Letters 24, 955 (1970); J. Ballam et al., Phys. Rev. Letters 24, 960 (1970); 1467(E) (1970); Phys. Rev. D5, 545 (1972).
2. J. Ballam et al., Phys. Rev. Letters 24, 1364 (1970); 26, 155(E) (1971). J. Ballam et al., SLAC-PUB-980, Stanford Linear Accelerator Center (1971), unpublished.
3. W. J. Podolsky, UCRL-20128 (Ph.D. Thesis, unpublished), Lawrence Radiation Laboratory, Berkeley (1971).
4. Cambridge Bubble Chamber Group, Phys. Rev. 146, 994 (1966); 155, 1468 (1967).
5. Aachen-Berlin-Bonn-Hamburg-Heidelberg-München Collaboration, Phys. Rev. 175, 1669 (1968).
6. Y. Eisenberg et al., Phys. Rev. D5, 15 (1972).
7. H. Alvensleben et al., Phys. Rev. Letters 23, 1058 (1969).
8. R. Anderson et al., Phys. Rev. D1, 27 (1970).
9. C. Berger et al., Phys. Letters 39B, 659 (1972).
10. J. J. Sakurai, Ann. Phys. 11, 1 (1960); M. Gell-Mann and A. Zachariasen, Phys. Rev. 124, 953 (1961).
11. L. Criegee et al., Phys. Rev. Letters 25, 1306 (1970).
12. G. Diambrini-Palazzi et al., Phys. Rev. Letters 25, 478 (1970).
13. J. Ballam et al., SLAC-PUB-1092, Stanford Linear Accelerator Center (1972), to be published.
14. P.G.O. Freund, Nuovo Cimento 48A, 541 (1967).
15. J. A. Shapiro, Phys. Rev. 179, 1345 (1969).

16. M. Davier et al., SLAC-PUB-666, Stanford Linear Accelerator Center (1969) and contribution to the 1971 Symposium on Electron and Photon Interactions at High Energies, Cornell University, unpublished.

17. C. Bacci et al., Phys. Letters 38B, 551 (1972); G. Barbarino et al., Lettere al Nuovo Cimento 3, 683 (1972).

18. G. Smadja et al., Lawrence Berkeley Laboratory Report LBL-991 (1972) and Proceedings of the 3rd International Conference on Experimental Meson Spectroscopy, Philadelphia (1972); H. H. Bingham et al., SLAC-PUB-1113, Stanford Linear Accelerator Center (1972) and to be published.

19. C. K. Sinclair et al., IEEE Trans. on Nuclear Sciences 16, No. 3, 1065 (1969); J. J. Murray, P. R. Klein, SLAC-TN-67-19, Stanford Linear Accelerator Center (1967), unpublished.

20. J. Ballam et al., Total and partial γp cross sections at 9.3 GeV, Stanford Linear Accelerator Center, to be published.

21. F. T. Solmitz et al., Three view geometry program, Alvarez Group Programming Note, P-117 (1966); O. I. Dahl et al., SQUAW, Alvarez Group Programming Note, P-126 (1968), Lawrence Radiation Laboratory, Berkeley.

22. K. C. Moffeit, UCRL-19890 (Ph.D. Thesis, unpublished), Lawrence Radiation Laboratory, Berkeley.

23. E. Burns, D. Drijard, PHONY, Trilling-Goldhaber Group Technical Note 143, Lawrence Radiation Laboratory, Berkeley (1968), unpublished.

24. P. Söding, Phys. Letters 19, 702 (1965); see also A. S. Krass, Phys. Rev. 159, 1496 (1967).

25. We analyze the $\pi^+\pi^-$ system in the helicity frame, where the z axis is the direction of the $\pi^+\pi^-$ system in the overall (γp) c.m.s. The y axis is the

normal to the production plane, defined by the cross product $\hat{k} \times \hat{\rho}$ of the directions of the photon and the vector meson. The x axis is given by $\hat{x} = \hat{y} \times \hat{z}$. The angle Φ between the electric vector of the photon, $\hat{\epsilon}$, and the production plane in the total c.m. system is defined by $\sin \Phi = \hat{y} \cdot \hat{\epsilon}$ with the sign ambiguity resolved by $\cos \Phi = \hat{\epsilon} \cdot (\hat{y} \times \hat{k})$. The decay angles θ, ϕ are the polar and azimuthal angles of the direction of flight, $\hat{\pi}$, of the π^+ in the ρ rest system:

$$\cos \theta = \hat{\pi} \cdot \hat{z}$$

$$\cos \phi = \hat{y} \cdot (\hat{z} \times \hat{\pi}) / |\hat{z} \times \hat{\pi}|$$

$$\sin \phi = -\hat{x} \cdot (\hat{z} \times \hat{\pi}) / |\hat{z} \times \hat{\pi}|$$

In the Gottfried-Jackson (Adair) system the z axis is replaced by the direction of the photon in the vector meson rest system (overall c.m.s.).

26. S. D. Drell, Rev. Mod. Phys. 33, 458 (1961)

27. E. Ferrari, F. Selleri, Phys. Rev. Letters 7, 387 (1961).

28. J. Pumplin, Phys. Rev. D2, 1859 (1970); T. Bauer, Phys. Rev. Letters 25, 485 (1970).

29. D. R. Yennie, private communication.

30. B. Barish et al., California Institute of Technology preprint CALT-68-345 (1971).

31. K. Schilling, P. Seyboth, G. Wolf, Nucl. Phys. B15, 397 (1970); B18, 332(E) (1970).

32. G. Cohen-Tannoudji et al., Nuovo Cimento 55A, 412 (1968).

33. A. de Lesquen et al. Phys. Letters 40B, 277 (1972); G. Cozzika et al., Phys. Letters 40B, 281 (1972).

34. G. Chadwick, Y. Eisenberg and E. Kogan, in Proceedings of the 3rd International Conference on Experimental Meson Spectroscopy,

Philadelphia (1972), and SLAC-PUB-1093, Stanford Linear Accelerator Center (1972), to be published; see also Y. Avni, SLAC-PUB-1036, Stanford Linear Accelerator Center (1972).

35. P. Dewey, B. Humpert, Nucl. Phys. B33, 589 (1971).

36. G. Kramer, Zeitschrift für Physik 250, 413 (1972).

37. The decay angles are defined as in footnote 25 replacing the direction $\hat{\pi}$ of the π^+ by the normal $\vec{\pi}^+ \times \vec{\pi}^-$ to the ω decay plane in the ω rest system.

38. Particle Data Group, Phys. Letters 39B, 1 (1972).

39. No correction at 2.8 GeV, $5\ ^{+10}_{-5}$ percent at 4.7 GeV, 7 ± 5 percent at 9.3 GeV in $0.02 \leq |t| \leq 0.06$ GeV^2. The cross section below $|t| = 0.02$ GeV^2 was calculated from a linear exponential fit to the differential cross section at 4.7, 9.3 GeV in the region $0.02 \leq |t| \leq 0.4$ GeV^2.

40. G. Wolf, Phys. Rev. 182, 1538 (1969).

41. J. D. Jackson, Nuovo Cimento 34, 1644 (1964). We used the form $BW(M_{KK}) \propto Q \cdot M_{KK} \cdot \Gamma / \left((M_{KK}^2 - M_\Phi^2)^2 + (M_\Phi \cdot \Gamma)^2\right)$ with $\Gamma = \Gamma_\Phi \cdot \left(q(M_{KK})/q(M_\Phi)\right)^3 \cdot 2/\left(1 + \left(q(M_{KK})/q(M_\Phi)\right)^2\right)$, where Q is the c.m.s. momentum of the Φ and q the momentum of the K mesons in the Φ rest frame.

42. H. Alvensleben et al., Phys. Rev. Letters 28, 66 (1972).

43. H. J. Halpern et al., SLAC-PUB-1085, Stanford Linear Accelerator Center (1972); R. L. Anderson et al., SLAC-PUB-1086, Stanford Linear Accelerator Center (1972).

44. G. McClellan et al., Phys. Rev. Letters 26, 1593 (1971).

45. D. Benaksas et al., Phys. Letters 39B, 289 (1972); J. LeFrancois, Proceedings of the 1971 Symposium on Electron and Photon Interactions at High Energies, Cornell (1971).

46. T. Das, V. S. Mathur, S. Okubo, Phys. Rev. Letters 19, 470 (1967).

47. R. J. Oakes, J. J. Sakurai, Phys. Rev. Letters 19, 1266 (1967).

48. R. L. Anderson et al., Phys. Rev. D4, 3245 (1971).

49. M. Krammer, Acta Phys. Austr. 32, 395 (1970).

50. J. C. Bizot et al., Phys. Letters 32B, 416 (1970); V. E. Balakin et al., Phys. Letters 34B, 328 (1971).

51. R. L. Anderson et al., Phys. Rev. Letters 25, 1218 (1970);
A. M. Boyarski et al., Phys. Rev. Letters 26, 1600 (1971);
G. Buschhorn et al., Phys. Letters 37B, 207 (1971).

52. H. Alvensleben et al., Phys. Rev. Letters 26, 273 (1971);
F. Bulos et al., Phys. Rev. Letters 26, 149 (1971);
G. McClellan et al., Phys. Rev. Letters 23, 718 (1969).

TABLE I

Beam Parameters and Exposure Statistics

Average Beam Energy E_γ (GeV)	Full Width at Half Maximum (GeV)	Number of Pictures	Average Linear Polarization P_γ (%)	Events Per μb	E_γ Limits Accepted (GeV)
2.8	0.15	294,000	93±2	92±4	2.4-3.3
4.7	0.45 [a]	454,000	91±2	150±6	4.1-5.3
9.3	0.60	1,260,000	77±2	275±6	8.0-10.3

[a]Broadened by energy shifts. For a constant electron energy the FWHM was about 0.35 GeV.

TABLE II

Reaction $\gamma p \rightarrow \Delta^{++}\pi^-$ at 9.3 GeV. Density matrix of Δ^{++} in the Gottfried-Jackson system for $|t_{p/\Delta^{++}}| \leq 0.4$ GeV^2

ρ^0_{33}	0.21±0.07
Re ρ^0_{31}	-0.02±0.09
Re ρ^0_{3-1}	-0.16±0.07
ρ^1_{11}	-0.34±0.15
ρ^1_{33}	-0.11±0.15
Re ρ^1_{31}	0.28±0.16
Re ρ^1_{3-1}	0.21±0.15
Im ρ^2_{31}	-0.21±0.11
Im ρ^2_{3-1}	-0.04±0.12
P_σ	-0.91±0.24

TABLE III

Reaction $\gamma p \rightarrow p\pi^+\pi^-$ at 9.3 GeV. $\Delta\sigma/\Delta t \Delta M_{\pi\pi}$ in $\mu b/GeV^3$. Here Δt is the interval heading the column (no $|t|_{min}$ correction has been made) and $\Delta M_{\pi\pi}$ is the interval in $\pi\pi$ mass given in the first column. Also given are B and A from a fit of the form $B \cdot e^{At}$ in the interval $t_0 \leq |t| \leq 0.5$ GeV^2, where t_0 is the larger of $|t|_{min}$ and 0.02 GeV^2. $\Delta\sigma/\Delta M_{\pi\pi}$ is the cross section integrated from $|t| = 0.02$ to $|t|_{max}$.

$M_{\pi\pi}$(GeV) \ $\frac{\Delta\sigma}{\Delta t \Delta M_{\pi\pi}}$ ($\mu b/GeV^3$) for $|t|$ (GeV^2)	0.02-0.05	0.05-0.075	0.075-0.10	0.10-0.15	0.15-0.20	0.20-0.25	0.25-0.30	0.30-0.35	0.35-0.40	0.40-0.50	$\frac{\Delta\sigma}{\Delta M_{\pi\pi}}$ ($\mu b/GeV$) 0.02-$\|t\|_{max}$	from fit $B \cdot e^{At}$ B ($\mu b/GeV^3$)	A (GeV^{-2})
0.28-0.32	6± 4	0± 0	0± 0	4± 3	0± 0	0± 0	0± 0	0± 0	2± 2	0± 0	0.5±0.2	4± 3	8.0±4.3
0.32-0.36	16± 7	15± 7	0± 0	5± 3	0± 0	4± 3	0± 0	2± 2	0± 0	0± 0	1.5±0.4	24±11	13.3±3.5
0.36-0.40	36± 10	18± 8	22± 9	7± 4	4± 3	2± 2	2± 2	5± 3	0± 0	1± 1	3.2±0.5	39±11	10.1±1.9
0.40-0.44	55± 13	25± 10	11± 6	7± 4	7± 4	0± 0	2± 2	0± 0	0± 0	0± 0	3.6±0.6	93±28	18.8±3.1
0.44-0.48	81± 16	44± 13	25± 10	13± 5	9± 4	4± 3	2± 2	2± 2	2± 2	2± 1	6.0±0.7	95±20	12.5±1.6
0.48-0.52	71± 15	73± 16	44± 13	15± 5	15± 5	9± 4	9± 4	4± 3	2± 2	0± 0	7.8±0.8	111±20	11.5±1.3
0.52-0.56	84± 16	62± 15	33± 11	40± 9	22± 6	7± 4	9± 4	4± 3	4± 3	0± 0	9.2±0.9	120±20	10.5±1.1
0.56-0.60	140± 21	76± 17	87± 18	44± 9	29± 7	20± 6	13± 5	2± 2	11± 4	1± 1	14.3±1.1	180±24	10.2±0.9
0.60-0.64	156± 22	109± 20	113± 20	58± 10	51± 10	24± 7	15± 5	9± 4	5± 3	3± 2	19.2±1.3	219±26	9.6±0.8
0.64-0.68	204± 25	193± 26	197± 27	51± 10	78± 12	45± 9	29± 7	13± 5	5± 3	6± 2	27.9±1.6	304±29	9.1±0.6
0.68-0.72	260± 28	204± 27	146± 23	113± 14	93± 13	56± 10	66± 11	35± 8	16± 5	10± 3	37.6±1.9	310±26	7.1±0.5
0.72-0.76	354± 33	269± 31	233± 29	189± 19	124± 15	104± 14	62± 11	42± 9	20± 6	15± 4	53.7±2.2	461±33	7.5±0.4
0.76-0.80	286± 29	240± 30	204± 27	129± 15	122± 15	87± 13	60± 10	35± 8	38± 8	15± 4	47.2±2.1	352±27	6.6±0.4
0.80-0.84	114± 19	127± 22	51± 14	91± 13	69± 11	55± 10	36± 8	22± 6	24± 7	15± 4	25.9±1.5	149±16	5.1±0.5
0.84-0.88	45± 12	58± 15	40± 12	44± 9	40± 9	27± 7	15± 5	7± 4	7± 4	6± 2	12.5±1.1	76±12	5.5±0.8
0.88-0.92	36± 10	7± 5	22± 9	20± 6	22± 6	11± 4	7± 4	4± 3	5± 3	4± 2	6.2±0.7	35± 8	5.1±1.1
0.92-0.96	10± 5	22± 9	4± 4	13± 5	7± 4	5± 3	9± 4	4± 3	4± 3	1± 1	3.5±0.6	18± 5	4.8±1.4
0.96-1.00	13± 6	11± 6	4± 4	2± 2	9± 4	9± 4	4± 3	2± 2	4± 3	3± 2	3.0±0.5	11± 4	3.1±1.5
1.00-1.10	3.9±2.2	7.3±3.3	7.3±3.3	5.1±1.9	2.9±1.5	3.6±1.6	2.2±1.3	2.2±1.3	4.4±1.8	0.4±0.4	1.8±0.3	8± 2	3.8±1.2
1.10-1.20	5.2±2.5	10.2±3.9	1.5±1.5	4.4±1.8	2.9±1.5	2.2±1.3	0.7±0.7	2.2±1.3	0.7±0.7	1.1±0.6	1.5±0.2	7± 2	5.1±1.4
1.20-1.40	4.5±1.7	2.9±1.5	3.6±1.6	2.5±1.0	2.2±0.9	3.3±1.1	1.8±0.8	1.1±0.6	1.1±0.6	0.9±0.4	1.2±0.1	5± 1	3.6±1.1
1.40-1.60	3.9±1.5	4.4±1.8	0.7±0.7	2.2±0.9	1.5±0.7	0.7±0.5	1.5±0.7	1.5±0.7	1.5±0.7	1.1±0.4	1.2±0.1	3± 1	2.7±1.1
1.60-1.80	1.9±1.1	3.6±1.6	2.9±1.5	1.5±0.7	1.8±0.8	2.5±1.0	0.7±0.5	1.5±0.7	0.4±0.4	0.9±0.4	0.9±0.1	3± 1	3.2±1.2
1.80-2.00	0.0±0.0	0.0±0.0	1.5±1.0	2.2±0.9	1.5±0.7	0.7±0.5	0.0±0.0	0.4±0.4	0.7±0.5	0.7±0.5	0.6±0.1	2± 1	4.6±2.0
2.00-2.20	0.0±0.0	0.0±0.0	0.7±0.7	1.8±0.8	1.5±0.7	0.7±0.5	0.7±0.5	1.5±0.7	0.0±0.0	0.4±0.1	0.4±0.1	-	-
2.20-2.40	0.0±0.0	0.0±0.0	0.0±0.0	1.1±0.6	0.4±0.4	0.7±0.5	0.7±0.5	0.0±0.0	0.7±0.5	0.2±0.2	0.3±0.1	-	-
2.40-2.60	0.0±0.0	0.0±0.0	0.0±0.0	0.0±0.0	0.0±0.0	0.0±0.0	0.0±0.0	0.7±0.5	0.7±0.5	0.2±0.2	0.3±0.1	-	-
2.60-2.80	0.0±0.0	0.0±0.0	0.0±0.0	0.0±0.0	0.0±0.0	0.4±0.4	0.4±0.4	0.4±0.4	0.0±0.0	0.4±0.3	0.4±0.1	-	-

TABLE IV

Reaction $\gamma p \rightarrow p\pi^+\pi^-$ at 2.8, 4.7 and 9.3 GeV: Dipion total cross sections, differential cross sections at t=0 and slope A of the differential cross sections (assuming the form $d\sigma/dt|_{t=0}\ e^{At}$) fitted in the interval $0.02 \leq |t| \leq 0.40$ GeV^2.

E_γ	2.8 GeV	4.7 GeV	9.3 GeV
Söding Model [a]			
$\sigma(\mu b)$	18.6±1.0	15.9±0.7	13.5±0.5
$\left.\frac{d\sigma}{dt}\right\|_{t=0}\left(\frac{\mu b}{GeV^2}\right)$	104±6	94±6	86±5
A (GeV^{-2})	5.4±0.3	5.9±0.3	6.5±0.2
Phenomenological Söding [a]			
$\sigma(\mu b)$ [b]	23.5±2.4	18.2±1.6	14.0±0.9
$\left.\frac{d\sigma}{dt}\right\|_{t=0}\left(\frac{\mu b}{GeV^2}\right)$	148±12	109±8	88±4
A (GeV^{-2})	6.3±0.4	6.0±0.3	6.3±0.3
Parameterization			
$\sigma(\mu b)$	21.0±1.0	16.2±0.7	13.3±0.5
$\left.\frac{d\sigma}{dt}\right\|_{t=0}\left(\frac{\mu b}{GeV^2}\right)$	138±8	114±6	95±4
A(GeV^{-2})	6.6±0.3	7.2±0.3	7.3±0.2
II			
$\sigma(\mu b)$	18.6±1.1	14.5±1.0	11.8±0.5
$\left.\frac{d\sigma}{dt}\right\|_{t=0}\left(\frac{\mu b}{GeV^2}\right)$	144±12	109±8	84±6
A (GeV^{-2})	7.5±0.6	7.6±0.5	7.1±0.4

[a] Errors do not include uncertainties in the model (see text).

[b] Calculated from: $\sigma = (d\sigma/dt)_{t=0}/A$.

TABLE V

Reaction $\gamma p \rightarrow p\pi^+\pi^-$ at 9.3 GeV. Dipion differential cross sections.

$\lvert t\rvert$ (GeV^2)	Söding[a] Model Fit	Phenomenological[a] Söding Cross Section	Parameterization	S-Channel Helicity Conserving Dipion Pairs (II)
	$\frac{d\sigma}{dt}$ (μb/GeV^2)			
0.02 -0.05	67.5 ±4.5	71.8±4.3	78.2 ±4.5	77.0 ±6.5
0.05 -0.075	60.2 ±3.3	60.8±4.4	62.2 ±3.0	40.0 ±5.6
0.075-0.10	46.7 ±2.8	45.7±3.9	49.9 ±2.7	54.3 ±4.4
0.10--0.15	35.4 ±1.8	38.4±2.4	34.2 ±1.6	33.9 ±2.8
0.15 -0.20	30.4 ±1.6	30.2±2.2	28.5 ±1.5	27.2 ±2.6
0.20 -0.25	21.0 ±1.4	20.2±1.2	19.2 ±1.2	19.1 ±2.2
0.25 -0.30	15.2 ±1.2		14.1 ±1.0	11.6 ±1.6
0.30 -0.40	8.0 ±0.6	8.8±0.8	7.2 ±0.5	5.2 ±1.0
0.40 -0.50	3.9 ±0.4	4.3±0.6	3.5 ±0.4	2.7 ±0.6
0.50 -0.70	1.5 ±0.2	1.4±0.2	1.5 ±0.2	1.7 ±0.3
0.70 -1.0	0.43±0.09		0.40±0.08	0.56±0.10
1.0 -1.5			0.06±0.02	0.06±0.08

[a]Errors do not include uncertainties in the model (see text).

TABLE VI

Reaction $\gamma p \rightarrow p\pi^+\pi^-$ at 9.3 GeV. Density matrix elements in the helicity system and parity asymmetry for dipion pairs in the ρ^0 region as determined from a maximum likelihood fit in intervals of the momentum transfer t.

$\lvert t \rvert$ (GeV^2)	0.02-0.05	0.05-0.08	0.08-0.12	0.12-0.18	0.18-0.25	0.25-0.40	0.40-0.80
ρ^0_{00}	0.02±0.01	-0.06±0.02	-0.01±0.02	0.03±0.02	-0.02±0.02	0.00±0.03	0.03±0.05
ρ^1_{1-1}	-0.02±0.03	0.06±0.03	-0.06±0.03	0.01±0.03	-0.08±0.03	-0.10±0.03	-0.16±0.04
Re ρ^0_{10}	0.00±0.02	0.04±0.02	0.04±0.02	0.03±0.02	0.07±0.02	0.06±0.02	0.10±0.03
ρ^1_{00}	0.03±0.02	-0.05±0.03	0.03±0.05	-0.05±0.04	0.01±0.04	-0.05±0.05	-0.04±0.08
ρ^1_{11}	-0.06±0.04	0.06±0.04	-0.05±0.05	-0.02±0.04	0.02±0.05	0.05±0.05	-0.06±0.06
ρ^1_{1-1}	0.48±0.04	0.38±0.05	0.48±0.05	0.48±0.05	0.49±0.05	0.41±0.06	0.57±0.07
Re ρ^1_{10}	0.03±0.03	0.03±0.03	-0.05±0.03	-0.01±0.03	-0.13±0.03	-0.02±0.03	-0.15±0.04
Im ρ^2_{1-1}	-0.50±0.04	-0.42±0.05	-0.57±0.04	-0.48±0.04	-0.49±0.05	-0.42±0.06	-0.64±0.10
Im ρ^2_{10}	-0.05±0.03	0.02±0.03	0.03±0.02	0.03±0.03	0.08±0.03	0.03±0.03	0.06±0.05
P_σ	0.93±0.09	0.80±0.11	0.93±0.11	1.00±0.10	0.97±0.12	0.86±0.12	1.17±0.15

TABLE VII

Reaction $\gamma p \rightarrow p\omega$ at 2.8, 4.7 and 9.3 GeV. Differential cross sections.

$\lvert t \rvert$ (GeV^2)	$\frac{d\sigma}{dt}$ (μb/GeV^2)		
	E_γ = 2.8 GeV	E_γ = 4.7 GeV	E_γ = 9.3 GeV
0.014-0.06	25.9 ±3.1	19.6 ±3.1	-
0.02 -0.06	-	-	10.2 ±1.4
0.06 -0.10	21.4 ±3.0	10.8 ±1.8	6.9 ±1.0
0.10 -0.15	14.7 ±2.3	8.1 ±1.4	6.5 ±1.0
0.15 -0.20	7.6 ±1.6	5.6 ±1.1	3.7 ±0.8
0.20 -0.30	6.4 ±1.1	2.8 ±0.6	2.2 ±0.5
0.30 -0.40	4.2 ±0.8	1.9 ±0.5	0.8 ±0.2
0.40 -0.50	1.2 ±0.6	0.8 ±0.4	
0.50 -1.0	0.8 ±0.2	0.3 ±0.1	0.15±0.07
1.0 -2.0	0.24±0.12	0.0 ±0.03	
2.0 $-\lvert t \rvert_{max}$	0.18±0.10	-	
2.0 -5.5	-	0.0 ±0.01	
5.5 $-\lvert t \rvert_{max}$	-	0.04±0.04	

TABLE VIII

Reaction $\gamma p \rightarrow p\omega$ at 2.8, 4.7 and 9.3 GeV. Total cross sections and forward differential cross sections $\left.\frac{d\sigma}{dt}\right|_{t=0}$ and slopes A from a fit of the form $\frac{d\sigma}{dt} = \left.\frac{d\sigma}{dt}\right|_{t=0} e^{At}$.

	E_γ = 2.8 GeV	E_γ = 4.7 GeV	E_γ = 9.3 GeV
$\sigma(\mu b)$	5.3±0.5	3.0±0.3	1.9±0.3
$\left.\frac{d\sigma}{dt}\right\|_{t=0} (\mu b/GeV^2)$	33.2±3.6 [a]	22.0±3.2 [a]	13.7±1.6 [a]
A (GeV^{-2})	6.8±0.6 [a]	7.9±0.9 [a]	7.5±0.8 [a]
$\sigma^N(\mu b)$	2.4±0.4	1.7±0.3	1.8±0.3
$\left.\frac{d\sigma^N}{dt}\right\|_{t=0} (\mu b/GeV^2)$	14.5±5.1 [b]	14.6±4.8 [b]	11.4±2.1 [a]
A^N (GeV^{-2})	7.3±2.4 [b]	8.5±2.4 [b]	6.6±1.1 [a]
$\sigma^U(\mu b)$	2.9±0.4	1.3±0.3	0.1±0.2

[a] fit interval $0.02 \leq |t| \leq 0.5$ GeV^2

[b] fit interval $0.014 \leq |t| \leq 0.4$ GeV^2

TABLE IX

Reaction $\gamma p \rightarrow p\omega$ at 2.8, 4.7 and 9.3 GeV. Density matrix of ω in the helicity system.

	E_γ = 2.8 GeV			E_γ = 4.7 GeV			E_γ = 9.3 GeV		
$\|t\|$ (GeV^2)	0.02-0.06	0.06-0.15	0.15-0.60	0.02-0.06	0.06-0.15	0.15-0.60	0.02-0.06	0.06-0.15	0.15-0.60
ρ^0_{00}	0.18±0.08	0.11±0.06	0.21±0.06	0.03±0.06	0.19±0.06	0.19±0.07	0.00±0.07	0.02±0.06	0.20±0.07
ρ^0_{1-1}	0.03±0.09	-0.07±0.07	0.04±0.06	0.03±0.07	-0.07±0.06	-0.03±0.07	0.16±0.08	0.06±0.06	-0.05±0.07
Re ρ^0_{10}	-0.07±0.05	-0.05±0.04	0.06±0.04	0.01±0.04	-0.10±0.05	0.05±0.04	-0.03±0.05	0.01±0.04	0.01±0.06
ρ^1_{00}	0.28±0.13	0.00±0.10	0.12±0.09	-0.22±0.08	-0.03±0.10	0.19±0.11	-0.08±0.13	-0.13±0.11	-0.01±0.14
ρ^1_{11}	0.02±0.08	0.00±0.08	0.00±0.07	0.15±0.09	0.00±0.09	-0.07±0.08	0.09±0.12	0.14±0.10	0.05±0.10
ρ^1_{1-1}	0.05±0.13	-0.18±0.10	0.03±0.09	-0.13±0.12	0.21±0.10	0.11±0.11	0.38±0.14	0.29±0.12	0.54±0.13
Re ρ^1_{10}	-0.09±0.09	-0.04±0.06	-0.06±0.06	-0.20±0.06	-0.05±0.07	-0.20±0.07	0.04±0.08	-0.11±0.08	-0.02±0.10
Im ρ^2_{1-1}	-0.09±0.14	-0.04±0.10	-0.22±0.09	-0.01±0.10	-0.09±0.10	-0.04±0.11	-0.19±0.14	-0.29±0.14	-0.21-0.13
Im ρ^2_{10}	0.03±0.09	0.14±0.05	0.10±0.06	-0.05±0.06	0.09±0.07	0.02±0.06	0.01±0.09	0.10±0.08	0.12±0.09
P_σ	-0.2 ±0.3	-0.4 ±0.2	-0.1 ±0.2	0.0 ±0.3	0.4 ±0.2	0.0 ±0.2	0.9 ±0.3	0.7 ±0.3	1.1 ±0.3

TABLE X

Reaction $\gamma p \rightarrow p\Phi$ at 2.8, 4.7 and 9.3 GeV. Differential cross sections. The results from 2.8 and 4.7 GeV have been combined.

$\lvert t \rvert$ (GeV^2)	$\frac{d\sigma}{dt}$ (μb/GeV^2)	
	E_γ = 2.8 & 4.7 GeV	E_γ = 9.3 GeV
0.02 -0.2		1.5 ±0.3
0.045-0.2	1.22±0.22	
0.2 -0.4	0.44±0.12	0.68±0.15
0.4 -0.6	0.17±0.10	0.23±0.11
0.6 -0.8	0.24±0.10	0.15±0.10
0.8 -1.6	0.03±0.02	0.04±0.03

TABLE XI

Reaction $\gamma p \rightarrow p\Phi$ at 2.8, 4.7 and 9.3 GeV. Cross sections, forward differential cross sections and slope of the differential cross section from a fit of the form $d\sigma/dt = d\sigma/dt|_{t=0}\ e^{At}$ in $0.02 \leq |t| \leq 0.8\ GeV^2$. A_p is the slope expected for pure P exchange.[34]

E_γ (GeV)	2.8	4.7	9.3
$\sigma(\mu b)$	0.40±0.10	0.41±0.09	0.55±0.07
$\frac{d\sigma}{dt}\|_{t=0}$ ($\mu b/GeV^2$)	1.7 ±0.7	1.6 ±0.6	2.5 ±0.5
A (GeV^{-2})	3.7 ±1.2	3.7 ±1.0	4.6 ±0.7
A_p (GeV^{-2}) Ref. 34	3.2 ±0.1	4.1 ±0.15	5.3 ±0.1

TABLE XII

Reaction $\gamma p \rightarrow p\Phi$: Density matrix and parity asymmetry in the helicity system for $0.02 \leq |t| \leq 0.8$ GeV^2. Values of the asymmetry Σ from this and other experiments are also given.

	E_γ = 2.8 & 4.7 GeV	E_γ = 9.3 GeV
ρ^0_{00}	-0.04±0.06	0.00±0.07
Re ρ^0_{10}	-0.00±0.06	-0.01±0.06
ρ^0_{1-1}	-0.04±0.10	-0.14±0.09
ρ^1_{00}	-0.13±0.09	0.08±0.12
ρ^1_{11}	-0.06±0.11	-0.18±0.13
Re ρ^1_{10}	0.00±0.09	-0.20±0.11
ρ^1_{1-1}	0.18±0.13	0.44±0.15
Im ρ^2_{10}	-0.02±0.10	-0.14±0.09
Im ρ^2_{1-1}	-0.51±0.16	-0.73±0.17
P_σ	0.50±0.28	0.80±0.32
Σ	0.25±0.35	0.72±0.60
Σ Ref. 44	0.55±0.13[a]	at E_γ=5.7 GeV, $\|t\| \approx 0$
Σ Ref. 43	0.985±0.12	at E_γ=8.1 GeV, $\|t\|$=0.2 GeV^2

[a]Not corrected for background from inelastic Φ production (see Ref. 9).

FIGURE CAPTIONS

1. Reaction $\gamma p \to p\pi^+\pi^-$ at 9.3 GeV. (a) Dalitz plot distribution for $|t| > 0.02$ GeV^2. (b) Chew Low plot for $\pi^+\pi^-$.

2. Reaction $\gamma p \to p\pi^+\pi^-$ at 9.3 GeV. Distributions of the $\pi^+\pi^-$ mass for different t intervals. The helicity conserving p-wave intensity, Π, is shown by the solid points. The curves give the result of a maximum likelihood fit to the reaction using the Söding model.

3. Reaction $\gamma p \to p\pi^+\pi^-$ at 9.3 GeV. Distribution of the $\pi^+\pi^-$, $p\pi^+$ and $p\pi^-$ effective masses. The shaded histograms represent events with $|t_{p/p\pi^\pm}| < 0.4$ GeV^2 and $M_{\pi^+\pi^-} > 1$ GeV. The curves give the result of a maximum likelihood fit to the reaction using the Söding model.

4. Reaction $\gamma p \to p\pi^+\pi^-$ at 2.8, 4.7, 9.3 GeV. Distribution of $\pi^+\pi^-$ effective mass in logarithmic scale. Events in the Δ^{++} mass region ($M_{p\pi^+} < 1.38$ GeV) are excluded. The right-hand ordinate scale gives the cross section $d\sigma/dM_{\pi^+\pi^-}$ corresponding to the histograms shown.

5. Reaction $\gamma p \to p\rho^o$ at 9.3 GeV. Fitted values for n(t) using the parameterization Breit-Wigner times $(M_\rho/M_{\pi^+\pi^-})^{n(t)}$ for the ρ^o shape.

6. Reaction $\gamma p \to p\pi^+\pi^-$ at 9.3 GeV. Results of fits of the form $d\sigma^2/dtdM_{\pi\pi} = d\sigma^2/dtdM_{\pi\pi}|_{t=0} \cdot e^{At}$ in the interval $0.02 \leq |t| \leq 0.5$ GeV^2. The curve in (b) is from the Söding model.

7. Reaction $\gamma p \to p\rho^o$ at 9.3 GeV. Decay angular distribution of events in the ρ^o region in the helicity system. The curves are calculated for an s-channel helicity conserving $\gamma \to \rho^o$ transition and incident photon polarization of 77%.

8. Reaction $\gamma p \to p\pi^+\pi^-$ at 9.3 GeV. The dipion moments $Y_2^0(\theta,\psi)$, Re $Y_2^2(\theta,\psi)$ and $Y_4^0(\theta,\psi)$ in the helicity system as a function of $M_{\pi^+\pi^-}$ for $0.02 \leq |t| \leq 0.8$ GeV^2. The curves were obtained from the Söding model.

16. Reaction $\gamma p \rightarrow p\pi^+\pi^- MM$ at 2.8, 4.7, 9.3 GeV. (a) Distribution of the square of the missing mass MM^2 for 3-prong events not fitting $\gamma p \rightarrow p\pi^+\pi^-$, $\gamma p \rightarrow pK^+K^-$ or $\gamma p \rightarrow pp\bar{p}$ and consistent with $\gamma p \rightarrow p\pi^+\pi^-\pi^o$. (b) $\pi^+\pi^-\pi^o$ mass distribution from a OC calculation for events in (a) with $MM^2 < 0.1$ GeV^2. At 2.8, 4.7 GeV a selection was also made on the calculated photon energy ($2.4 \leq E_\gamma \leq 3.3$ GeV and $4.1 \leq E_\gamma \leq 5.3$ GeV, respectively).

17. Reaction $\gamma p \rightarrow p\pi^+\pi^-\pi^o$ at 2.8, 4.7, 9.3 GeV. Scatter plots of $\pi^+\pi^-\pi^o$ mass versus momentum transfer t.

18. Reaction $\gamma p \rightarrow p\pi^+\pi^-\pi^o$ at 2.8, 4.7, 9.3 GeV. (a) Slope A of the t-distribution of the $\pi^+\pi^-\pi^o$ system as calculated from a fit of the form e^{At} as a function of $\pi^+\pi^-\pi^o$ mass. (b), (c) Moments $Y_2^0(\theta)$, Re $Y_2^2(\theta, \psi)$ of the $\pi^+\pi^-\pi^o$ system in the helicity system as a function of $\pi^+\pi^-\pi^o$ mass.

19. Reaction $\gamma p \rightarrow p\omega$ at 2.8, 4.7, 9.3 GeV. Differential cross sections ($\blacklozenge$) and natural parity exchange contributions to the differential cross section ($-\frac{1}{1}-$).

20. Reaction $\gamma p \rightarrow p\omega$. Total cross sections as a function of the incident photon energy. The points labeled ABBHHM, SLAC Annihilation Beam are from Refs. 5, 6 respectively. Also shown are the contributions of natural and unnatural parity exchange in the t-channel. The full and dashed curves give the contributions of a diffractive process and OPE, respectively, as obtained from the fit described in the text.

21. Reaction $\gamma p \rightarrow p\omega$ at 2.8, 4.7, 9.3 GeV. Decay angular distributions in the helicity system and parity asymmetry P_σ for events in the ω mass region $0.74 \leq M_{\pi^+\pi^-\pi^o} \leq 0.84$ GeV and in the momentum transfer interval $0.02 \leq |t| \leq 0.3$ GeV^2. Curves are calculated from the fitted density matrix elements (see text).

22. Reaction $\gamma p \rightarrow p\omega$ at 2.8, 4.7, 9.3 GeV. Density matrix elements in the helicity system and parity asymmetry as a function of momentum transfer t.

23. Reaction $\gamma p \rightarrow p\omega$ at 2.8, 4.7, 9.3 GeV. (a) Density matrix elements of the natural parity exchange contribution in the helicity system. (b) Density matrix elements of the unnatural parity exchange contribution in the Gottfried-Jackson system.

24. Reaction $\gamma p \rightarrow pK^+K^-$ at 2.8, 4.7, 9.3 GeV. Distribution of the K^+K^- mass for $|t| > 0.02$ GeV^2. The curves in the inset are from a fit of a p-wave Breit-Wigner distribution with measuring resolution folded in.

25. Reaction $\gamma p \rightarrow pK^+K^-$ at 2.8, 4.7, 9.3 GeV. Distribution of the pK^+ and pK^- mass for $|t| > 0.02$ GeV^2. Shaded distributions are for $M_{K^+K^-} > 1.04$ GeV.

26. Reaction $\gamma p \rightarrow pK_S^0K_L^0$ at 2.8, 4.7, 9.3 GeV. Distribution of the $K_S^0K_L^0$ mass. Shaded distributions are for $|t| \leq 1.0$ GeV^2.

27. Reaction $\gamma p \rightarrow p\Phi$ at 2.8, 4.7, 9.3 GeV. Differential cross section: (a) 2.8 and 4.7 GeV data combined, (b) 9.3 GeV. The data points labeled ABBHHM, DESY-MIT, Berger et al. and Anderson et al. are from Refs. 5, 42, 9, 8, 43 respectively.

28. Reaction $\gamma p \rightarrow p\Phi$. Total cross section and exponential slope A of the differential cross section as a function of the incident photon energy. Data points labeled ABBHHM and Berger et al. are from Refs. 5, 9 respectively.

29. Reaction $\gamma p \rightarrow p\Phi$ at 2.8, 4.7, 9.3 GeV. Decay angular distribution of $K\bar{K}$ pairs in the helicity system in the Φ mass region $1.00 \leq M_{K\bar{K}} \leq 1.04$ GeV and in the momentum transfer interval $0.02 \leq |t| \leq 0.8$ GeV^2. The

curves are calculated for an s-channel helicity conserving Φ production amplitude.

30. Comparison between photoproduction and Compton scattering at 2.8, 4.7, 9.3 GeV. Relation (13) was used with C=2. The errors on the photoproduction points include a 15 percent uncertainty due to the differences in the ρ^0 cross sections derived by different methods. Compton scattering data were taken from Ref. 51 and the optical points from this experiment.[1,20]

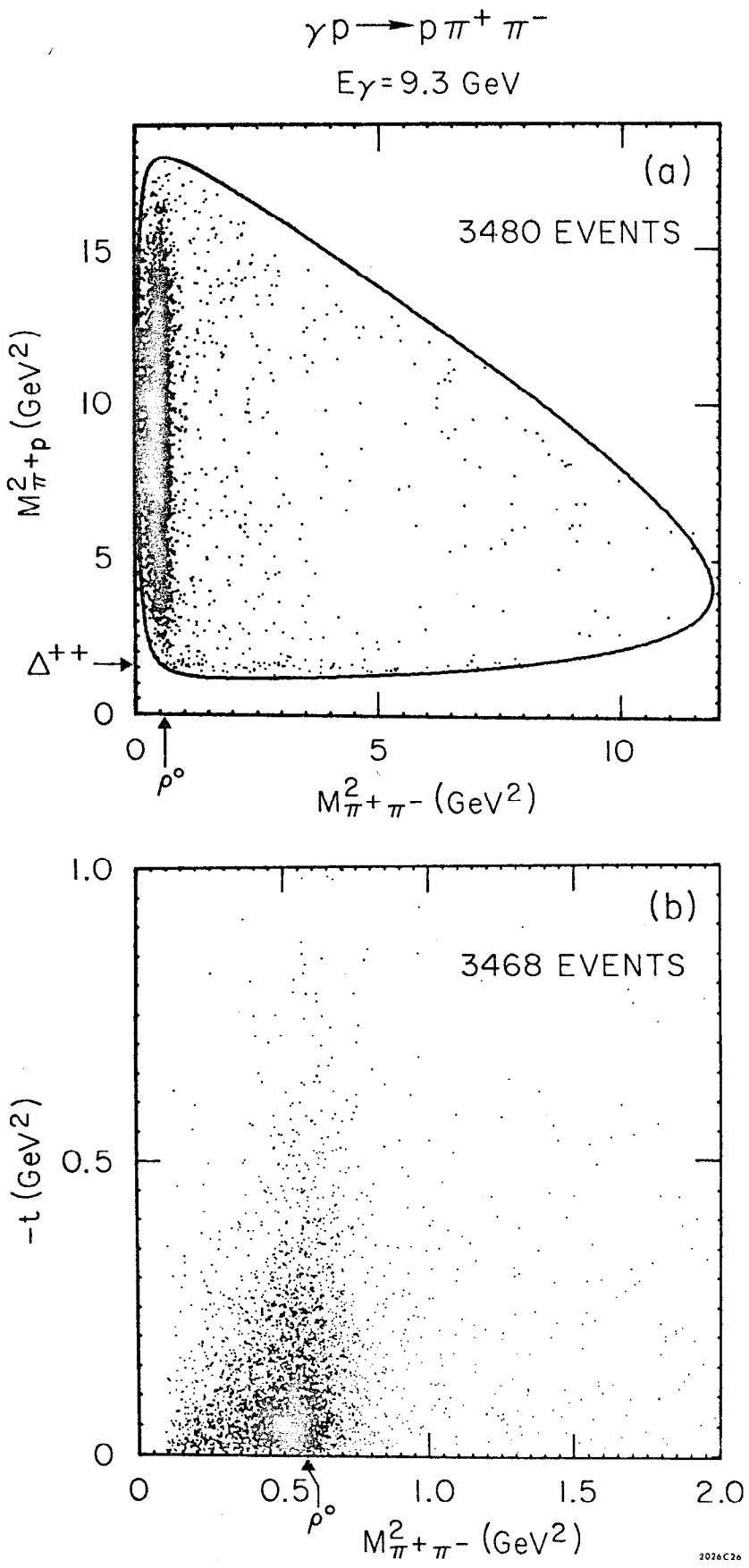
γp → pπ+π−
Eγ = 9.3 GeV
(a)
3480 EVENTS
15
10
5
0
Δ++
0
5
10
ρ°
M²π+p (GeV²)
M²π+π− (GeV²)
(b)
3468 EVENTS
1.0
0.5
0
−t (GeV²)
0
0.5
1.0
1.5
2.0
ρ°
M²π+π− (GeV²)
2026C26

Fig. 1

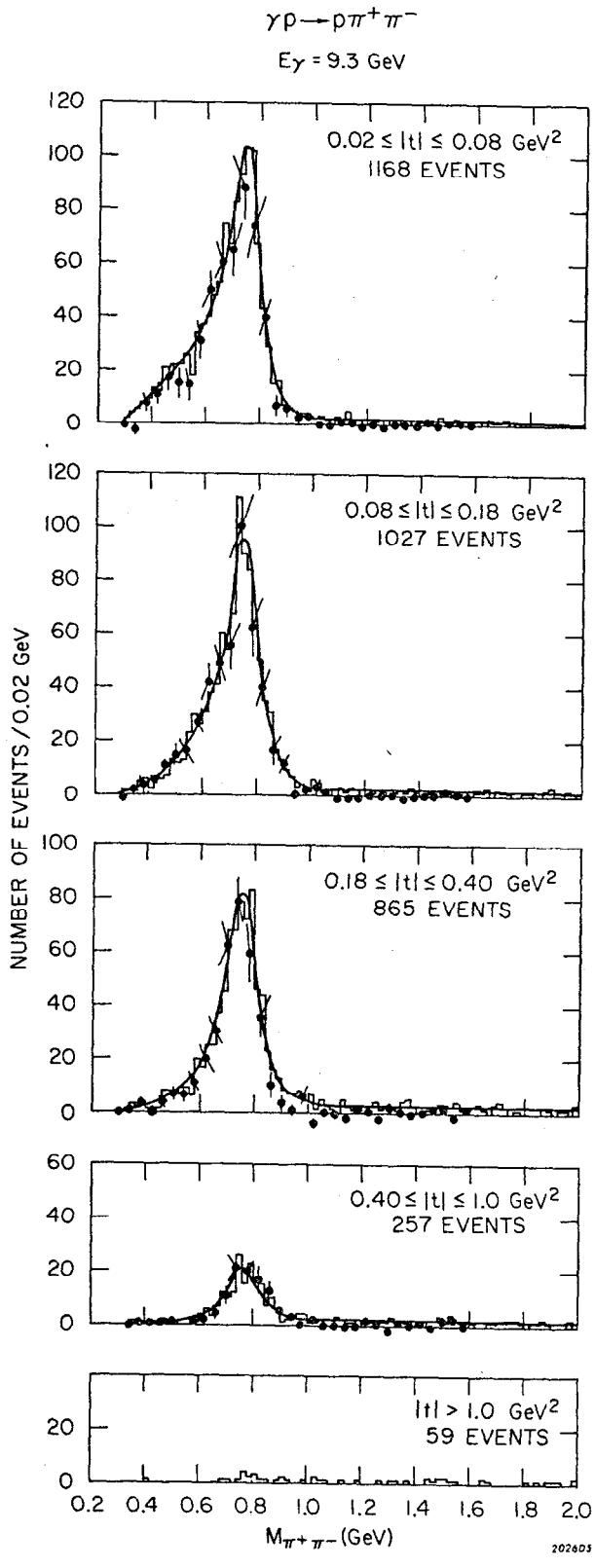
γp→pπ+π−
Eγ = 9.3 GeV
0.02 ≤ |t| ≤ 0.08 GeV2
1168 EVENTS
0.08 ≤ |t| ≤ 0.18 GeV2
1027 EVENTS
0.18 ≤ |t| ≤ 0.40 GeV2
865 EVENTS
0.40 ≤ |t| ≤ 1.0 GeV2
257 EVENTS
|t| > 1.0 GeV2
59 EVENTS
NUMBER OF EVENTS/0.02 GeV
Mπ+π− (GeV)
202603

Fig. 2

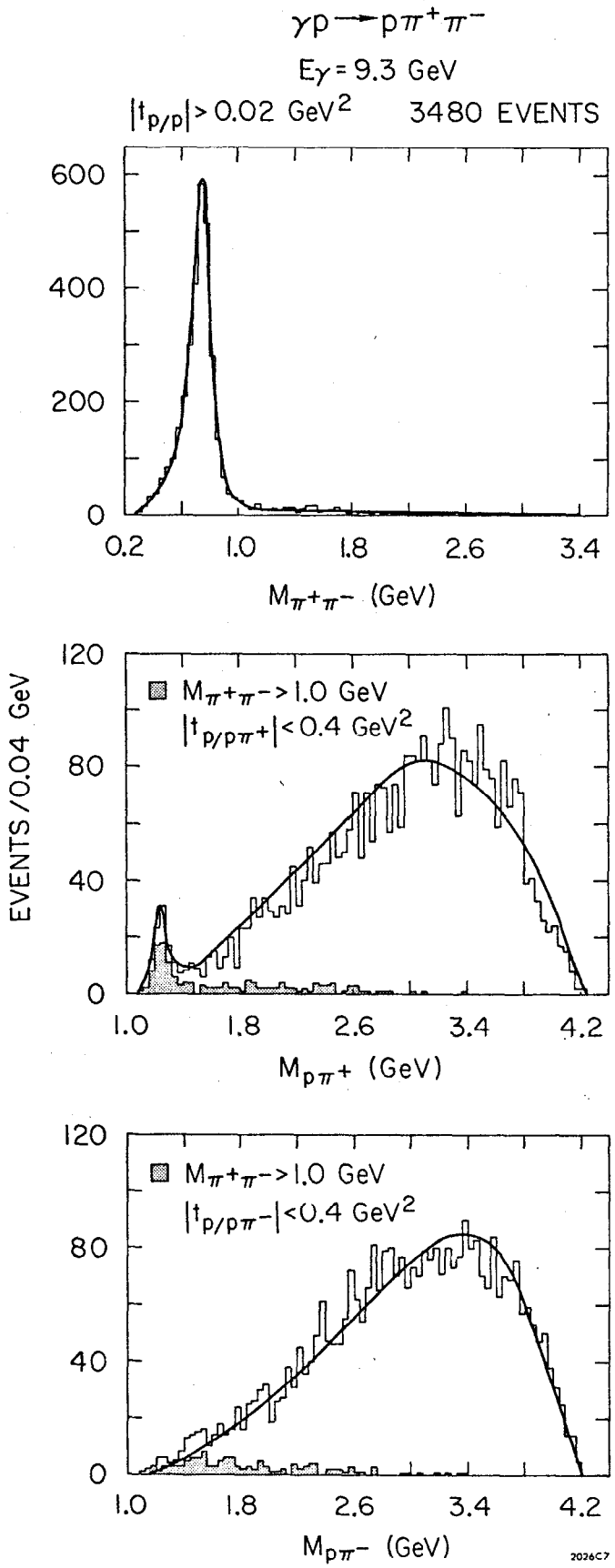
γp → pπ+π−
Eγ = 9.3 GeV
|tp/p| > 0.02 GeV2
3480 EVENTS
600
400
200
0
0.2
1.0
1.8
2.6
3.4
Mπ+π− (GeV)
EVENTS/0.04 GeV
120
80
40
0
Mπ+π− > 1.0 GeV
|tp/pπ+| < 0.4 GeV2
1.0
1.8
2.6
3.4
4.2
Mpπ+ (GeV)
Mπ+π− > 1.0 GeV
|tp/pπ−| < 0.4 GeV2
Mpπ− (GeV)
2026C7

Fig. 3

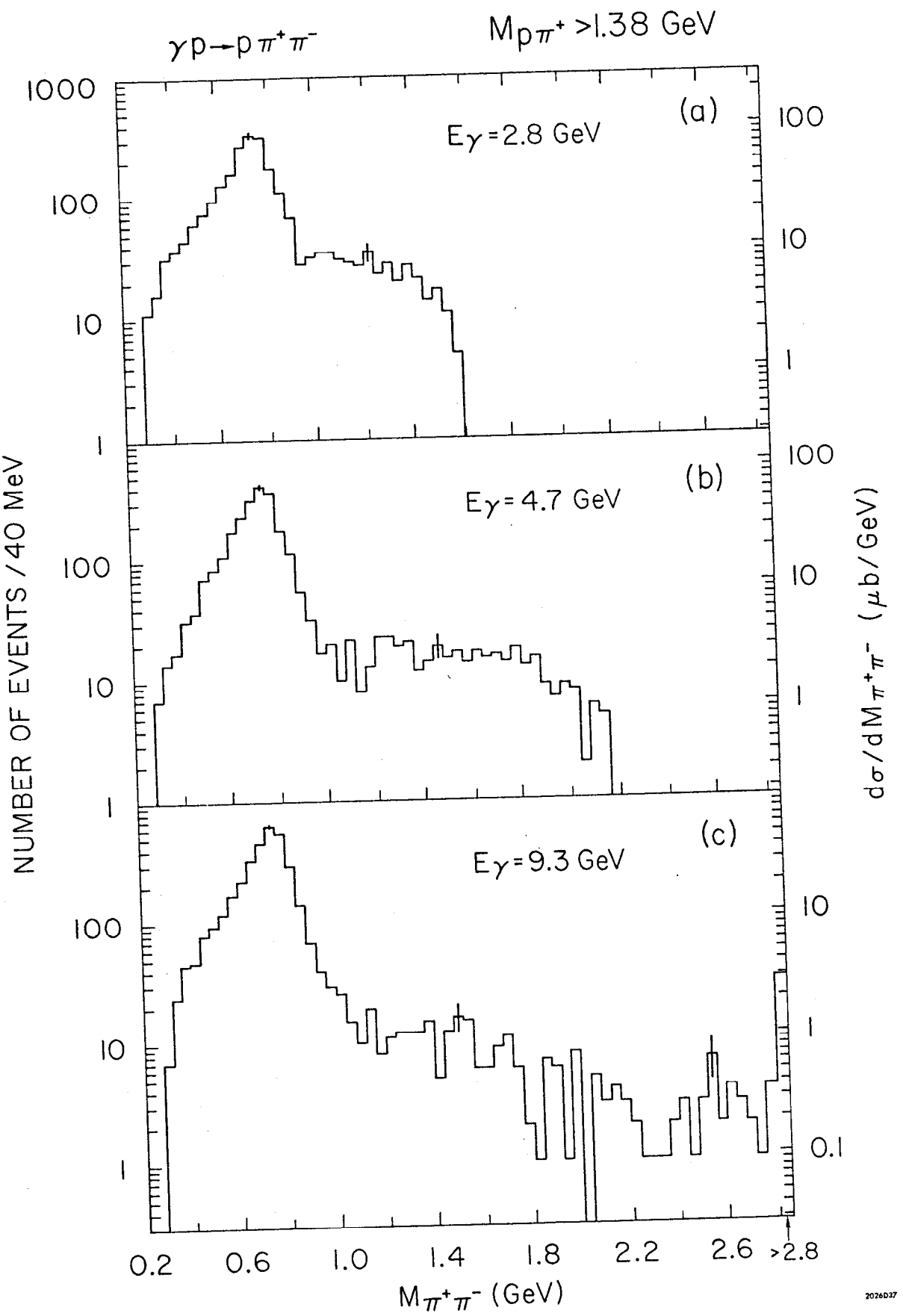
γp→pπ⁺π⁻
Mpπ⁺ >1.38 GeV
(a)
Eγ=2.8 GeV
(b)
Eγ=4.7 GeV
(c)
Eγ=9.3 GeV
NUMBER OF EVENTS / 40 MeV
dσ/dMπ⁺π⁻ (μb/GeV)
Mπ⁺π⁻ (GeV)
0.2
0.6
1.0
1.4
1.8
2.2
2.6
>2.8
2026D37

Fig. 4

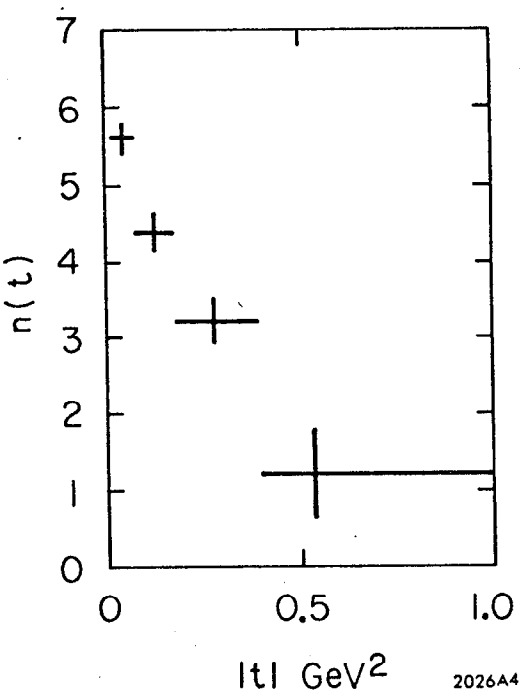

Fig. 5

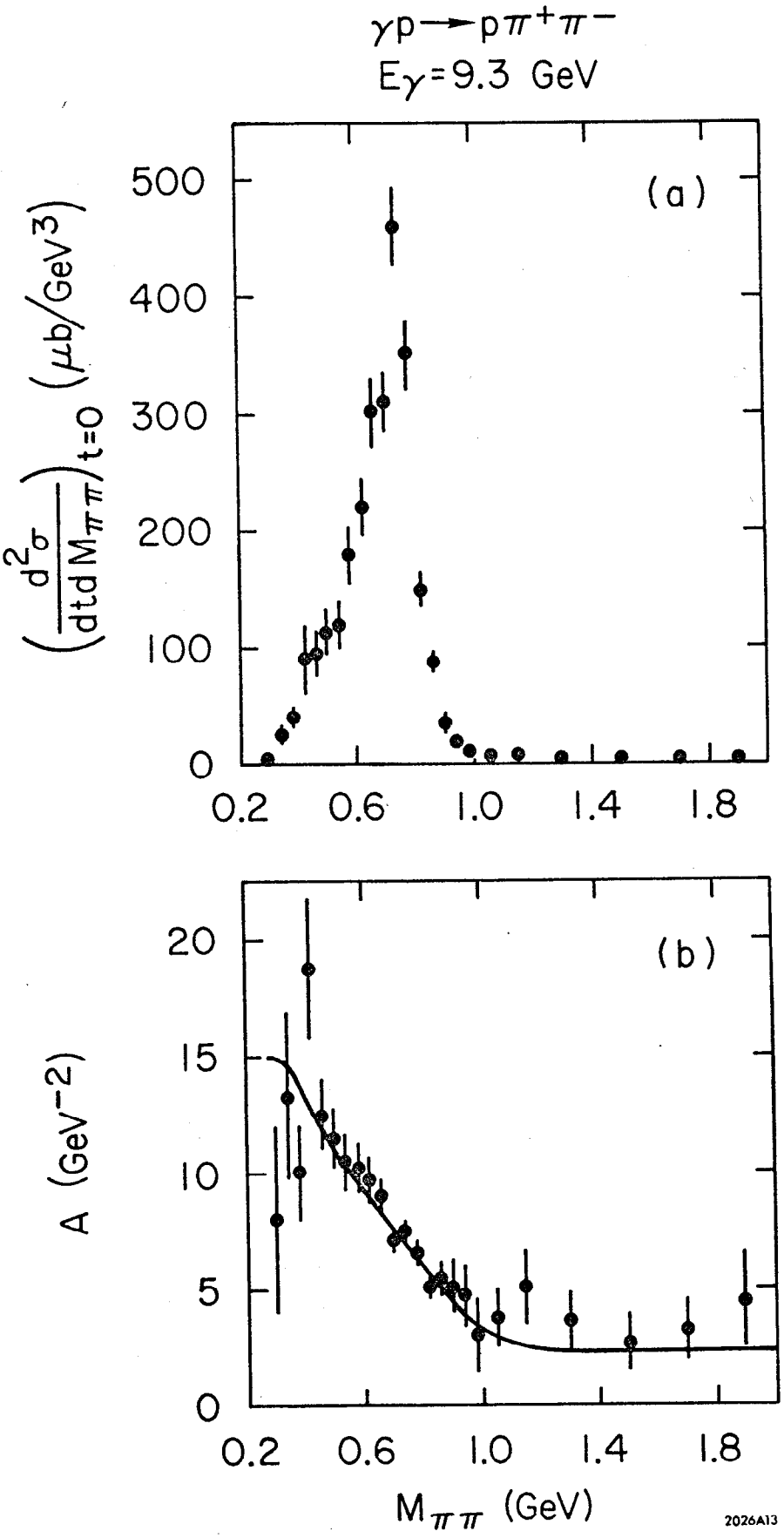
γp → pπ+π−
Eγ = 9.3 GeV
(a)
$\left(\frac{d^2\sigma}{dt\,dM_{\pi\pi}}\right)_{t=0}$ (μb/GeV3)
500
400
300
200
100
0
0.2
0.6
1.0
1.4
1.8
(b)
A (GeV−2)
20
15
10
5
0
0.2
0.6
1.0
1.4
1.8
Mππ (GeV)
2026A13

Fig. 6

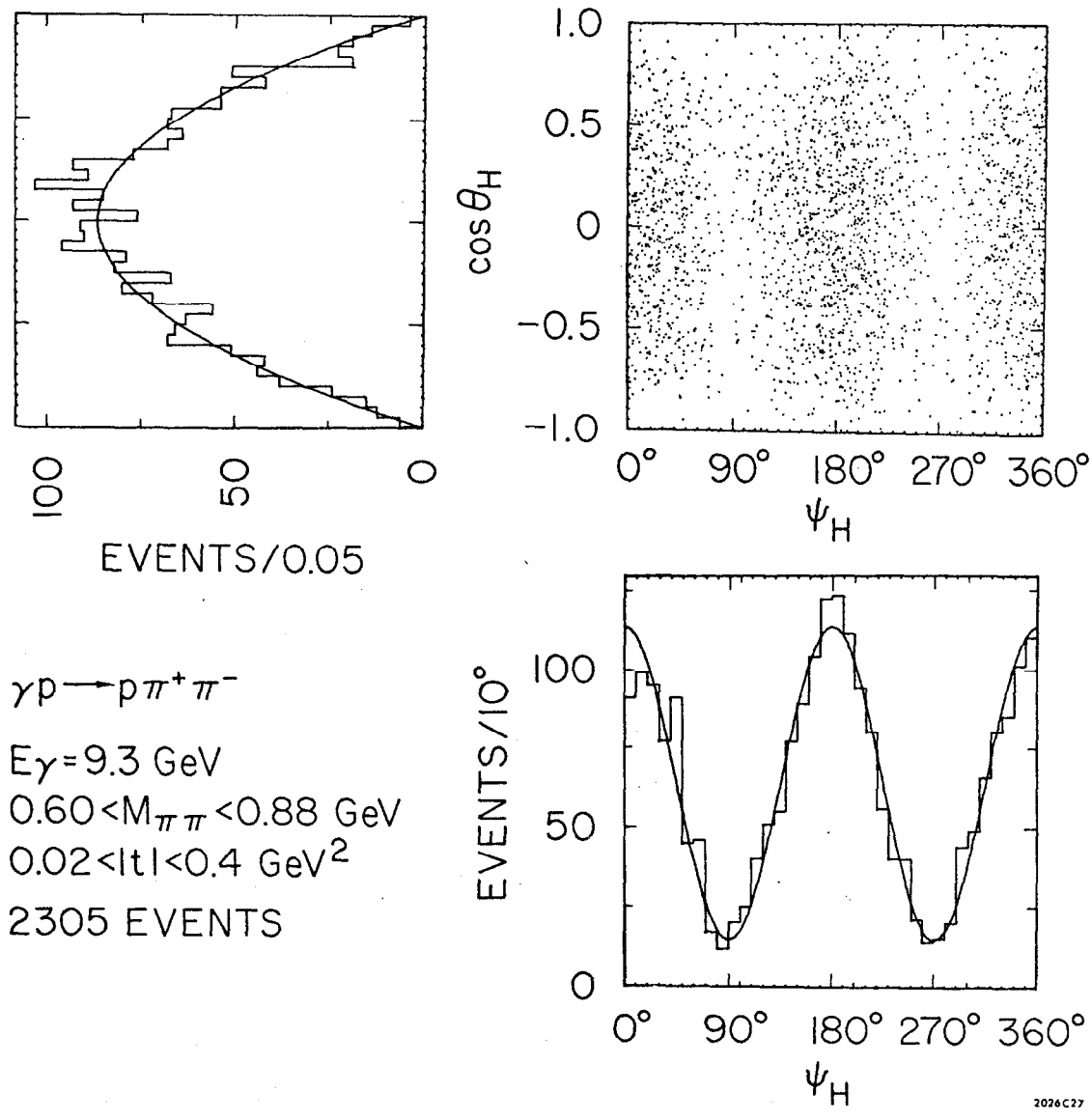
100
50
0
EVENTS/0.05
1.0
0.5
0
-0.5
-1.0
cos θH
0° 90° 180° 270° 360°
ψH
γp → pπ+π−
Eγ=9.3 GeV
0.60<Mππ<0.88 GeV
0.02<|t|<0.4 GeV2
2305 EVENTS
EVENTS/10°
100
50
0
0° 90° 180° 270° 360°
ψH
2026C27

Fig. 7

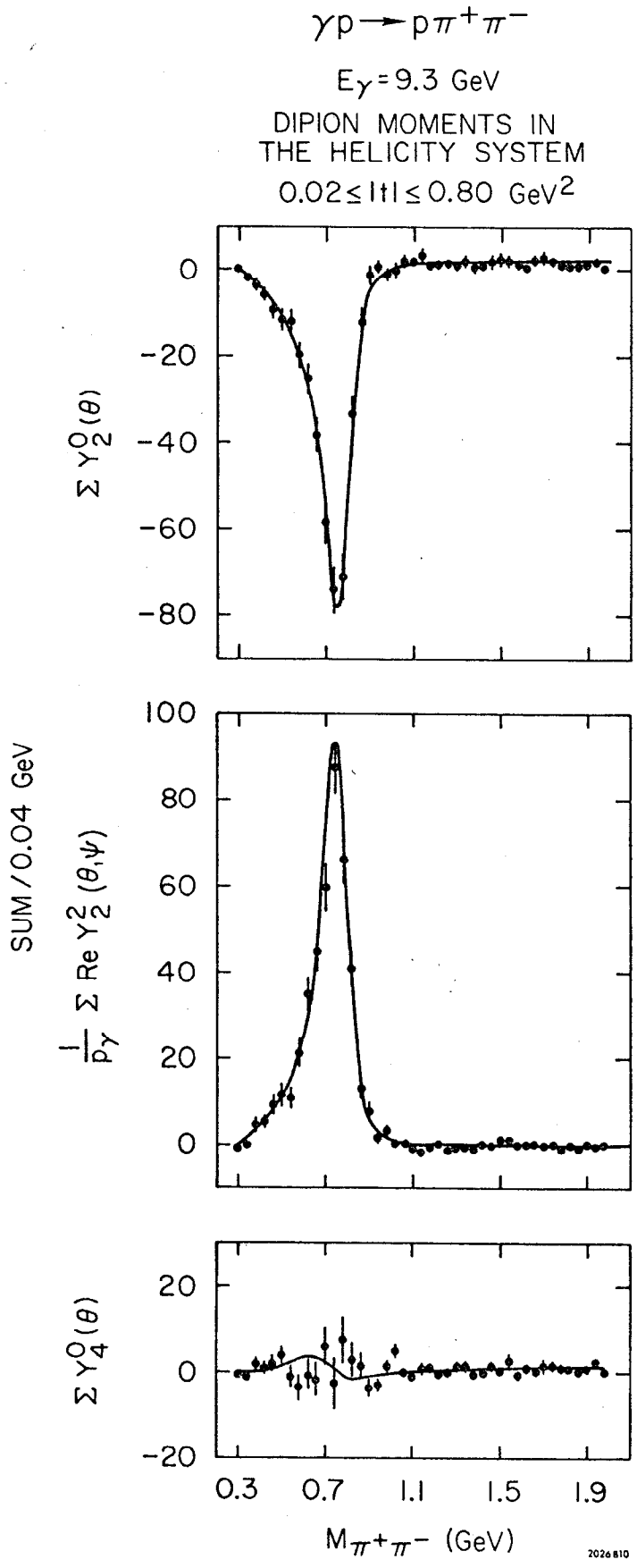
$\gamma p \rightarrow p\pi^+\pi^-$
$E_\gamma = 9.3$ GeV
DIPION MOMENTS IN
THE HELICITY SYSTEM
$0.02 \leq |t| \leq 0.80$ GeV^2
$\Sigma Y_2^0(\theta)$
0
-20
-40
-60
-80
SUM/0.04 GeV
$\frac{1}{p_\gamma} \Sigma \text{Re}\, Y_2^2(\theta,\psi)$
100
80
60
40
20
0
$\Sigma Y_4^0(\theta)$
20
0
-20
0.3
0.7
1.1
1.5
1.9
$M_{\pi^+\pi^-}$ (GeV)
2026810

Fig. 8

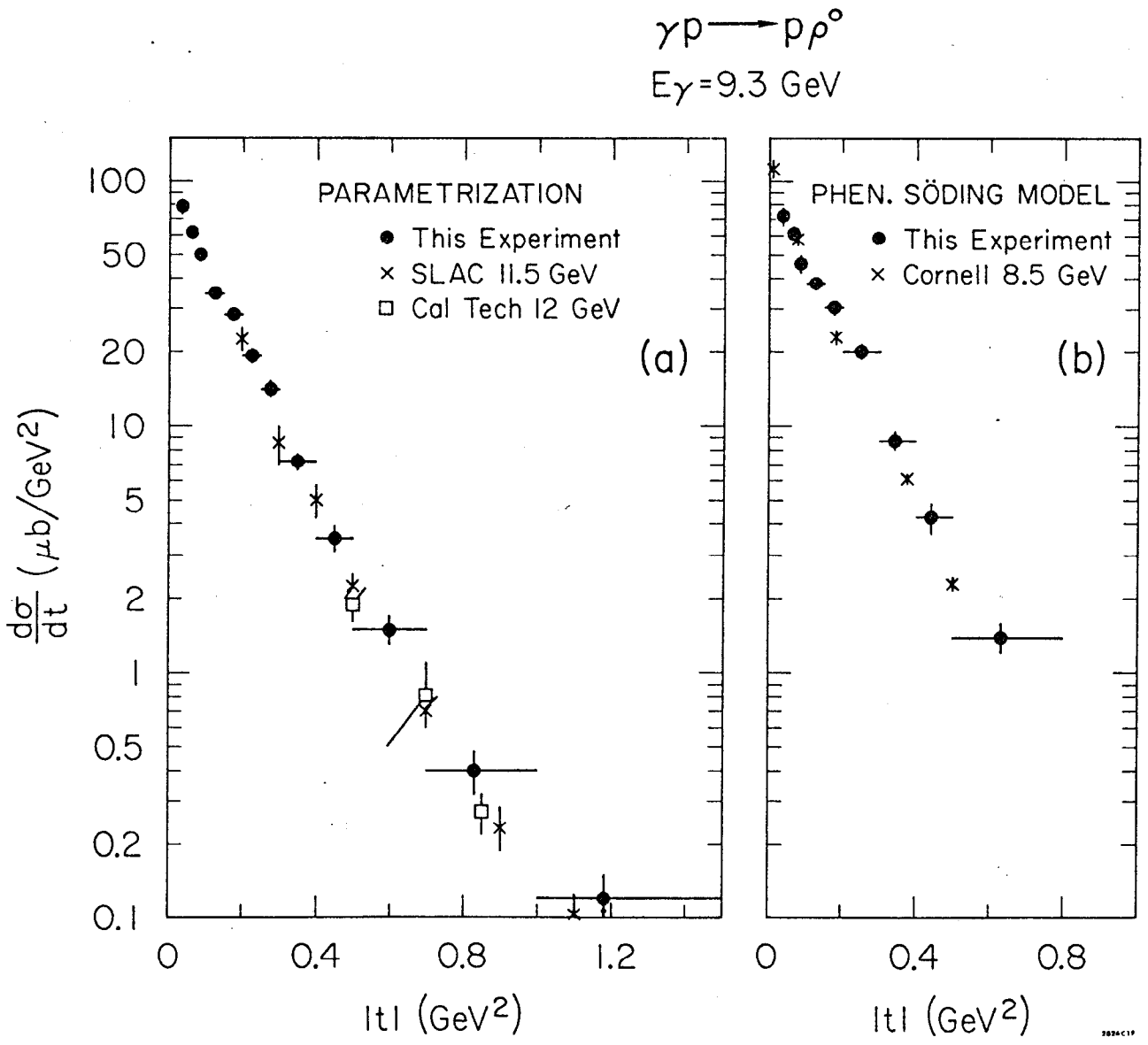
γp ⟶ pρ°
Eγ = 9.3 GeV
PARAMETRIZATION
This Experiment
SLAC 11.5 GeV
Cal Tech 12 GeV
(a)
PHEN. SÖDING MODEL
This Experiment
Cornell 8.5 GeV
(b)
dσ/dt (μb/GeV²)
100
50
20
10
5
2
1
0.5
0.2
0.1
0
0.4
0.8
1.2
|t| (GeV²)

Fig. 9

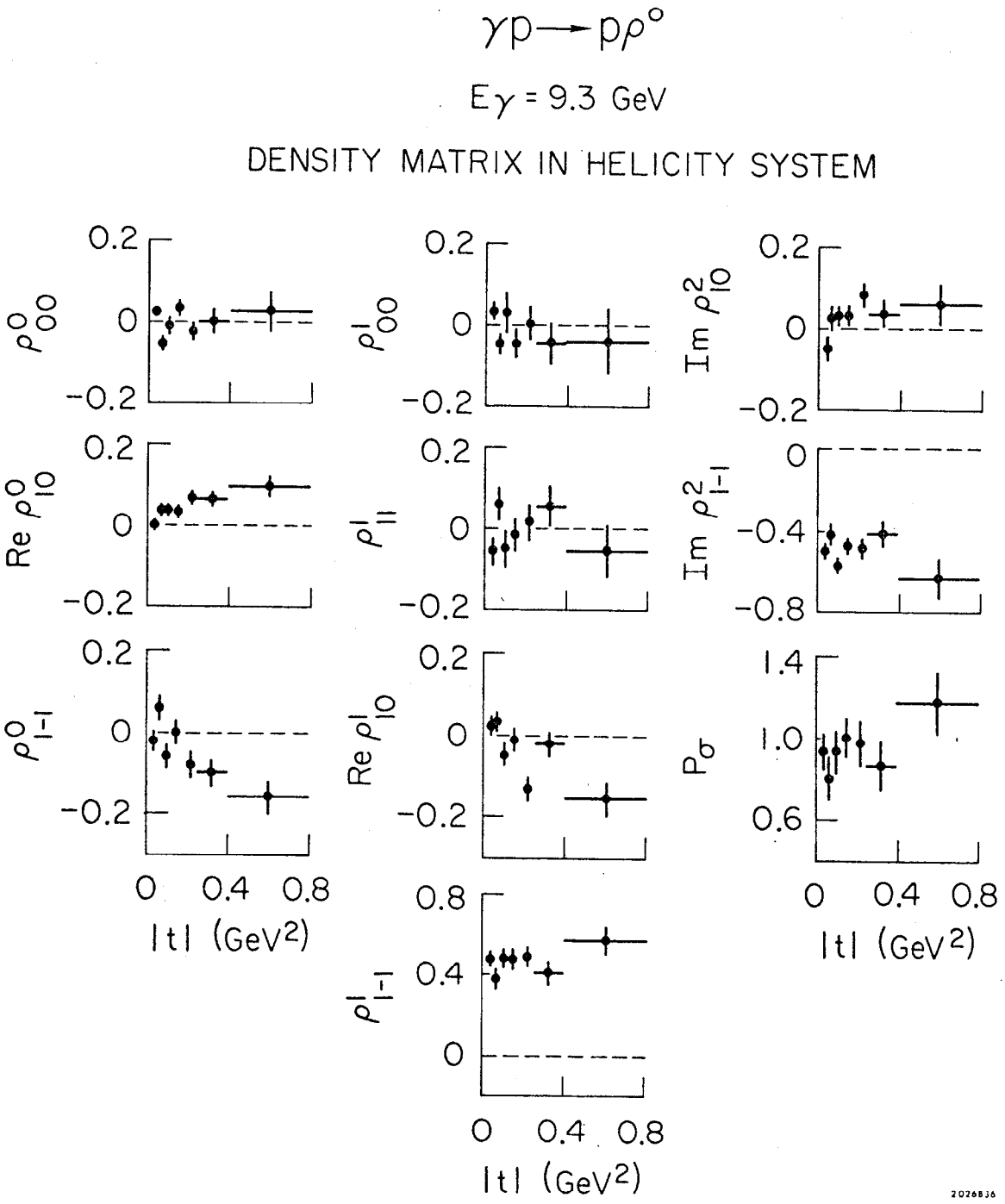
γp → pρ°
Eγ = 9.3 GeV
DENSITY MATRIX IN HELICITY SYSTEM
ρ^0_{00}
ρ^1_{00}
Im ρ^2_{10}
Re ρ^0_{10}
ρ^1_{11}
Im ρ^2_{1-1}
ρ^0_{1-1}
Re ρ^1_{10}
P_σ
ρ^1_{1-1}
0.2
0
-0.2
0.4
-0.4
0.8
-0.8
1.4
1.0
0.6
0 0.4 0.8
|t| (GeV²)
2026836

Fig. 10

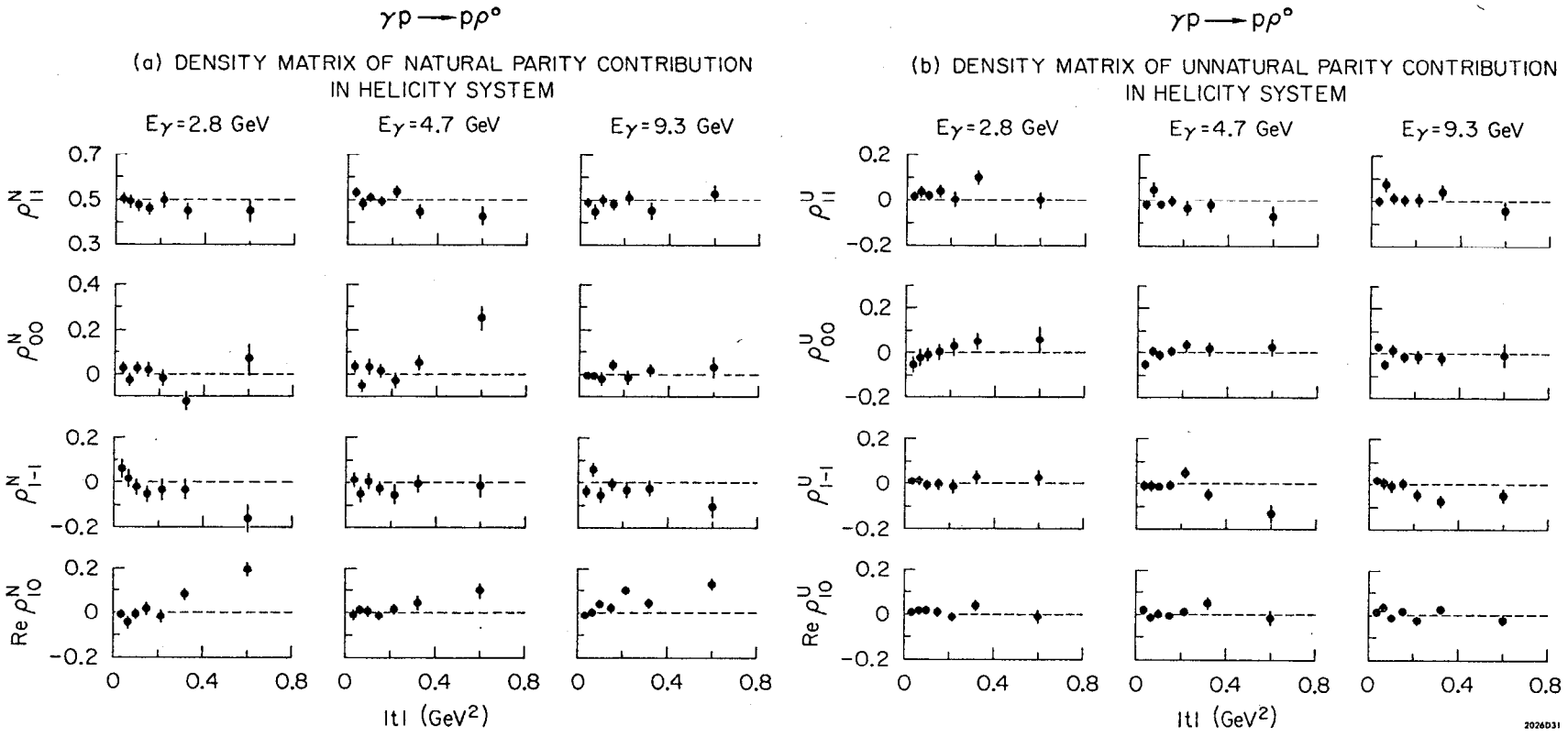
γp → pρ°
(a) DENSITY MATRIX OF NATURAL PARITY CONTRIBUTION IN HELICITY SYSTEM
Eγ=2.8 GeV
Eγ=4.7 GeV
Eγ=9.3 GeV
ρ^N_{11}
ρ^N_{00}
ρ^N_{1-1}
Re ρ^N_{10}
0.7
0.5
0.3
0.4
0.2
0
-0.2
0
0.4
0.8
|t| (GeV²)
γp → pρ°
(b) DENSITY MATRIX OF UNNATURAL PARITY CONTRIBUTION IN HELICITY SYSTEM
Eγ=2.8 GeV
Eγ=4.7 GeV
Eγ=9.3 GeV
ρ^U_{11}
ρ^U_{00}
ρ^U_{1-1}
Re ρ^U_{10}
0.2
0
-0.2
0
0.4
0.8
|t| (GeV²)
2026D31

Fig. 11

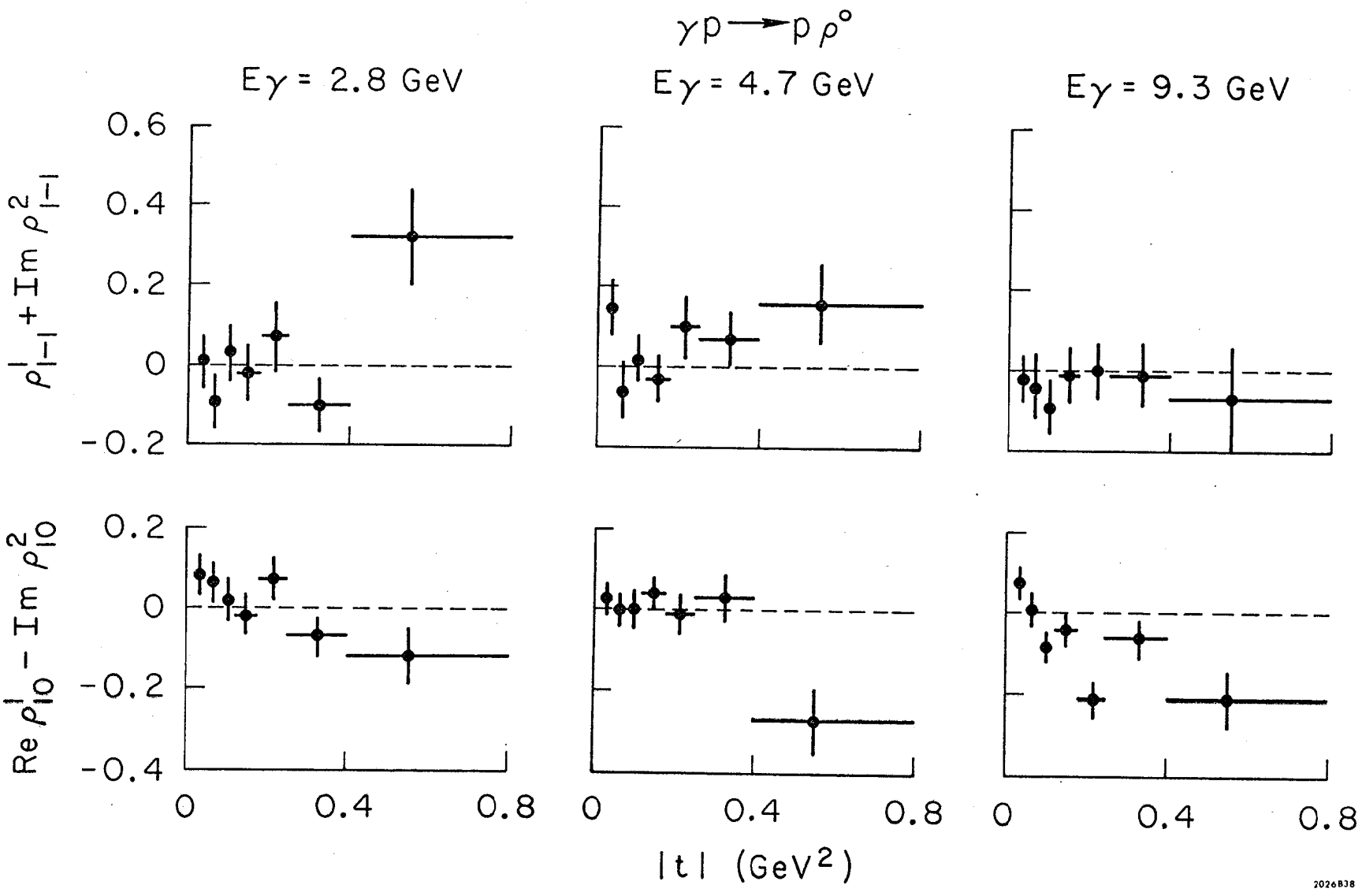
γp → pρ°
Eγ = 2.8 GeV
Eγ = 4.7 GeV
Eγ = 9.3 GeV
$\rho^1_{1-1} + \mathrm{Im}\,\rho^2_{1-1}$
$\mathrm{Re}\,\rho^1_{10} - \mathrm{Im}\,\rho^2_{10}$
0.6
0.4
0.2
0
-0.2
0.2
0
-0.2
-0.4
0
0.4
0.8
|t| (GeV²)
2026B38

Fig. 12

$\gamma p \rightarrow p\pi^+\pi^-$

$E\gamma = 9.3$ GeV

DENSITY MATRIX ELEMENTS IN THE HELICITY SYSTEM

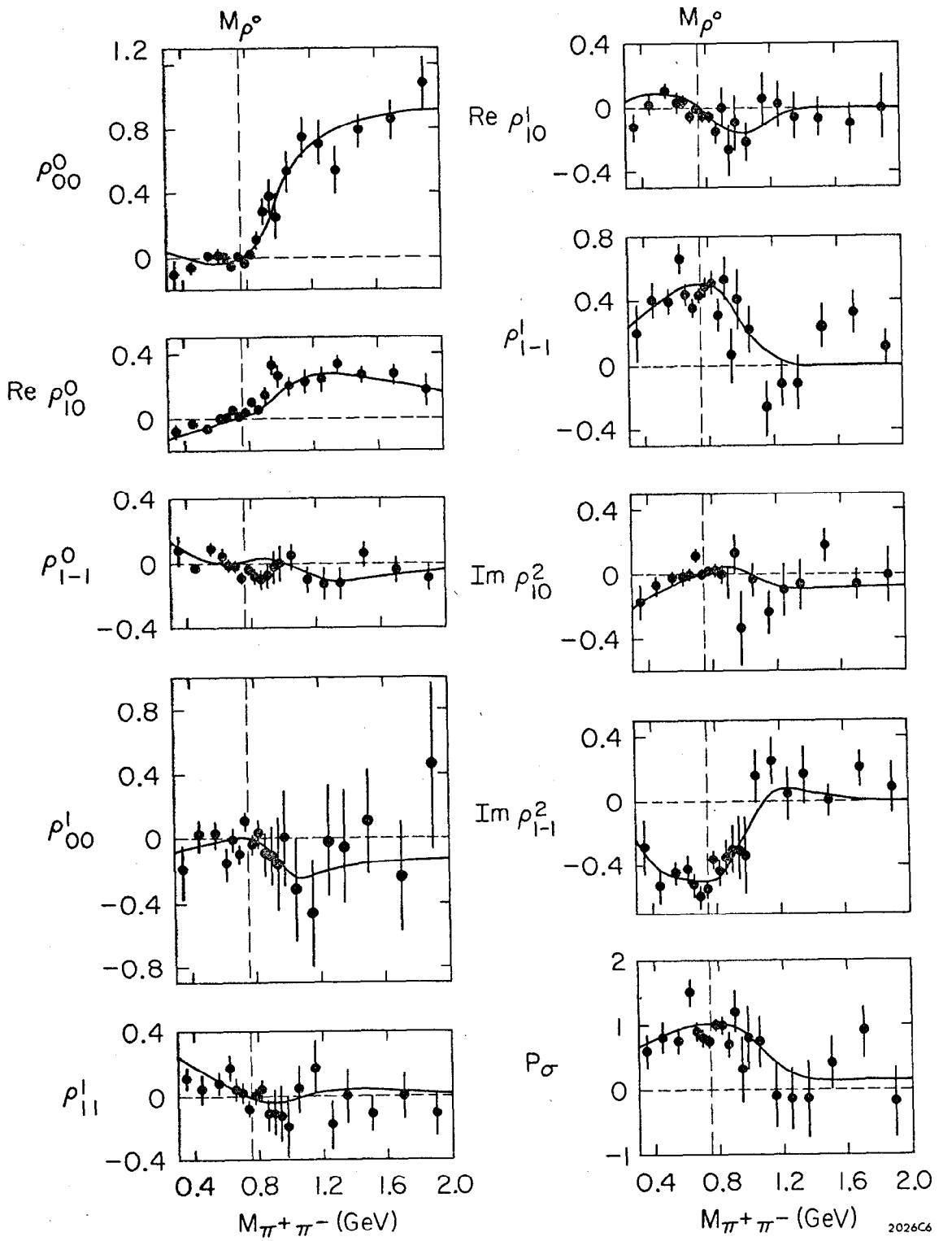

Fig. 13

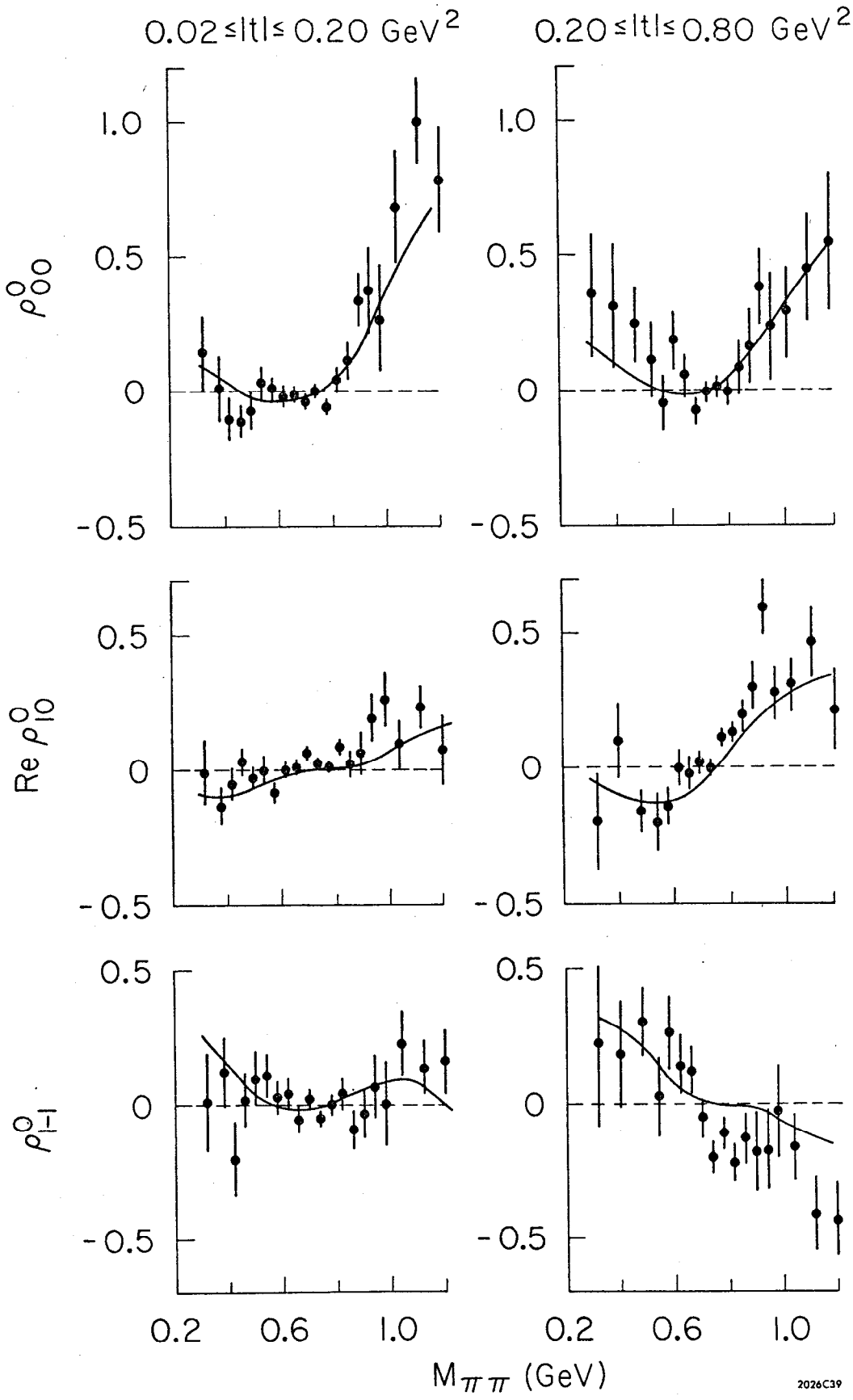
0.02≤|t|≤0.20 GeV²
0.20≤|t|≤0.80 GeV²
ρ^0_{00}
Re ρ^0_{10}
ρ^0_{1-1}
1.0
0.5
0
-0.5
0.2
0.6
1.0
$M_{\pi\pi}$ (GeV)
2026C39

Fig. 14

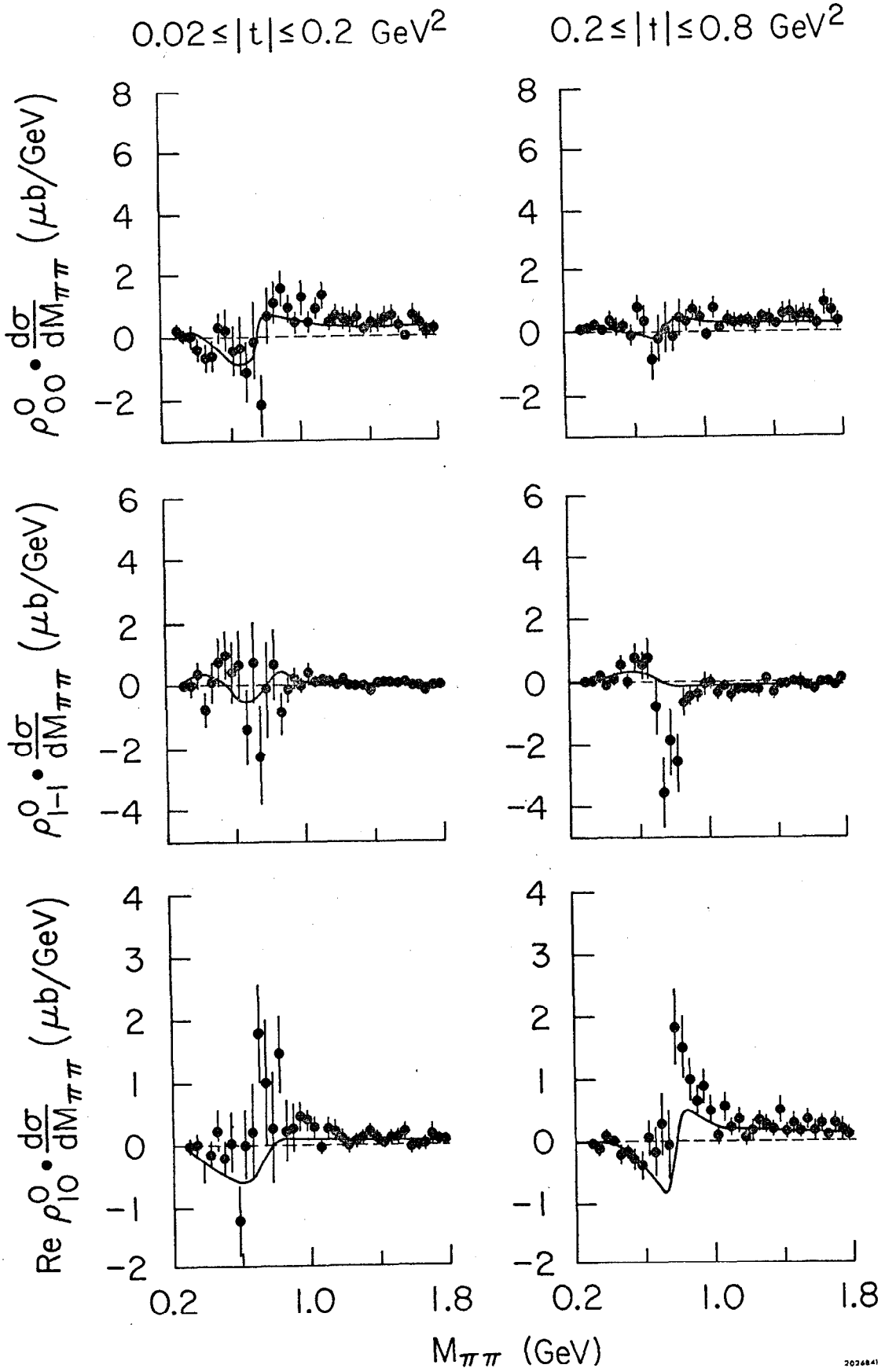
0.02≤|t|≤0.2 GeV²
0.2≤|t|≤0.8 GeV²
$\rho^0_{00} \bullet \frac{d\sigma}{dM_{\pi\pi}}$ (μb/GeV)
$\rho^0_{1-1} \bullet \frac{d\sigma}{dM_{\pi\pi}}$ (μb/GeV)
Re $\rho^0_{10} \bullet \frac{d\sigma}{dM_{\pi\pi}}$ (μb/GeV)
$M_{\pi\pi}$ (GeV)
0.2
1.0
1.8
2026841

Fig. 15

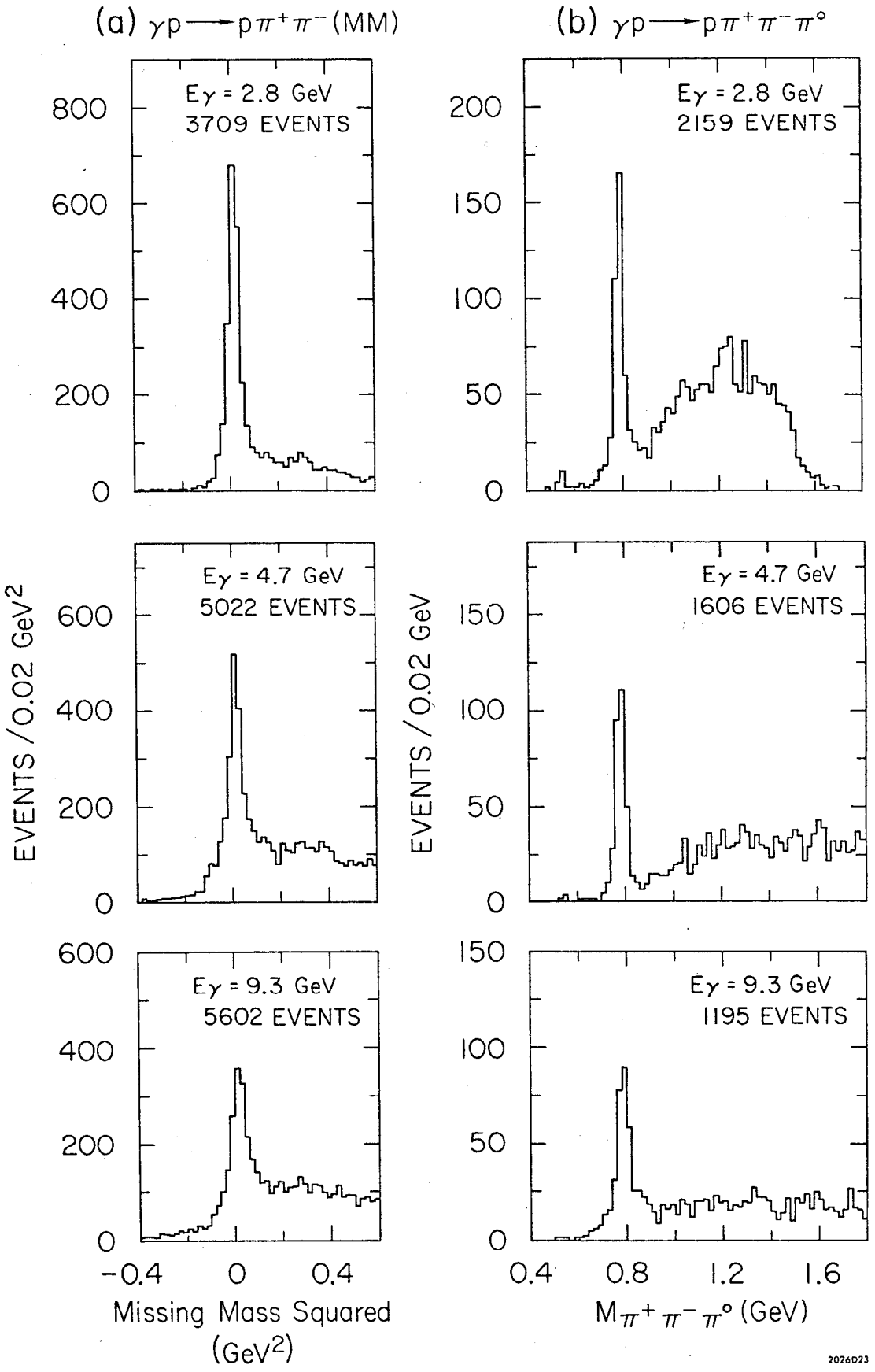
(a) γp → pπ+π−(MM)
(b) γp → pπ+π−π°
Eγ = 2.8 GeV
3709 EVENTS
Eγ = 2.8 GeV
2159 EVENTS
Eγ = 4.7 GeV
5022 EVENTS
Eγ = 4.7 GeV
1606 EVENTS
Eγ = 9.3 GeV
5602 EVENTS
Eγ = 9.3 GeV
1195 EVENTS
EVENTS / 0.02 GeV²
EVENTS / 0.02 GeV
Missing Mass Squared (GeV²)
Mπ+π−π° (GeV)
2026D23

Fig. 16

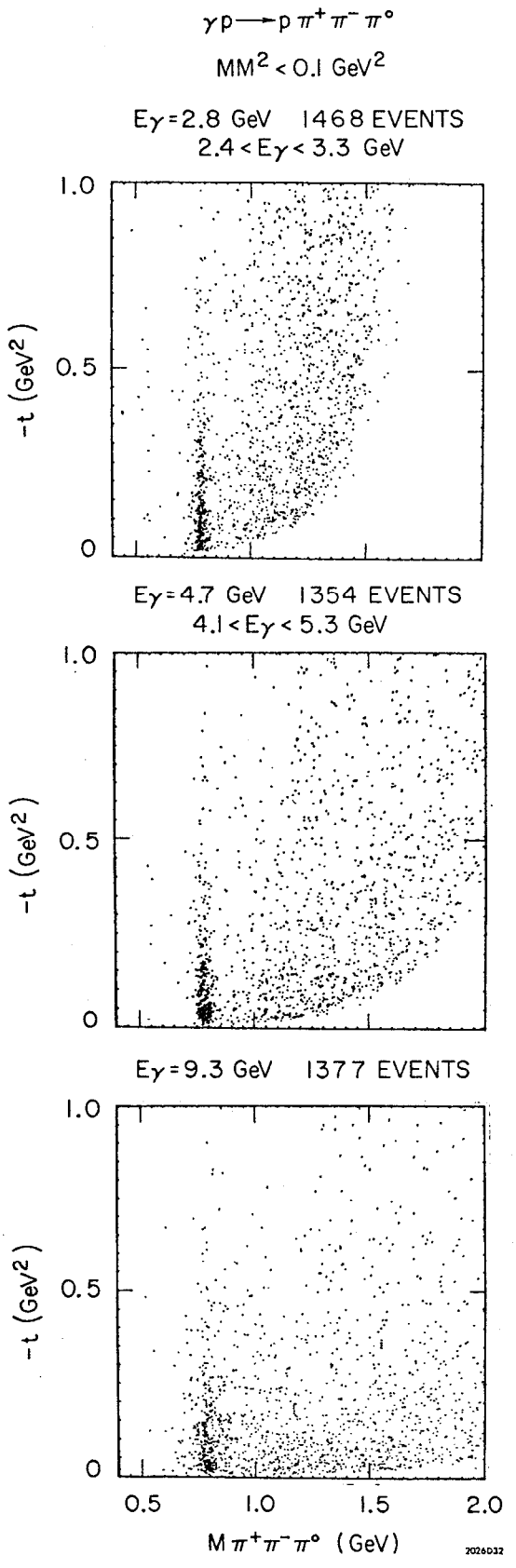
γp → p π+ π− π°
MM² < 0.1 GeV²
Eγ = 2.8 GeV 1468 EVENTS
2.4 < Eγ < 3.3 GeV
Eγ = 4.7 GeV 1354 EVENTS
4.1 < Eγ < 5.3 GeV
Eγ = 9.3 GeV 1377 EVENTS
-t (GeV²)
1.0
0.5
0
0.5
1.0
1.5
2.0
M π+ π− π° (GeV)
2026D32

Fig. 17

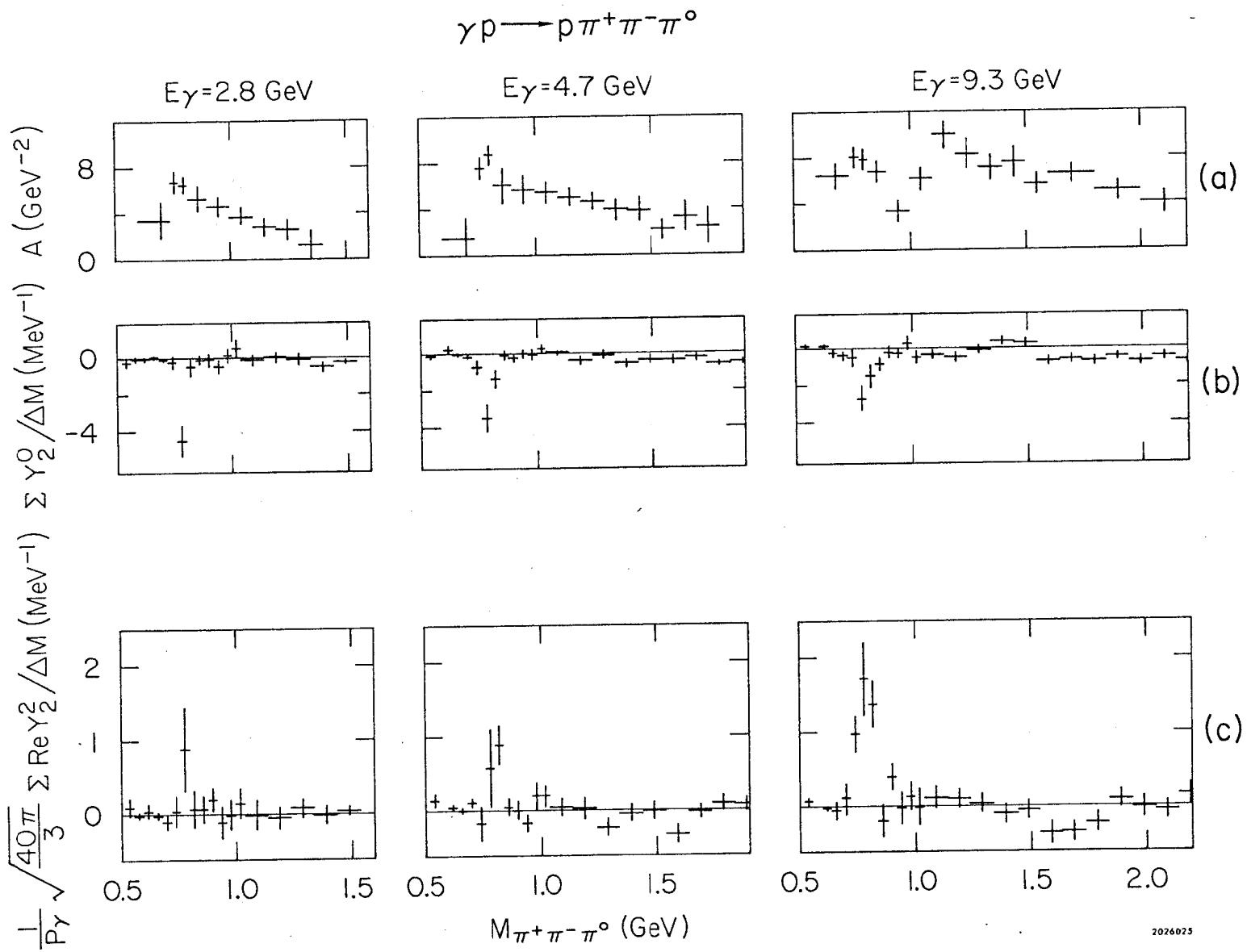
γp → pπ+π−π°
Eγ=2.8 GeV
Eγ=4.7 GeV
Eγ=9.3 GeV
A (GeV⁻²)
Σ Y₂⁰/ΔM (MeV⁻¹)
(a)
(b)
(c)
8
0
-4
2
1
0.5
1.0
1.5
2.0
Mπ+π−π° (GeV)
2026023

Fig. 18

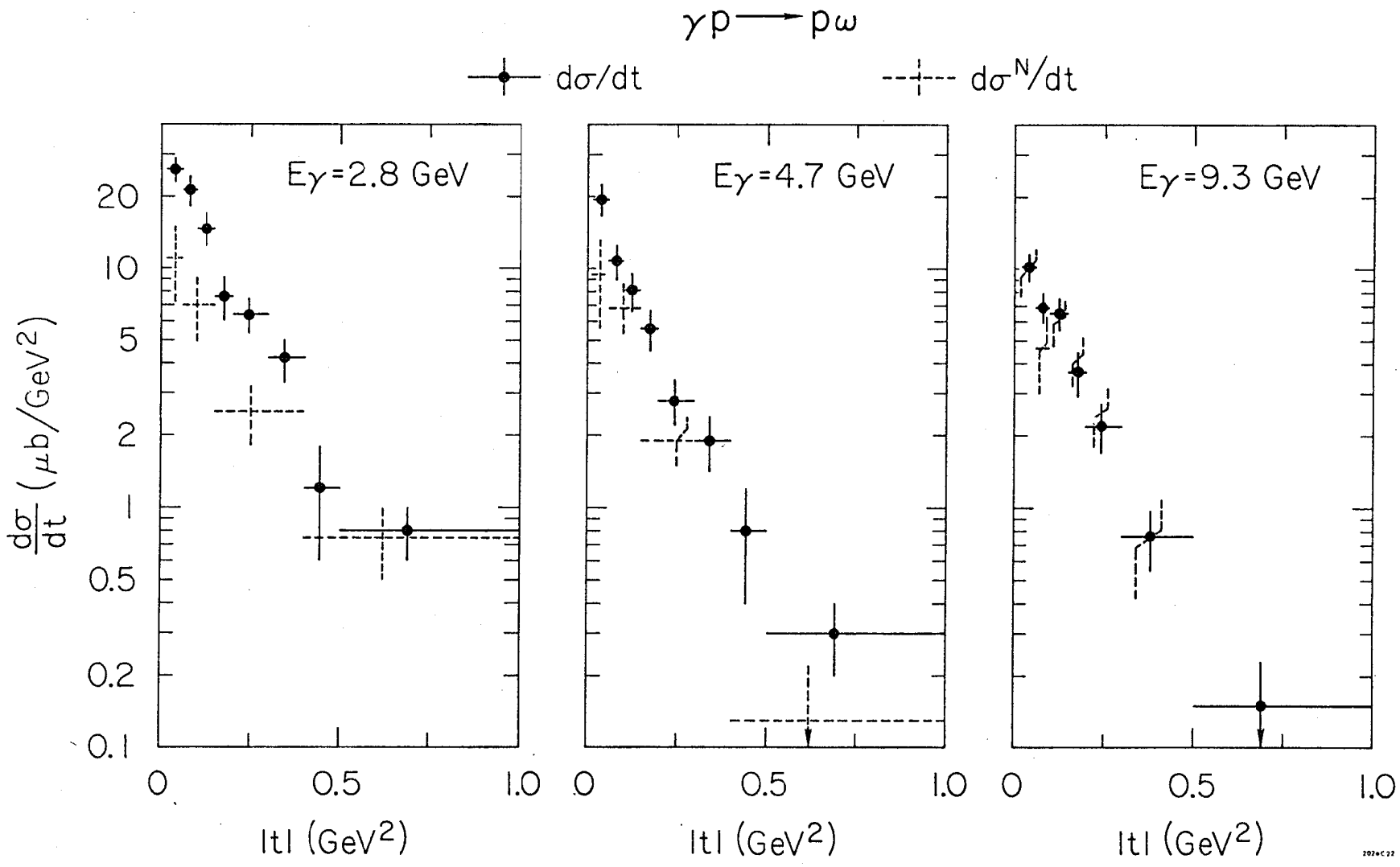
γp → pω
dσ/dt
dσ^N/dt
Eγ=2.8 GeV
Eγ=4.7 GeV
Eγ=9.3 GeV
dσ/dt (μb/GeV²)
20
10
5
2
1
0.5
0.2
0.1
0
0.5
1.0
|t| (GeV²)

Fig. 19

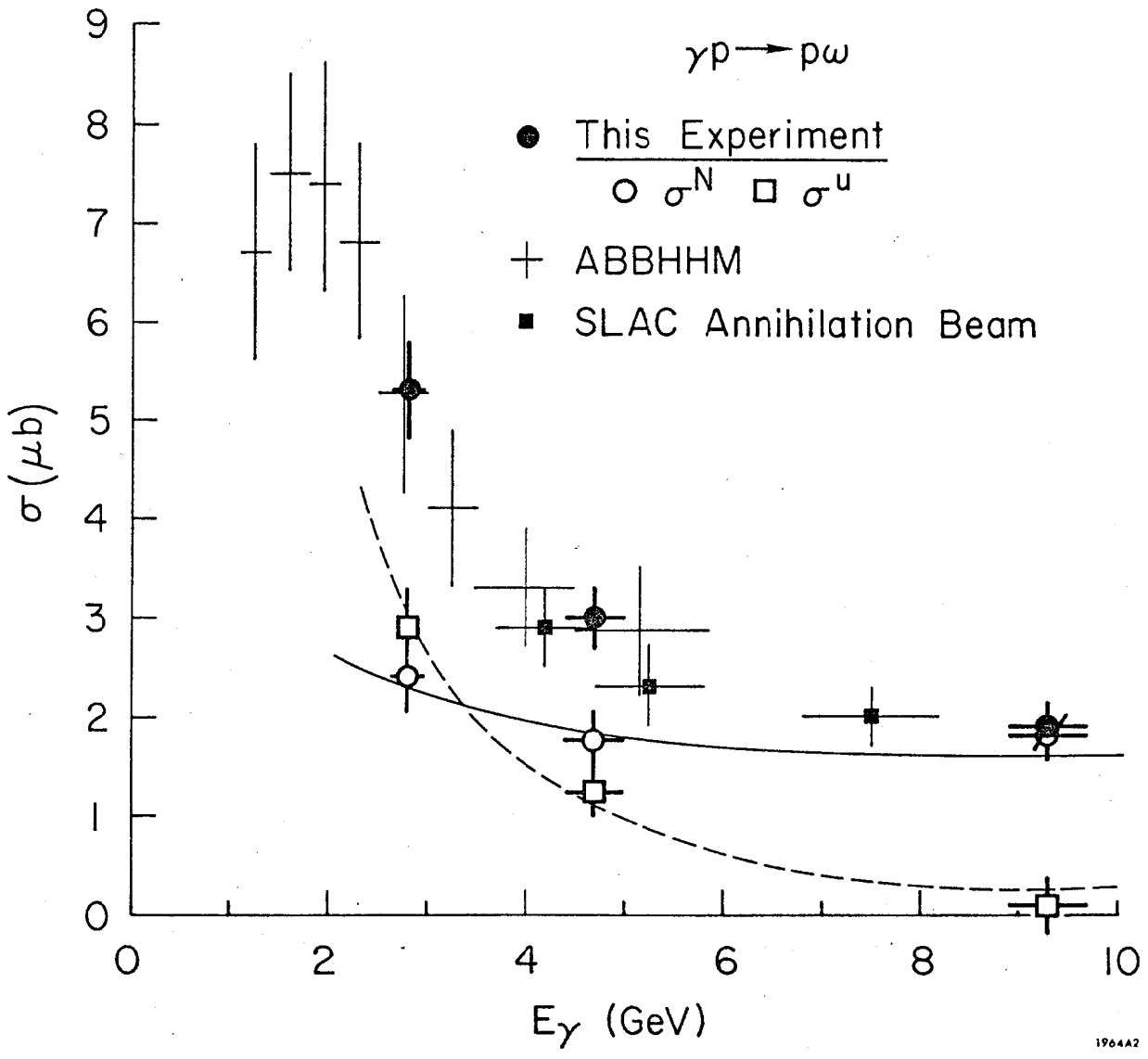
$\gamma p \rightarrow p\omega$
This Experiment
$\circ\ \sigma^N\ \square\ \sigma^u$
ABBHHM
SLAC Annihilation Beam
$\sigma(\mu b)$
E_γ (GeV)
0
1
2
3
4
5
6
7
8
9
0
2
4
6
8
10
1964A2

Fig. 20

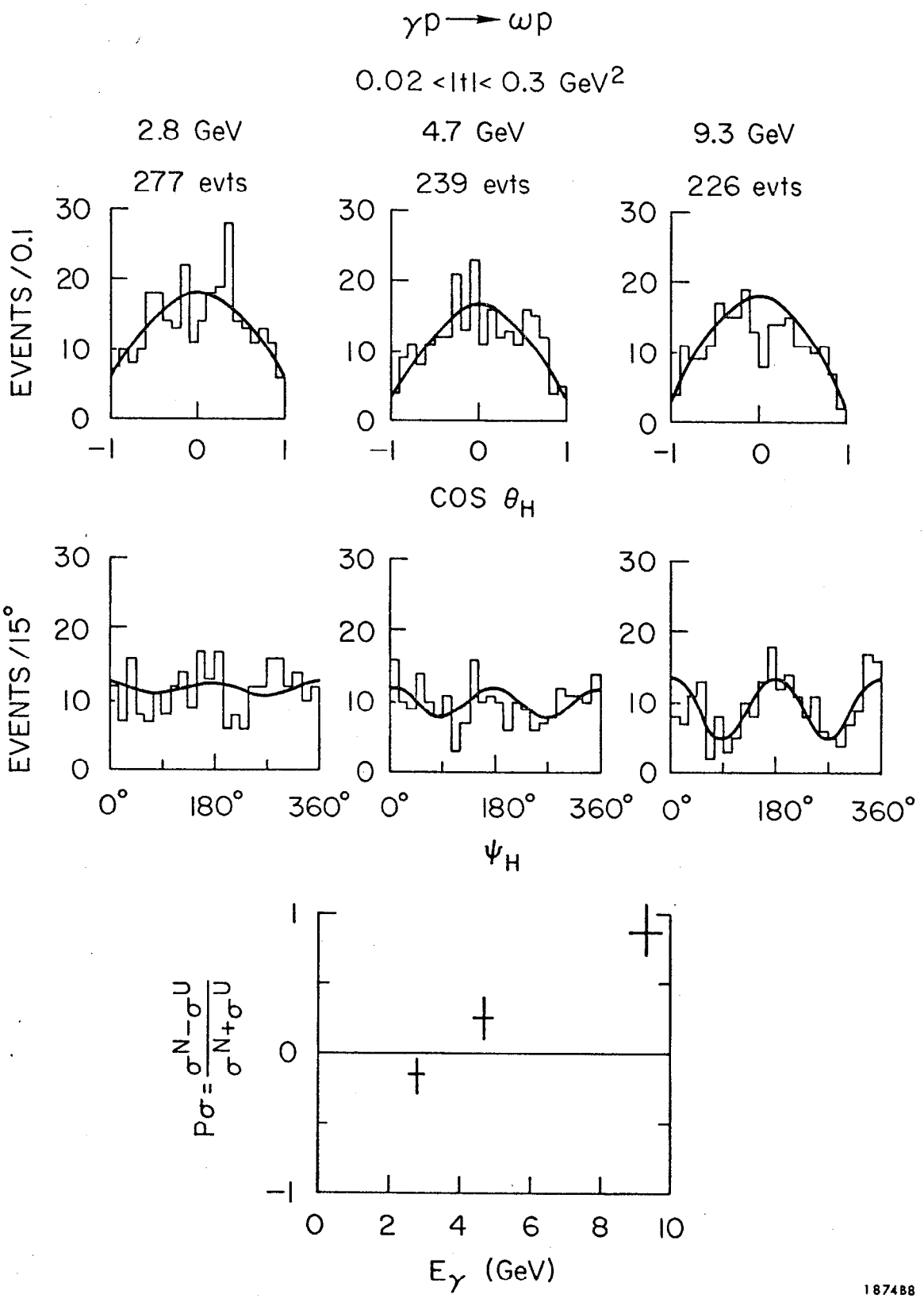
γp → ωp
0.02 < |t| < 0.3 GeV²
2.8 GeV
277 evts
4.7 GeV
239 evts
9.3 GeV
226 evts
EVENTS / 0.1
COS θH
EVENTS / 15°
ΨH
P_b^σ = (σ_b^N − σ_b^U) / (σ_b^N + σ_b^U)
Eγ (GeV)
187488

Fig. 21

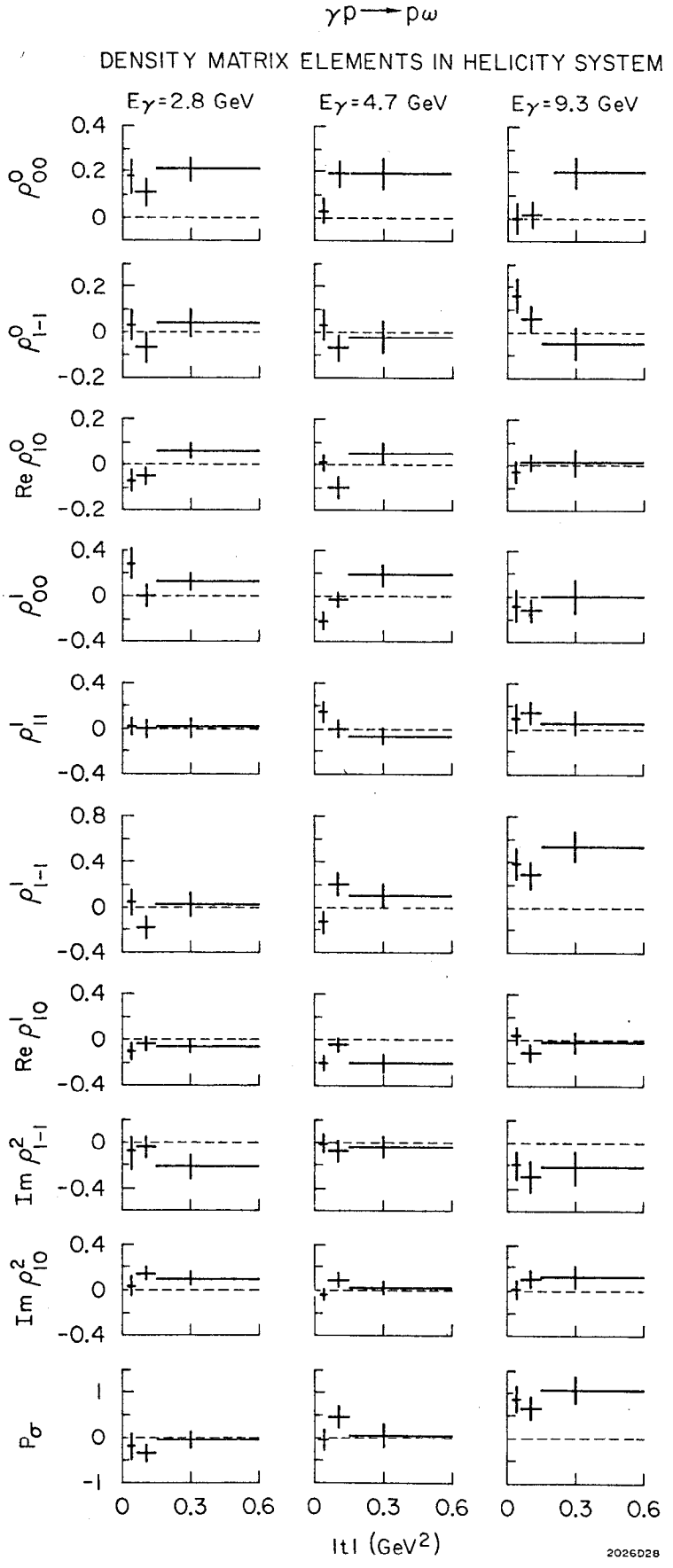
γp → pω
DENSITY MATRIX ELEMENTS IN HELICITY SYSTEM
Eγ=2.8 GeV
Eγ=4.7 GeV
Eγ=9.3 GeV
ρ^0_{00}
ρ^0_{1-1}
Re ρ^0_{10}
ρ^1_{00}
ρ^1_{11}
ρ^1_{1-1}
Re ρ^1_{10}
Im ρ^2_{1-1}
Im ρ^2_{10}
P_σ
0.4
0.2
0
-0.2
0.2
0
-0.2
0.2
0
-0.2
0.4
0
-0.4
0.4
0
-0.4
0.8
0.4
0
-0.4
0.4
0
-0.4
0
-0.4
0.4
0
-0.4
1
0
-1
0
0.3
0.6
|t| (GeV²)
2026D28

Fig. 22

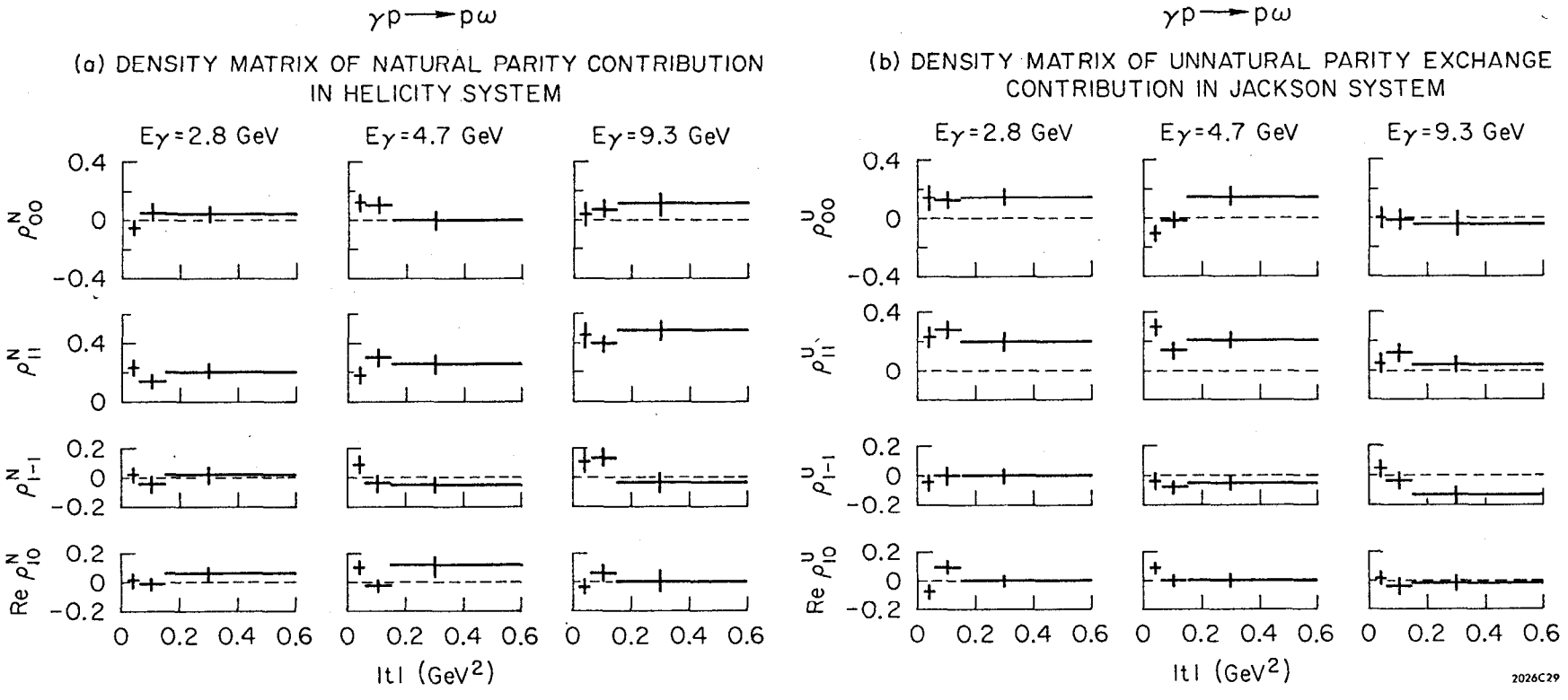
γp → pω
(a) DENSITY MATRIX OF NATURAL PARITY CONTRIBUTION IN HELICITY SYSTEM
Eγ=2.8 GeV
Eγ=4.7 GeV
Eγ=9.3 GeV
ρ^N_{00}
ρ^N_{11}
ρ^N_{1-1}
Re ρ^N_{10}
0.4
0
-0.4
0.2
-0.2
0 0.2 0.4 0.6
|t| (GeV²)
γp → pω
(b) DENSITY MATRIX OF UNNATURAL PARITY EXCHANGE CONTRIBUTION IN JACKSON SYSTEM
Eγ=2.8 GeV
Eγ=4.7 GeV
Eγ=9.3 GeV
ρ^U_{00}
ρ^U_{11}
ρ^U_{1-1}
Re ρ^U_{10}
0.4
0
-0.4
0.2
-0.2
0 0.2 0.4 0.6
|t| (GeV²)
2026C29

Fig. 23

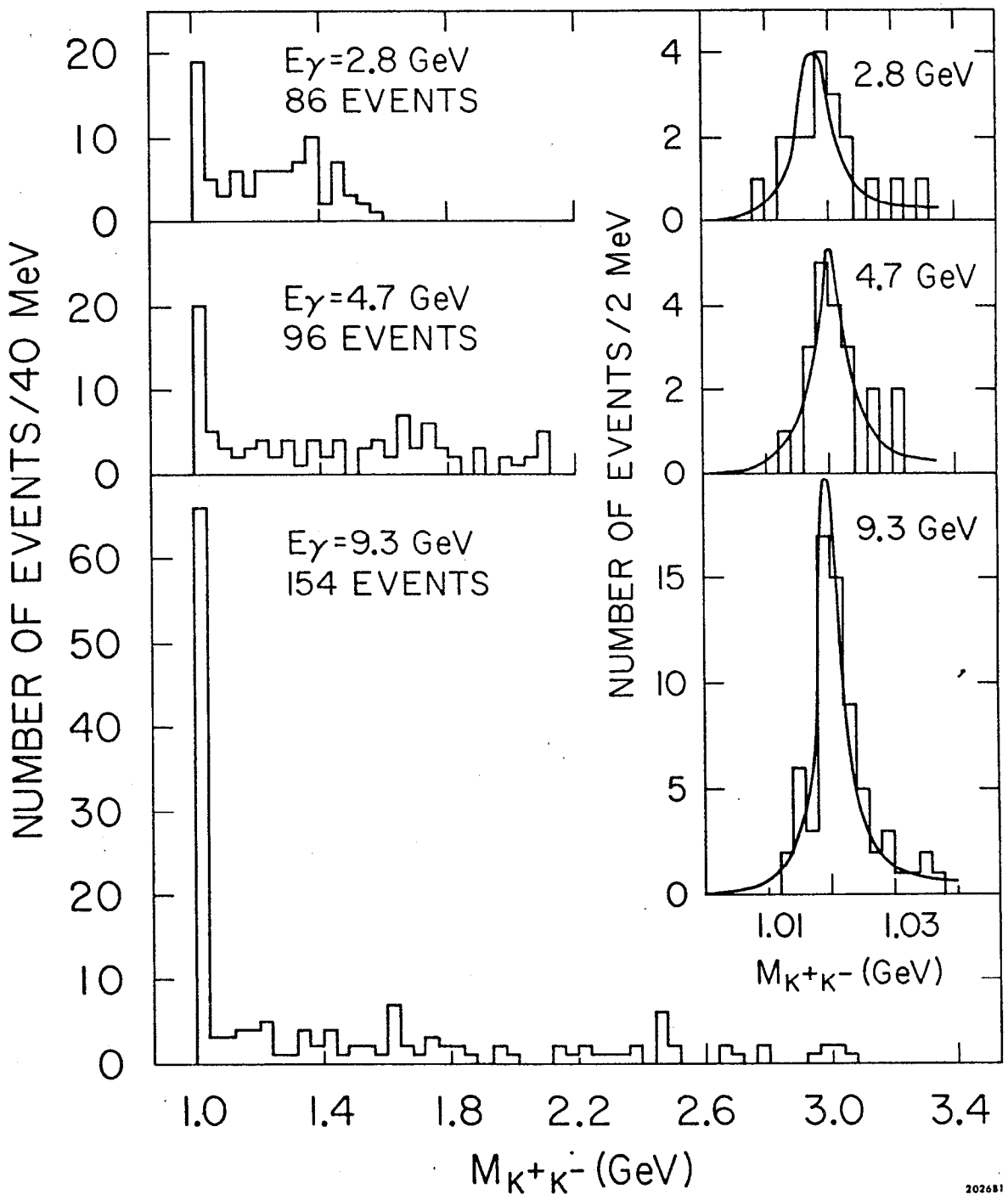
γp → pK+K−
|t| > 0.02 GeV2
Eγ=2.8 GeV
86 EVENTS
Eγ=4.7 GeV
96 EVENTS
Eγ=9.3 GeV
154 EVENTS
NUMBER OF EVENTS/40 MeV
NUMBER OF EVENTS/2 MeV
2.8 GeV
4.7 GeV
9.3 GeV
1.01
1.03
MK+K− (GeV)
1.0
1.4
1.8
2.2
2.6
3.0
3.4
MK+K− (GeV)
202681

Fig. 24

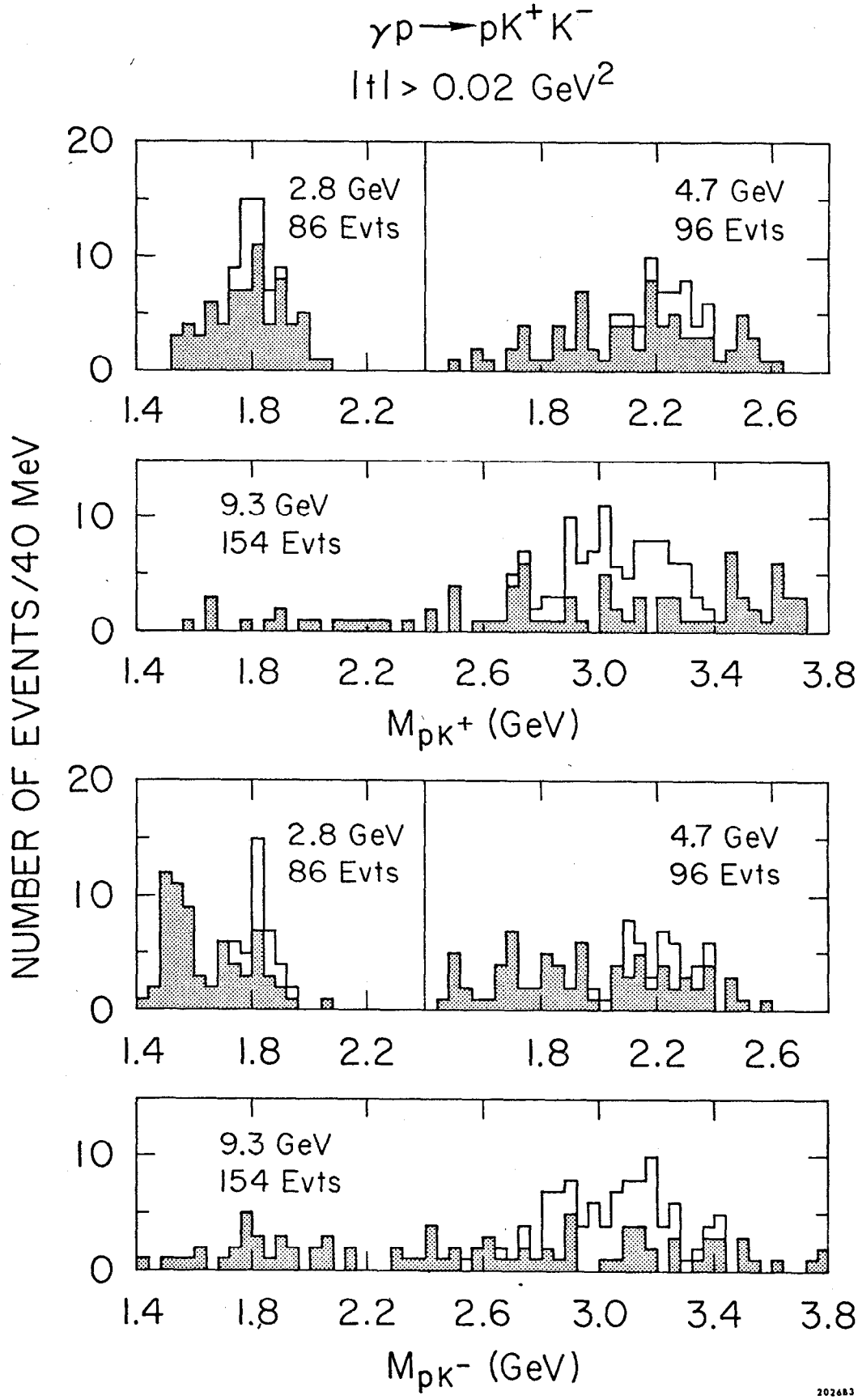
γp → pK⁺K⁻
|t| > 0.02 GeV²
2.8 GeV
86 Evts
4.7 GeV
96 Evts
9.3 GeV
154 Evts
NUMBER OF EVENTS/40 MeV
M_pK⁺ (GeV)
M_pK⁻ (GeV)
202683

Fig. 25

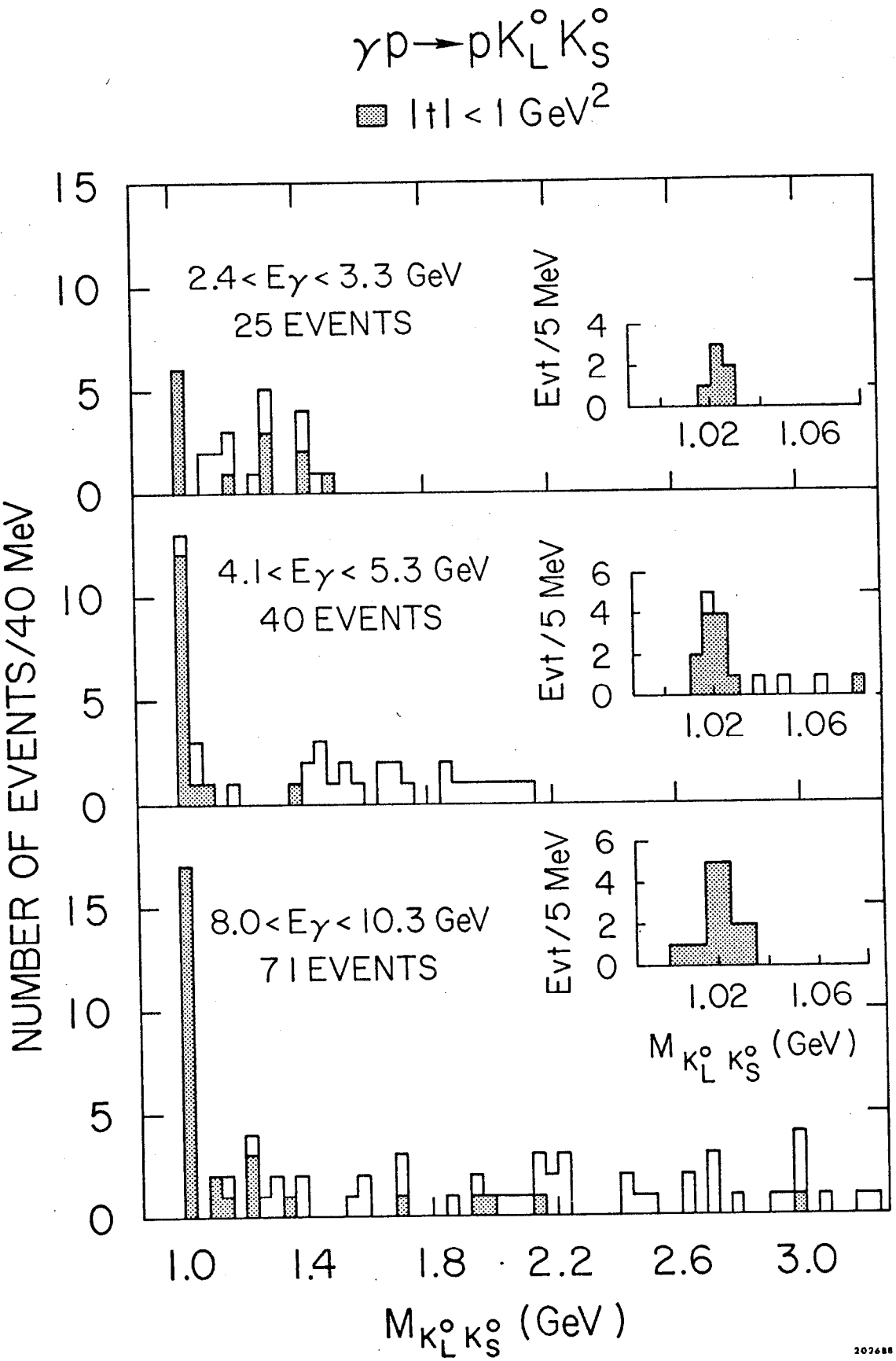
γp→pK°L K°S
|t| < 1 GeV²
2.4 < Eγ < 3.3 GeV
25 EVENTS
4.1 < Eγ < 5.3 GeV
40 EVENTS
8.0 < Eγ < 10.3 GeV
71 EVENTS
Evt/5 MeV
NUMBER OF EVENTS/40 MeV
M K°L K°S (GeV)
202688

Fig. 26

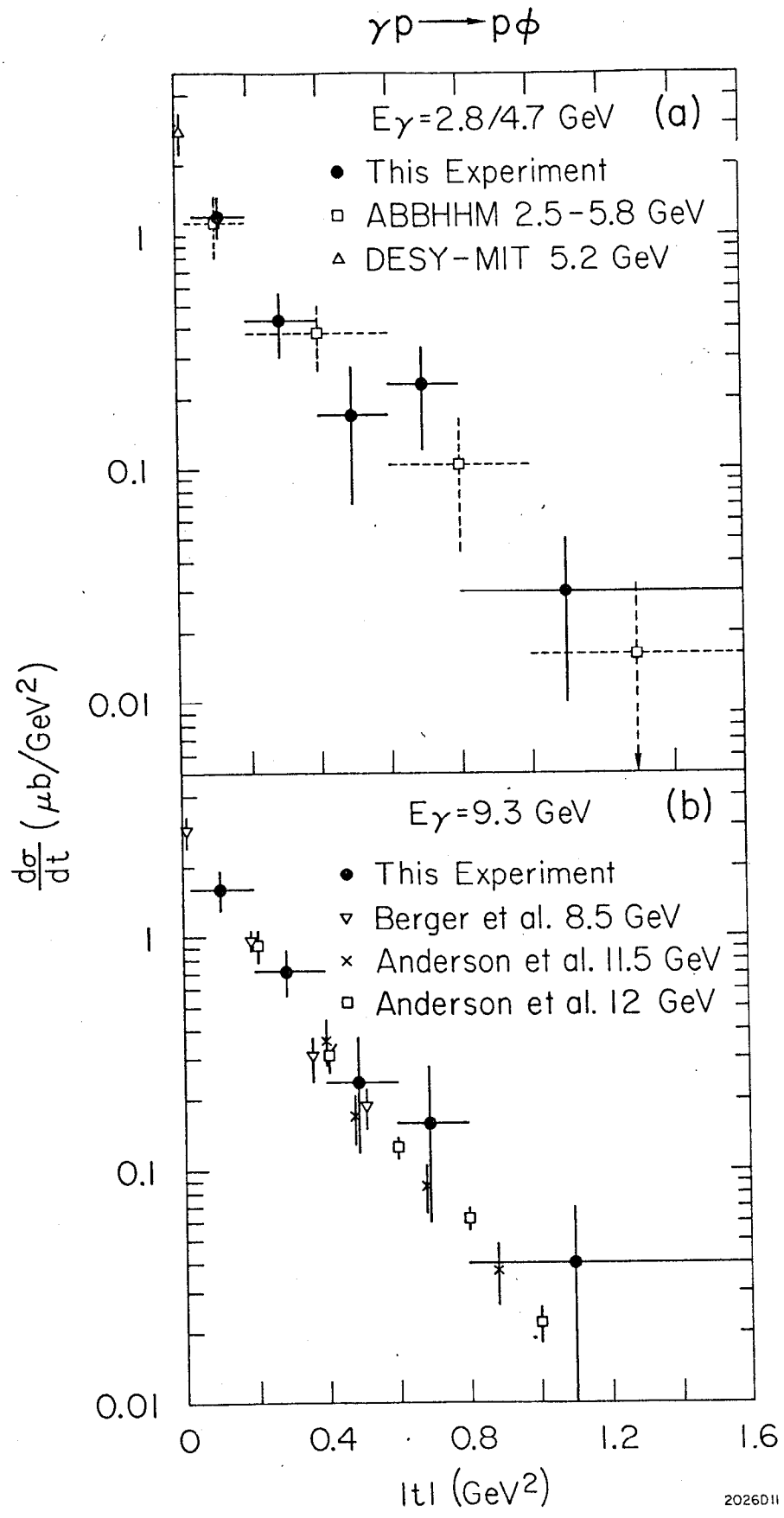
γp → pφ
Eγ=2.8/4.7 GeV (a)
This Experiment
ABBHHM 2.5-5.8 GeV
DESY-MIT 5.2 GeV
Eγ=9.3 GeV (b)
This Experiment
Berger et al. 8.5 GeV
Anderson et al. 11.5 GeV
Anderson et al. 12 GeV
dσ/dt (μb/GeV²)
1
0.1
0.01
0
0.4
0.8
1.2
1.6
|t| (GeV²)
2026D11

Fig. 27

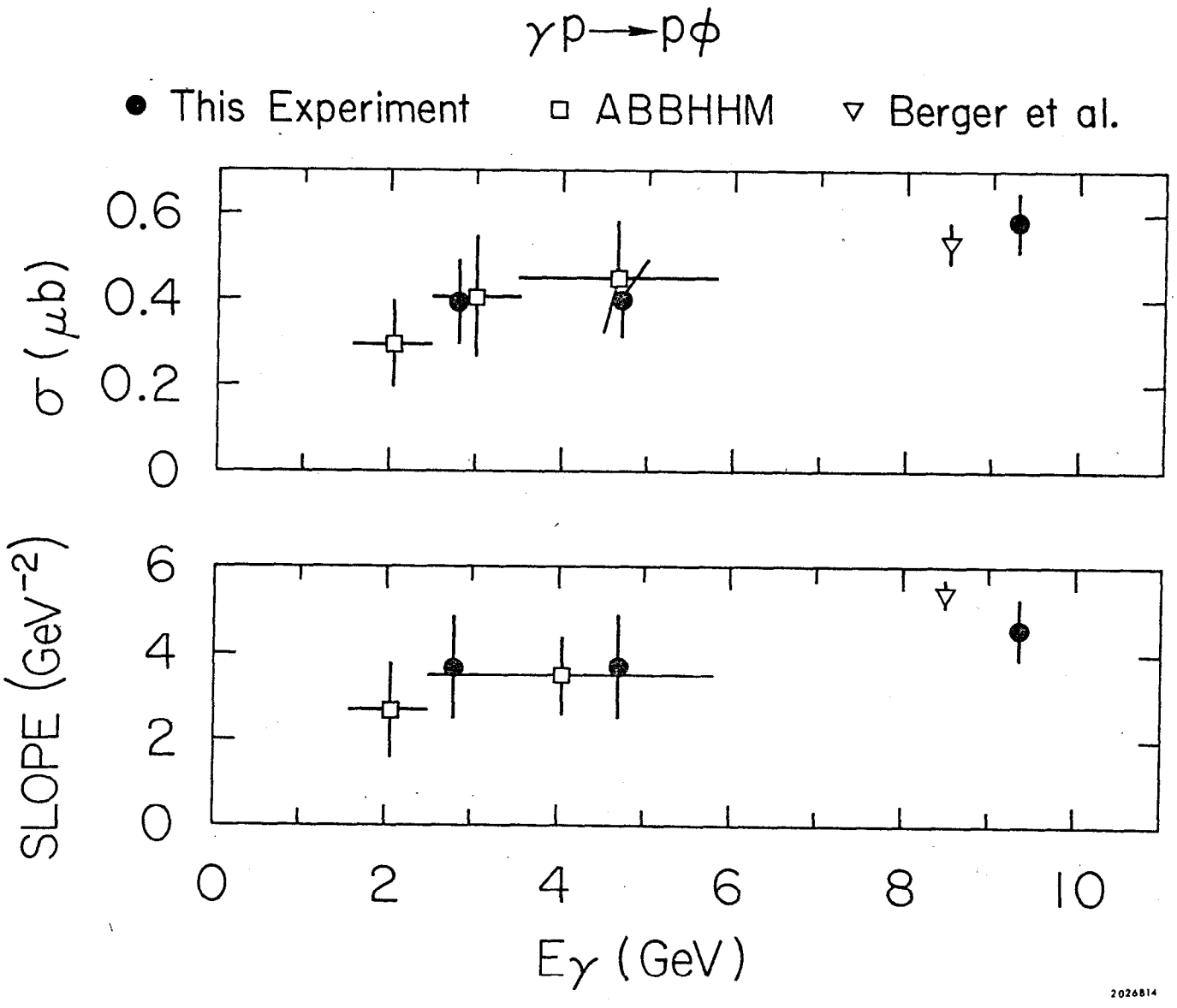
γp→pφ
This Experiment
ABBHHM
Berger et al.
σ (μb)
0.6
0.4
0.2
0
SLOPE (GeV⁻²)
6
4
2
0
0
2
4
6
8
10
Eγ (GeV)
2026B14

Fig. 28

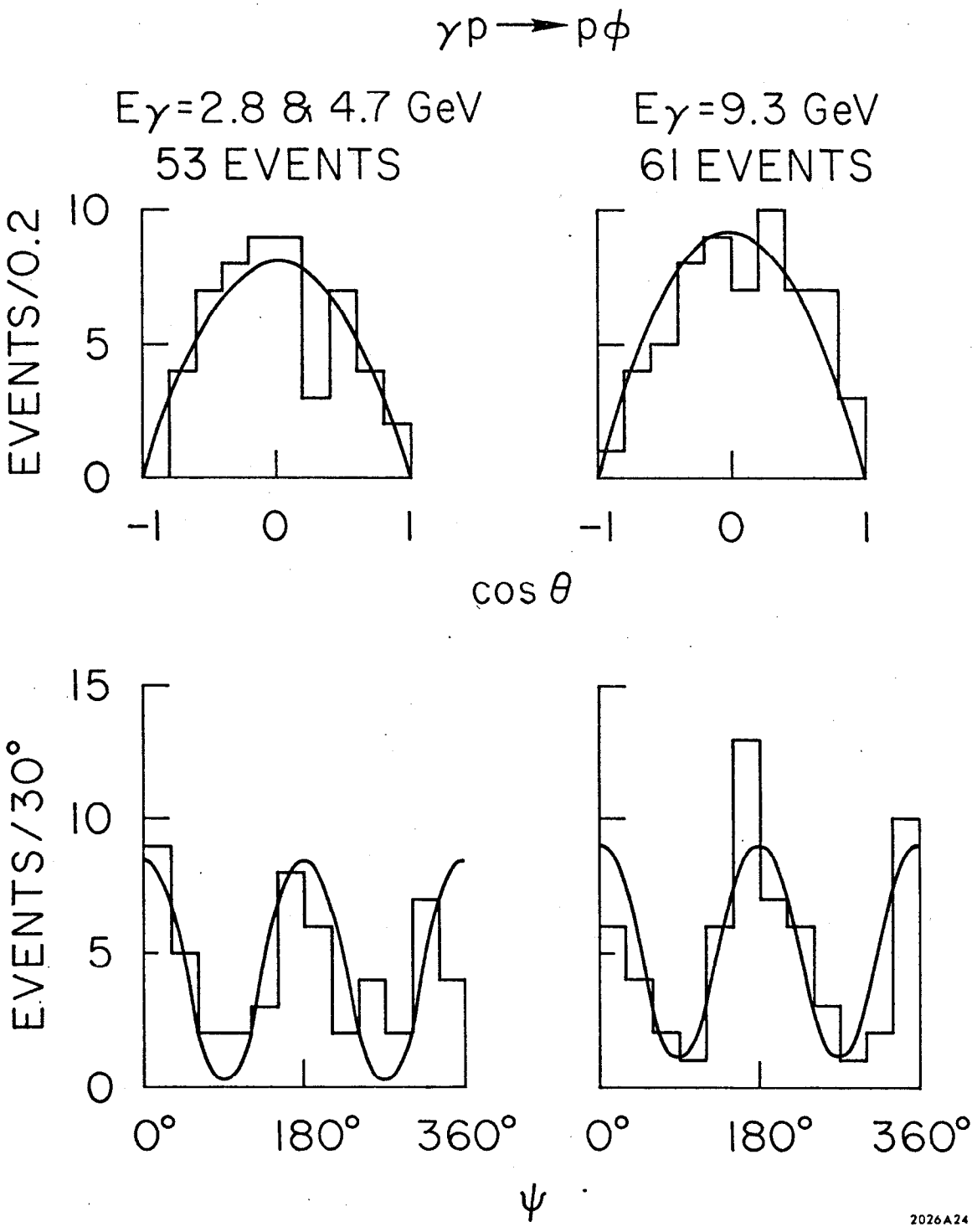
γp → pφ
Eγ=2.8 & 4.7 GeV
53 EVENTS
Eγ=9.3 GeV
61 EVENTS
EVENTS/0.2
10
5
0
-1
0
1
cos θ
EVENTS/30°
15
10
5
0
0°
180°
360°
ψ
2026A24

Fig. 29

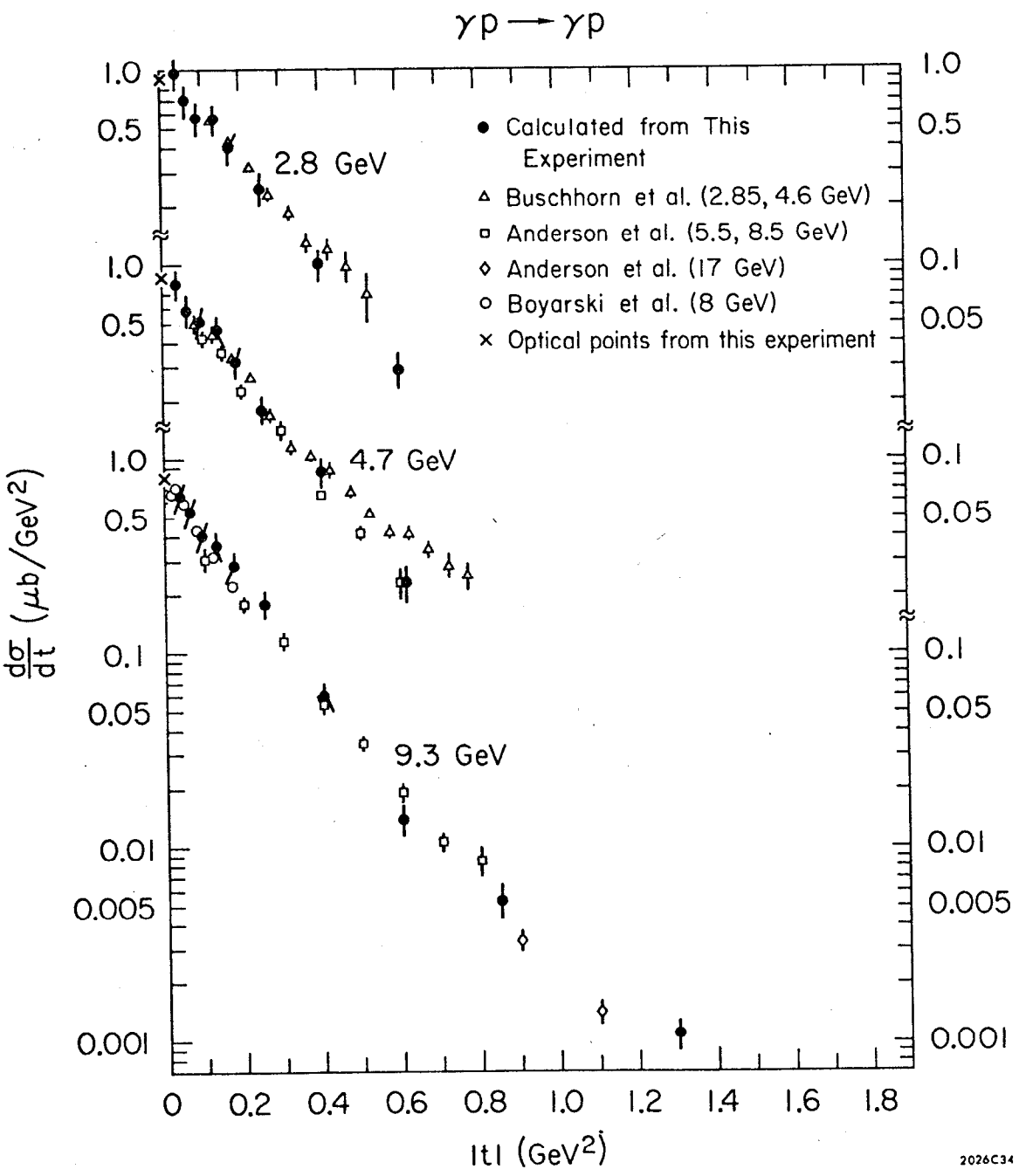
γp → γp
Calculated from This Experiment
Buschhorn et al. (2.85, 4.6 GeV)
Anderson et al. (5.5, 8.5 GeV)
Anderson et al. (17 GeV)
Boyarski et al. (8 GeV)
Optical points from this experiment
2.8 GeV
4.7 GeV
9.3 GeV
dσ/dt (μb/GeV²)
|t| (GeV²)
2026C34

Fig. 30